

**HIGH-POWER HIGH-LINEARITY PHOTODIODES AND HIGH-
POWER PHOTODIODES AS OPTOELECTRONIC MIXERS**

Dissertation

Presented to
the faculty of the School of Engineering and Applied Science
University of Virginia

In Partial Fulfillment
of the requirements for the Degree
Doctor of Philosophy
in Electrical Engineering

by

Huapu Pan

August 2010

© Copyright

by

Huapu Pan

August 2010

Abstract

Even since fibers are proposed to replace conventional coaxial cables to transmit microwave signals, the applications for analog optical link have been rapidly increasing such as phased array antennas, radio over fiber, photonic analog-to-digital converters, etc. Power handling capability is an essential figure of merit for photodiodes that are utilized in analog optical links in order to minimize the loss of the analog optical link. In this dissertation the saturation mechanisms in uni-traveling-carrier (UTC) photodiodes and modified uni-traveling-carrier (MUTC) photodiodes are investigated, and some guidelines for the design of high-power UTC and MUTC photodiodes are presented.

Photodiodes are frequently the limiting factor for the linearity performance of an analog optical link. Third-order output intercept point (OIP3), the figure of merit for the linearity of photodiode, needs to be maximized especially at high frequencies. In this dissertation the nonlinear phenomena in Charge-Compensated MUTC (CC-MUTC) photodiodes are quantitatively measured, and the physical origins of those nonlinear phenomena are explained. An equivalent circuit model is developed that provides excellent fits to the measured OIP3 of CC-MUTC photodiodes. The equivalent circuit model is used to optimize the operating wavelength for the highest OIP3 of CC-MUTC photodiodes, and a high OIP3 of 57.5 dBm is achieved for CC-MUTC at 152 MHz. An InGaAs/InP partially depleted absorber photodiode with highly doped absorbers (HD-PDA) and a modified uni-traveling-carrier photodiode with highly doped absorber (HD-MUTC) are designed to improve the OIP3 at high frequencies. For HD-MUTC the OIP3

starts at a high value of 55 dBm at low frequency and remains as high as 47.5 dBm at 20 GHz.

Radio-over-fiber systems operating at millimeter-wave frequencies have great potential in providing future V-band (50-75 GHz) wireless networks with larger channel capacity. Photodiodes can be used as V-band optoelectronic mixers, but photodiodes must be able to deliver high up-converted RF power. In this dissertation a high-power MUTC photodiode is presented to work as a V-band optoelectronic mixer. By optimizing the operation condition of the MUTC photodiode, a record high up-converted RF power of -4.7 dBm was achieved at 60 GHz when the photocurrent was 70 mA.

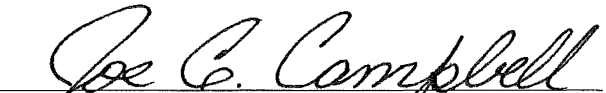
APPROVAL SHEET

The dissertation is submitted in partial fulfillment of the requirements for the degree of

Doctor of Philosophy in Electrical Engineering

Huapu Pan

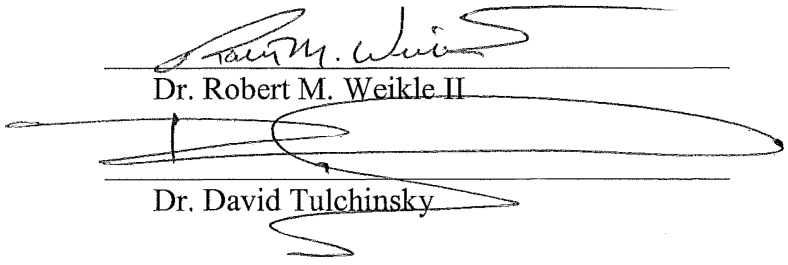
This dissertation has been read and approved by the examining Committee:


Dr. Joe C. Campbell (Advisor)

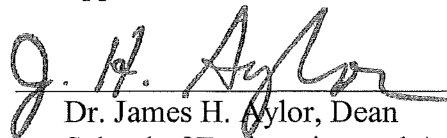
Dr. Archie L. Holmes Jr. (committee chair)


Dr. Maite Brandt-Pearce

Dr. Robert M. Weikle II


Dr. David Tulchinsky

Accepted for the School of Engineering and Applied Science:


Dr. James H. Aylor, Dean
School of Engineering and Applied Science

(August 2010)

Dedicated

To

my parents

Acknowledgements

This dissertation is the summary of my research work at University of Virginia. The research experience at University of Virginia was very pleasant working with so many great researchers in this excellent environment. There are many people who made important contribution to my research work, and I would like to show my deepest appreciation to all of them.

My deepest gratitude is to my advisor, Dr. Joe C. Campbell. His invaluable guidance of my research and his generous sharing of his wealth of knowledge lit up my way to a successful graduate research study. I feel that I am amazingly fortunate because on one hand, Dr. Campbell is such an experienced advisor who would give me the freedom to explore on my own and at the same time provide insightful advices. On the other hand, Dr. Campbell is so friendly and interesting as a person that his hospitality, his life philosophies and his life stories made my stay in University of Virginia a extremely memorable experience. Dr. Campbell taught me innumerable lessons and insights on research as well as life in general.

I would like to thank Dr. Archie L. Holmes for his insightful comments and constructive criticisms at different stages of my research. My thanks also go to the members of my dissertation committee, Dr. Maite Brandt-Pearce, Dr. Lloyd R. Harriott, Dr. Robert M. Weikle II, and Dr. David Tulchinsky. Their valuable feedback since my proposal helped me improve my research in many ways.

I am thankful to Dr. Andreas Beling for familiarizing me in the lab and the measurement process. The numerous and productive discussions with Andreas greatly helped me understand the mechanisms of the research and led to many new research ideas.

I am also very grateful to the members of the Dr. Campbell's research group at University of Virginia, with whom I have worked during the whole process of my graduate study. Particularly, I would like to acknowledge Han-Din Liu, Dion C. McIntosh, Xin Wang, Hao Chen, Zhi Li, Qiugui Zhou, Zhiwen Lu, Kejia Li, Yang Fu, Joseph Murray, Jinrong Yuan, for the many valuable discussions that helped me understand my research area better, especially to Zhi Li and Yang Fu for their friendship and support. I would like to thank Brenda E. Crider, Gloria R. Walker, Dan R. Fetko, Eileen F. Thacker, and Katherine L. Harlow for their administrative help. Brenda has been incredibly helpful in keeping everything in order and making our group happy and warm.

Last, but not least, I wish to express my gratitude to my family. My father Shiyong Pan and my mother Ping Zheng, deserve my deepest gratitude for their dedication and the many years of love and support since the birth of my life. This work can never be achieved without the support from them.

Huapu Pan

University of Virginia

August 2010

Table of Contents

| | |
|--|------------|
| Abstract | III |
| Acknowledgements | V |
| Chapter 1 Introduction | 14 |
| 1.1 Analog Optical Links and High-Power Photodiodes | 15 |
| 1.2 High-Power High-Linearity Photodiodes | 17 |
| 1.3 High-Power Photodiodes as Optoelectronic Mixers | 18 |
| 1.4 Thesis Organization | 19 |
| Chapter 2 High Power Photodiodes | 20 |
| 2.1 Introduction | 20 |
| 2.2 Brief Review on High-Power Photodiode Structures | 20 |
| 2.3 Saturation Mechanisms in Uni-Traveling-Carrier Photodiodes | 24 |
| 2.4 The Role of Cliff Layer | 28 |
| 2.5 Conclusion | 32 |
| Chapter 3 Characterization of Photodiode Linearity | 34 |
| 3.1 Introduction | 34 |
| 3.2 Conventional Two-Tone Setup | 35 |
| 3.3 Problems with Two-Tone Setup | 37 |
| 3.4 Three-Tone Setup | 40 |
| 3.5 Bias Modulation Setup | 43 |
| 3.6 Conclusion | 46 |
| Chapter 4 Nonlinear Phenomena in Photodiodes and the Equivalent Circuit Model | 47 |
| 4.1 Introduction | 47 |
| 4.2 Nonlinear Phenomena in Photodiodes | 47 |
| 4.3 Physical Mechanisms of Nonlinear Phenomena | 50 |
| 4.4 The Equivalent Circuit Model in Two-Tone Setup | 54 |

| | | |
|------------------|---|------------|
| 4.5 | Optimization of Photodiode Linearity Using the Equivalent Circuit Model | 57 |
| 4.6 | The Equivalent Circuit Model in Bias Modulation Setup | 61 |
| 4.7 | Conclusion | 64 |
| Chapter 5 | Novel Designs for High Linearity Photodiodes | 66 |
| 5.1 | Introduction | 66 |
| 5.2 | Partially Depleted Absorber Photodiodes with Highly Doped Absorber | 67 |
| 5.2.1 | Device Design | 67 |
| 5.2.2 | Nonlinear Phenomena And Equivalent Circuit Analysis | 69 |
| 5.3 | Modified Uni-Traveling-Carrier Photodiodes with Highly Doped Absorber | 72 |
| 5.3.1 | Device Design | 72 |
| 5.3.2 | Measurement of Nonlinear Phenomena | 74 |
| 5.3.3 | Measurement of OIP3 | 75 |
| 5.3.4 | Explanation for the Peak of OIP3 at Certain Photocurrent | 83 |
| 5.4 | Conclusions | 88 |
| Chapter 6 | High Power Photodiodes as Optoelectronic Mixers | 90 |
| 6.1 | Introduction | 90 |
| 6.2 | Device Design and Measurement Setup | 92 |
| 6.3 | Measurement Results | 95 |
| 6.4 | Theoretical Calculations and Maximum Up-converted RF Power | 100 |
| 6.5 | Conclusion | 105 |
| Chapter 7 | Conclusions and Future Work | 107 |
| 7.1 | Conclusions | 107 |
| 7.2 | Future Work | 110 |
| 7.2.1 | Improved Device Structures | 110 |
| 7.2.2 | Wilkinson Power Combiner | 113 |

List of Figures

| | | |
|------------|---|----|
| Figure 1 | Schematic of a typical analog optical link..... | 15 |
| Figure 2 | Loss of the analog optical link versus photocurrent with different have-wave voltage of the modulator | 16 |
| Figure 2.1 | Schematic, carrier distribution and electric field distribution of (a) PIN photodiodes and (b) PDA photodiodes..... | 21 |
| Figure 2.2 | Schematic, carrier distribution and electric field distribution of (a) UTC photodiodes and (b) MUTC photodiodes | 22 |
| Figure 2.3 | Schematic of InGaAs/InP CC-MUTC photodiode..... | 25 |
| Figure 2.4 | Measured and simulated (a) RF output power versus optical power and (b) responsivity versus optical power at zero bias..... | 26 |
| Figure 2.5 | Simulated (a) electric field and (b) bandgap diagram at various optical injection levels..... | 28 |
| Figure 2.6 | (a) Schematic of InGaAs/InP CC-MUTC photodiode with a cliff layer; (b) The responsivity versus photocurrent curve for CC-MUTC photodiodes with and without cliff layer..... | 29 |
| Figure 2.7 | (a) electric field and (b) energy band diagram of the CC-MUTC photodiodes with and without cliff layer..... | 31 |
| Figure 2.8 | electric field in the CC-MUTC photodiodes with cliff layers of different doping levels..... | 32 |
| Figure 3.1 | (a) Schematic of fundamentals and IMD3 (b) The definition of OIP3 | 34 |
| Figure 3.2 | Schematic of conventional two-tone measurement setup | 35 |
| Figure 3.3 | Measurement of OIP3 of CC-MUTC at 20 mA and 50 mA | 36 |
| Figure 3.4 | Fundamental and IMD3 produced by the modulator and the photodiode with different deviations from quadrature point..... | 39 |
| Figure 3.5 | Experimental setup for three-tone measurements. | 41 |

| | | |
|-------------|--|----|
| Figure 3.6 | Voltage-dependence of OIP3 measured by two-tone and three-tone setups. | 42 |
| Figure 3.7 | Experimental setup bias modulation measurements..... | 44 |
| Figure 3.8 | IMD2 and IMD3 vs. fundamental power for CC-MUTC at 10 mA average photocurrent and 6 V average reverse bias V_{dc} | 45 |
| Figure 4.1 | Normalized imaginary part of the photodiode impedance (symbols) at $f = 1$ GHz vs. photocurrent with self-consistent simulation (solid line) at reverse bias $V_b = -8$ V. Inset: Measured responsivity normalized to the responsivity at low photocurrent and $V_b = -7$ V..... | 48 |
| Figure 4.2 | Measured photodiode capacitance (symbols) and self-consistent simulation (solid line). Inset: Relative responsivity at -7 dBm (filled circles) and -22 dBm (open circles) average optical power with quadratic polynomial fit function (solid line)..... | 49 |
| Figure 4.3 | Doping profile of Zn and Si from a SIMS measurement | 51 |
| Figure 4.4 | Equivalent circuit for the photodiode..... | 55 |
| Figure 4.5 | Measured OIP3 (circles) at 50 mA and reverse bias $V_b = -7$ V, and calculated OIP3 based on the voltage-dependent responsivity (dotted line), capacitive effects (dashed line) and all effects (solid line) | 56 |
| Figure 4.6 | Relative responsivity measured at 50 μ A photocurrent. The wavelength was changed from 1540 nm to 1650 nm in 10 nm steps. | 57 |
| Figure 4.7 | Relative responsivity measured at 50 μ A photocurrent. The wavelength was changed from 1250 nm to 1350 nm in 20 nm-steps..... | 58 |
| Figure 4.8 | exponential fits to the measured voltage-dependent responsivity | 60 |
| Figure 4.9 | Measured OIP3 of a 40- μ m-diameter CC-MUTC photodiode at 152 MHz and 50 mA on for different wavelengths..... | 61 |
| Figure 4.10 | Experimental setup bias modulation measurements..... | 62 |
| Figure 4.11 | Measured and simulated IMD2 and IMD3 vs. fundamental frequency f_1 at $I_{pd} = 10$ mA, $V_{dc} = 6$ V using the numerical model..... | 62 |
| Figure 5.1 | Schematic layer structures of HD-PDA photodiode. All doping concentrations in cm^{-3} | 67 |
| Figure 5.2 | Doping profile of the HD-PDA photodiode measured with SIMS | 68 |

Figure 5.3 Measured photodiode capacitance (symbols) and exponential fit (lines) for CC-MUTC photodiode and HD-PDA photodiode. Inset: Relative responsivity (dots) with quadratic polynomial fit (lines) for MUTC-PD and PDA-PD..... 69

Figure 5.4 Relative responsivity (dots) with quadratic polynomial fit (lines) for CC-MUTC photodiode and HD-PDA photodiode..... 70

Figure 5.5 Measured OIP3 of CC-MUTC photodiode at 50 mA and $V_b = -7$ V and that of HD-PDA photodiode at 21 mA and $V_b = -8$ V..... 71

Figure 5.6 Schematic cross section of InGaAs–InP HD-MUTC photodiode..... 72

Figure 5.7 Measured junction capacitance density for CC-MUTC photodiode, HD-PDA photodiode, and HD-MUTC photodiode. Inset: Relative responsivity for CC-MUTC, HD-PDA and HD-MUTC photodiodes..... 74

Figure 5.8 OIP3 of the HD-MUTC photodiode versus photocurrent at 7 V, 9 V and 10 V reverse bias. 76

Figure 5.9 The power of IMD3 versus fundamental power shows a good slope of 3 and an extracted OIP3 of 55 dBm at 33 mA and 10 V..... 77

Figure 5.10 Measured OIP3 of HD-MUTC photodiode at 33 mA and 42 mA. The reverse bias is 10 V. Solid line: calculated OIP3 of HD-MUTC photodiode at 10V bias assuming that $C(V)$ is the primary nonlinearity driver..... 79

Figure 5.11 Frequency dependence of OIP3 of HD-MUTC at various reverse biases and their corresponding optimized photocurrents. Solid line: $C(V)$ -limited OIP3 at 10 V; Dashed line: $C(V)$ -limited OIP3 at 7 V. 80

Figure 5.12 Measured OIP3 of (1) CC-MUTC photodiode at 50 mA and $V_b = -7$ V, (2) HD-PDA photodiode at 21 mA and $V_b = -8$ V, and (3) HD-MUTC photodiode at 33 mA and 10 V reverse bias. Solid line: calculated OIP3 of HD-MUTC photodiode based assuming the dominance of $C(V)$; Dashed line: calculated OIP3 of CC-MUTC photodiode assuming primary contributions from $C(V)$ and $C(I)$; Dotted line: calculated OIP3 of HD-MUTC photodiode assuming that $C(V)$ is the primary nonlinear driver..... 81

Figure 5.13 The compressions of IMD2 and IMD3 versus photocurrent. The calculated OIP3 based on the nonlinear parameters extracted from the measured compressions of IMD2 and IMD3 is compared with the OIP3 measured using three-tone techniques at 320 MHz and 7 V reverse bias.... 83

Figure 5.14 Measured $R(V)$ curve and the $R(V)$ curves determined from the bias modulation measurement..... 86

| | | |
|------------|--|-----|
| Figure 6.1 | Schematic of Radio-over-fiber system for V-band wireless communication | 90 |
| Figure 6.2 | Schematic of the MUTC photodiode..... | 92 |
| Figure 6.3 | Measurement setup for optical signal mixing with photodiode | 94 |
| Figure 6.4 | Relative frequency response of the MUTC photodiode measured at 50 mA and 5 V reverse bias. | 96 |
| Figure 6.5 | Measured electrical LO power and up-converted RF power versus optical IF percentage | 98 |
| Figure 6.6 | Conversion loss versus frequency at 30 mA and 70 mA. The LO and up-converted RF power versus frequency at 30 mA is also shown..... | 99 |
| Figure 6.7 | Filled shapes: measured up-converted power versus reverse bias at different photocurrent levels. Open circles: calculated optimum reverse bias..... | 102 |
| Figure 6.8 | Measured LO power versus reverse bias at different photocurrent levels. Dashed lines: optimum reverse bias corresponding to those shown in Figure 6.7..... | 105 |
| Figure 7.1 | Schematic of HD-MUTC2 | 111 |
| Figure 7.2 | Measured junction capacitance density for MUTC photodiode, HD-PDA photodiode, and simulated junction capacitance density of HD-MUTC2 photodiode. | 112 |
| Figure 7.3 | (a) mask design and (b) the equivalent circuit model of the photodiode pair coupled to a Wilkinson power combiner..... | 113 |
| Figure 7.4 | Simulation of the amplitude of voltage swing assuming a photocurrent of 10 mA. Solid line: voltage swing amplitude on the photodiode for the combiner design; Dashed line: voltage swing amplitude on the load for the combiner design; Dotted line: voltage swing amplitude on the photodiode for the discrete photodiode with tuning circuits. Dash dot line: voltage swing amplitude on the load for the discrete photodiode with tuning circuits. | 115 |

List of Tables

| | | |
|-----------|--------------------------------------|----|
| Table 4-1 | calculated OIP3 limited by R(V)..... | 60 |
|-----------|--------------------------------------|----|

Chapter 1 Introduction

Ever since Heinrich Hertz discovered radio waves in 1886, applications for radio frequency (from 3 kHz to 300 GHz) waves have expanded rapidly: from civilian applications such as radio communication to military applications such as radar. With the ever increasing demand for high bandwidth, the carrier frequency for telecommunication has already moved into the microwave frequency range (from 300 MHz to 300 GHz) and it is still rapidly increasing. Coaxial cables have been the primary media to transmit radio frequency signals since their invention in 1880. However, the loss of coaxial cables increases rapidly with the frequency of the microwave signals. Compared with coaxial cables, optical fibers have significant advantages. Fiber has smaller size, lighter weight, better immunity to electromagnetic interference, and lower propagation loss [1]. For example, a typical commercial coaxial cable exhibits loss of 56 dB/km at 2.4 GHz. In contrast, the transmission loss in typical optical fibers is less than 0.2 dB/km at 1.55 μm wavelength [1] and this loss is independent of the frequency of the microwave signals being transmitted. Thus, fibers have been used to replace conventional coaxial cables to transmit microwave signals in many applications such as phased array antennas [2], radio over fiber [3], photonic analog-to-digital converters [4], and photonic signal processing of microwave signals [5].

1.1 Analog Optical Links and High-Power Photodiodes

To transmit microwave signals through fibers, an analog optical link is required to convert the microwave signals into an optical format, transmit it through the fiber, and convert the optical signal back into the microwave domain in the receiver. A typical analog optical link consists of an optical source, a modulator that imposes the radio frequency (RF) signals onto the optical carrier, an optical fiber cable as the transmission medium, and a photodiode to convert the optical signal back into the RF signal. A schematic of a typical analog optical link is shown in Figure 1.

Loss is one of the most important figures of merit for analog optical links. The loss of coaxial cables is linearly proportional to the length of the cables. However, the loss of the analog optical link is almost independent of the length of the fiber (for transmission distances of a few 10's of km) due to the low fiber loss. The link loss is primarily dependent on the RF/optical conversion efficiencies of the modulators and photodiodes. The loss can be very large when the optical power delivered to the photodiode is small. This is due to the fact that the input RF power required for 100% modulation is only dependent on the efficiency of the optical modulator but the higher the optical power

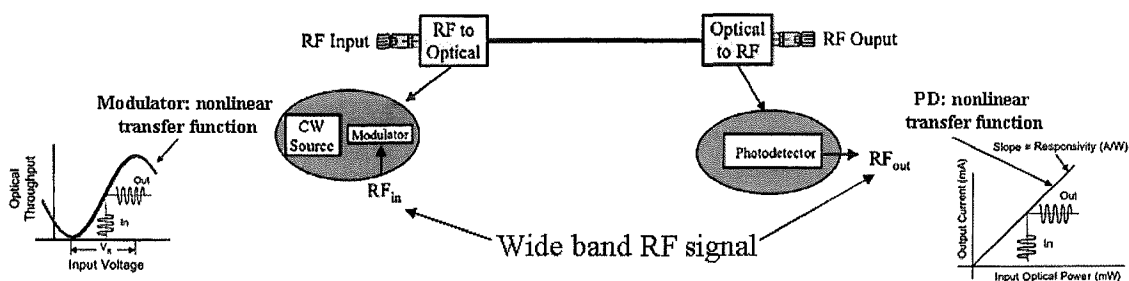


Figure 1 Schematic of a typical analog optical link

received by the photodiode, the higher the RF output power at the receiver. Assuming that the modulator has a half-wave voltage of $V_{\pi} = 5$ V, using 100% modulation, the input RF signal has a peak-to-peak voltage of $V_{pp} = 5$ V, which is equivalent to 24 dBm of RF power on a 50Ω load. If an optical power level of 1 mW is fed into a photodiode with a responsivity of 1A/W , the output RF power would be -16 dBm. Thus this analog optical link has a loss of $(24 + 16) = 40$ dB! The advantage of the low loss nature of the fiber is greatly diminished if the loss due to the RF/optical conversion is so high.

However, the loss of the analog optical link can be improved by increasing the optical power from the source. If the optical power is increased from 1 mW to 100 mW, using the same assumptions, the link loss would be 0 dB. The link loss is plotted in versus the output photocurrent with different modulator half-wave voltage, V_{π} , as shown

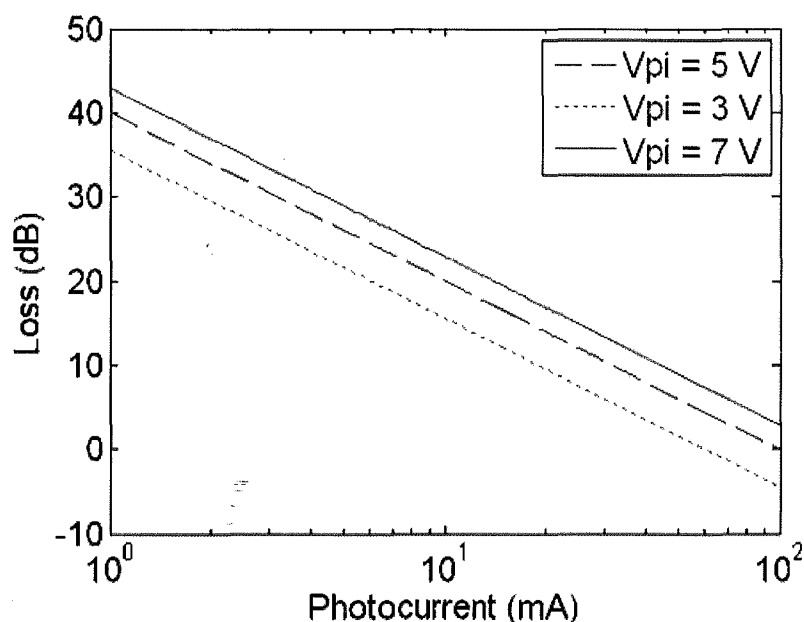


Figure 2 Loss of the analog optical link versus photocurrent with different have-wave voltage of the modulator

in Figure 2. It is clear that with low V_{π} and high photocurrent, RF signals transmitted through the analog optical link can have gain instead of loss. In this case, a photodiode that can handle very high photocurrent is required. Thus a high-power photodiode is an essential component for low loss analog optical links. In addition to reducing the link loss, higher photocurrent levels can also enable higher dynamic range and reduce the link noise figure [6].

1.2 High-Power High-Linearity Photodiodes

The spur-free dynamic range is defined as the ratio of the power of the carrier frequency to the power of the next largest harmonic or intermodulation distortions above noise floor. It is an essential figure of merit for analog optical links in applications such as phased array antennas and photonic analog-to-digital converters. There are two major nonlinear photonic components in the analog optical links, namely the optical modulators and the photodiodes. In order to improve the spur-free dynamic range of the entire link, the nonlinearities caused by both the modulators and the photodiodes should be reduced. When properly biased at the quadrature point, the harmonics and intermodulations produced by the modulators can be effectively minimized [7]. However, unlike modulators, there is not an explicit expression for the transfer function of photodiodes and the nonlinearity of photodiodes is a complicated function of reverse bias, photocurrent, and temperature [8]. Usually the linearity of photodiodes is the limiting factor for the spur-free dynamic range in high performance analog optical links, especially when the optical power is high [6]. Furthermore, a microwave signal can also be generated by heterodyning two laser sources, although it is challenging to minimize the phase noise associated

with heterodyning; the advantage of this approach is that it is almost free of nonlinear distortions [9]. In this case photodiodes become the only nonlinear source in the link, which makes it even more critical to minimize their nonlinearities.

1.3 High-Power Photodiodes as Optoelectronic Mixers

Radio-over-fiber systems operating at millimeter-wave frequencies have the potential to provide future V-band (50-75 GHz) wireless networks with greater channel capacity than current systems. Since the carrier frequency for the V-band wireless network is very high, it is desirable to transmit this high frequency signal through an optical fiber rather than via coaxial cables. Conventionally, the optical subcarrier-modulated signals are converted to electrical signals with a linear-detection photodiode and then up-converted by electrical frequency mixing. However, when operated in low bias conditions, photodiodes can exhibit very nonlinear behavior, and thus can be used as optoelectronic mixers to directly up-convert intermediate frequency (IF) signals with a high frequency optical oscillator (LO) signal [10]. When photodiodes are used as optoelectronic mixers, the necessity of using electrical mixers is eliminated. This simplifies the design of the base station for the V-band wireless network. However, in order to offer performance comparable to a conventional linear photodiode in combination with an electronic mixer, the photodiodes operated in nonlinear mode as optoelectronic mixers have to provide high power and high conversion efficiency. These requirements challenge the power handling capability and the strength of nonlinearity of photodiodes.

1.4 Thesis Organization

The primary focus of my work has been investigation of nonlinear mechanisms in high power photodiodes and optimization of the photodiode structures to achieve both high power and high linearity. However, I have also shown that high-power photodiodes, when properly designed and operated, can be used as efficient high-power optoelectronic mixers. Chapter 2 reviews several structures that were designed to improve the power handling capability of photodiodes. It also presents important guidelines for the design of high-power photodiodes. Chapter 3 describes the experimental setups and the measurement techniques that I employed to characterize the linearity performance of photodiodes. In Chapter 4 I discuss measurements of several nonlinear phenomena in photodiodes and develop an equivalent circuit model to associate the measured nonlinear phenomena with the measured intermodulation distortions from the photodiodes. Chapter 5 demonstrates two novel photodiodes structures that show improved linearity performance. Chapter 6 demonstrates a novel high-power photodiode structure that can be used as an efficient high-power optoelectronic mixer. Finally, this dissertation is summarized with future research plans in Chapter 7.

Chapter 2 High Power Photodiodes

2.1 Introduction

As discussed in Chapter 1, power handling capability is an essential figure of merit for photodiodes that are utilized in analog optical links. In this chapter, the drawbacks for conventional PIN photodiodes are discussed and several high power photodiode structures are reviewed. This is followed by a description of the saturation mechanisms in uni-traveling-carrier (UTC) photodiodes and modified uni-traveling-carrier (MUTC) photodiodes. Finally the role of a cliff layer, a thin lightly n-doped InP layer between the intrinsic InGaAs absorber and intrinsic InP layer, is analyzed and some guidelines for the design of high-power UTC and MUTC photodiodes are presented.

2.2 Brief Review on High-Power Photodiode Structures

Photodiodes with a PIN structure are widely used for optical communication because they have simple structures and relatively high responsivity. However, PIN photodiodes cannot sustain high photocurrent levels for two major reasons. First, PIN photodiodes are very susceptible to thermal failure because the electric field in the intrinsic InGaAs absorber needs to be high enough to ensure that the electrons and holes drift at the saturation velocity. On the other hand, the electric field in the intrinsic InGaAs absorber is responsible for most of the heat generation in PIN photodiode. Since InGaAs is a narrow-bandgap semiconductor, its critical temperature for thermal runaway is relatively low. This results in thermal failure at relatively small photocurrent levels.

Second, PIN photodiodes are particularly susceptible to space-charge induced current saturation. As shown in Figure 2.1(a), in PIN photodiodes the electron velocity is higher than that of holes. This causes an imbalance in the spatial profile of the photo-generated carriers with more holes than electrons in the depleted intrinsic absorber. As the optical power increases and the photo-generated carriers accumulate, the electric field in this depleted region is screened by this charge and due to the unbalanced carrier density distribution, the electric field collapses near the n side. When the field drops to the point that carriers no longer maintain saturation velocity, the bandwidth decreases and the RF output power saturates. This is referred to as the space charge effect.

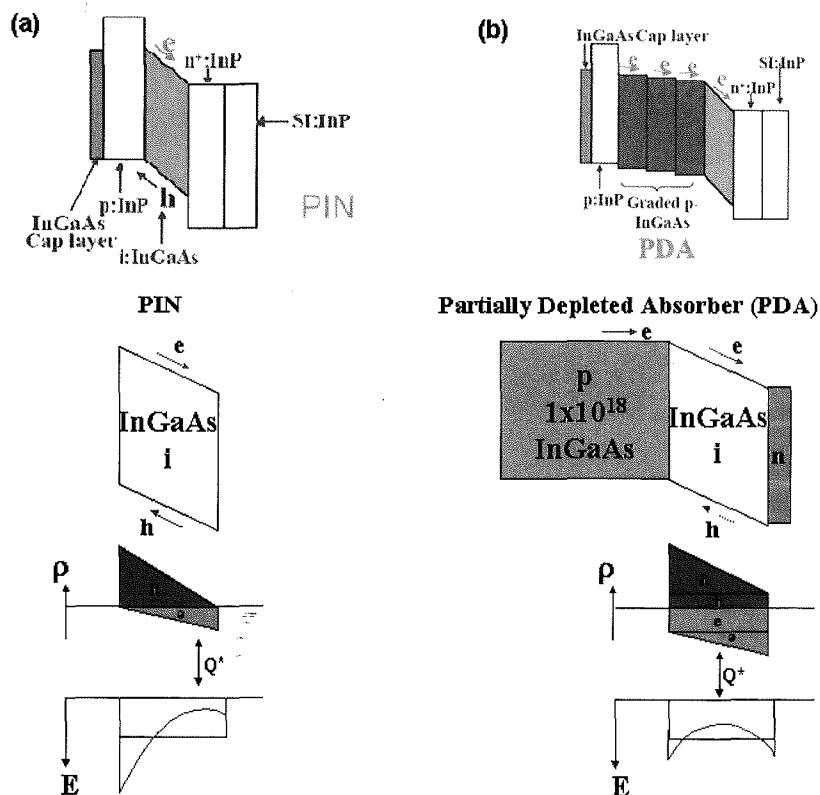


Figure 2.1 Schematic, carrier distribution and electric field distribution of (a) PIN photodiodes and (b) PDA photodiodes

Several photodiode structures have been developed to mitigate the space charge effect. Partially depleted absorber (PDA) photodiodes have both undepleted and depleted absorber regions to balance the photo-generated carriers in the depleted drift region [11]. When properly designed, the electric field collapses in the middle of the depleted drift region, as shown in Figure 2.1(b). Besides charge balancing, the space charge effect is reduced in the PDA structure relative to PINs because the depleted absorber is thinner. The drawback of PDA photodiode is that a narrow band absorber is used as the drift region, which is the same as a PIN photodiode, which renders it susceptible to thermal

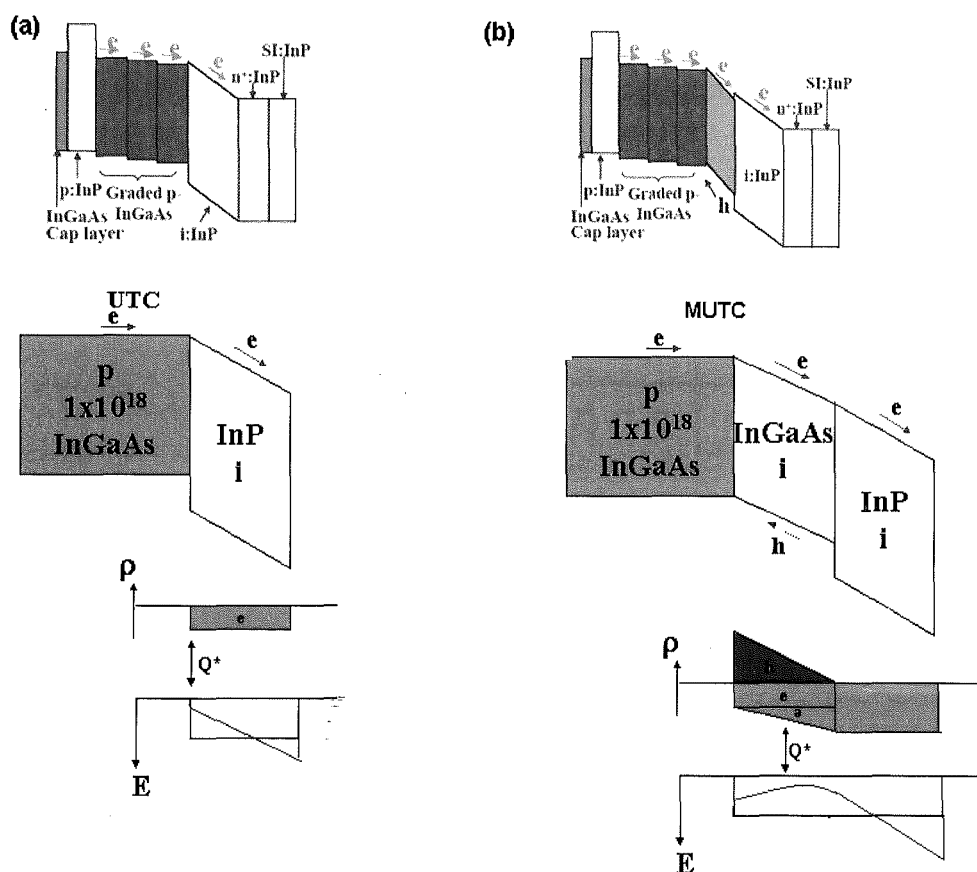


Figure 2.2 Schematic, carrier distribution and electric field distribution of (a) UTC photodiodes and (b) MUTC photodiodes

failure and space charge degradation, although to a lesser extent than the PIN structure.

In contrast, the uni-traveling-carrier (UTC) photodiode utilizes an undepleted p-type layer to absorb light and inject electrons into a wide-bandgap depleted drift region, as shown in Figure 2.2(a). This type of photodiode structure was first introduced by C.R. Davis et. al. to reduce the dark current of photodiodes in 1996 [12]. T. Ishibashi et al. [3] first demonstrated the potential of this structure, which they referred to as a uni-traveling carrier (UTC) photodiode, to achieve high operating current (high RF output power) at high bandwidths. The UTC structure has three advantages. First, only electrons transit the depleted drift region, which significantly suppresses the space charge effect. Second, there is a bandwidth enhancement because only electrons transit the depletion region and electrons have higher saturation velocity in InP than in InGaAs. Third, a wide band absorber is used as the drift region, which lowers the dark current and makes the photodiode less susceptible to thermal failure. In the original design of the UTC, some space charge remains owing to single carrier injection. This causes the electric field to collapse at the edge of the depleted region at high optical power levels, which limits the RF output power. One issue for the UTC is the performance tradeoff associated with the thickness of the absorber, which is entirely undepleted. If the layer is thick, a high fraction of the incident light can be absorbed, which will yield high responsivity. However, the time required for the photogenerated electrons to diffuse to the wide-bandgap collector can significantly limit the bandwidth if the undepleted absorber is thick. In order to circumvent this problem, variations of original UTC photodiode have been developed. the charge-compensated UTC (CC-UTC) photodiode utilizes an InP electron drift layer that is slightly n-doped so as to compensate the space charge effect caused by the photo-

generated electron [13], i.e., the electric field is “pre-distorted” so that a flat field profile can be achieved at high photocurrent levels. Another structure, the modified UTC (MUTC), combines the advantages of the PDA and UTC structures [5]. The MUTC narrow-bandgap absorber has an undepleted p-type region and a depleted layer and a wide-bandgap depleted drift region [14], as shown in Figure 2.2(b). In this structure, space charge in the intrinsic InGaAs layer is relatively small owing to the fact that it is thin. The depleted wide-bandgap (usually InP) collector has the advantages of reducing the capacitance and high electron saturation velocity. The thickness of the undepleted absorber, depleted absorber and the electron drift layer can be adjusted separately besting order to achieve high bandwidth, high responsivity and high RF output power. This dissertation will focus on UTC-type photodiodes owing to their combination of high bandwidth and excellent power handling capability.

2.3 Saturation Mechanisms in Uni-Traveling-Carrier Photodiodes

If heat dissipation is not an issue, the power handling capability of photodiodes is mainly limited by the space-charge saturation effect. As described in Section 2.2, saturation in PIN and PDA photodiodes occurs because the electric field in the depleted absorber collapses below the level required to sustain the electron and hole saturation velocities as the optical power increases. Although this space charge effect also exists in UTC type of photodiodes, the saturation mechanism of UTC type of photodiodes is slightly different from PIN or PDA photodiodes. In PIN and PDA photodiodes the InP layers are heavily doped; there is no charge accumulation at the InGaAs/InP heterojunc-

tions. However, in UTC-type photodiodes, the InP electron drift layer is undoped. It follows that if the field at the interface between the InGaAs absorber and the InP drift layer is too low, electrons can be trapped by the heterojunction barriers in the conduction band. This will lead to degradation of the bandwidth because the trapped carriers escape by thermionic emission, a slow process, and reduced responsivity if the carriers recombine through interface defect levels before they enter the drift layer.

In order to further study the saturation mechanisms in UTC type of photodiodes, measurements and simulations are carefully carried out on the charge compensated MUTC (CC-MUTC) photodiode reported in [15]. The device structure was grown on semi-insulating double-side-polished InP substrates by metal organic chemical vapor deposition (MOCVD). As is shown in Figure 2.3, the depletion region consists of a 605 nm InP depletion layer, two 15 nm undoped InGaAsP “bandgap smooth” layers, and a

| |
|--|
| InGaAs, p ⁺ , Zn, 2.0×10^{19} , 50nm |
| InP, p ⁺ , Zn, 3×10^{18} , 1000nm |
| InGaAs, Zn, 2×10^{18} , 100nm |
| InGaAs, Zn, 1×10^{18} , 150nm |
| InGaAs, Zn, 5×10^{17} , 200nm |
| InGaAs, Zn, 2.5×10^{17} , 200nm |
| InGaAs, Si, 1.0×10^{16} , 200nm |
| InGaAsP, Q1.4, undoped, 15nm |
| InGaAsP, Q1.1, undoped, 15nm |
| InP, Si, 1.0×10^{16} , 605nm |
| InP, n ⁺ , Si, 1.0×10^{19} , 1000nm |
| InGaAs, n ⁺ , Si, 1.0×10^{19} , 20nm |
| InP, n ⁺ , Si, 1.0×10^{19} , 200nm |
| InP, semi-insulating substrate, Double side polished |

Figure 2.3 Schematic of InGaAs/InP CC-MUTC photodiode

200 nm depleted InGaAs absorbing layer. The depleted region was slightly n-doped to compensate the space charge. To help carrier transport in the doped absorbing layer, the doping levels of the p-doped $\text{In}_{0.53}\text{Ga}_{0.47}\text{As}$ absorbing region was graded in four steps ($2.5 \times 10^{17} \text{ cm}^{-3}$, $5 \times 10^{17} \text{ cm}^{-3}$, $1 \times 10^{18} \text{ cm}^{-3}$, and $2 \times 10^{18} \text{ cm}^{-3}$) to create a quasielectric field. Back-illuminated mesa structures were fabricated on the wafer and microwave contact pads were fabricated for high-speed measurements. A 220 nm SiO_2 layer was deposited on the back of the wafer as anti-reflection coating. This photodiode has a responsivity of 0.75 A/W at 1.55 μm wavelength.

Since photodiodes saturate at low current for low bias voltage, the RF power and responsivity were measured for a 34- μm -diameter photodiode at zero bias from low-level to high-level optical injection. The measured RF power peaks at about 8 mW of incident

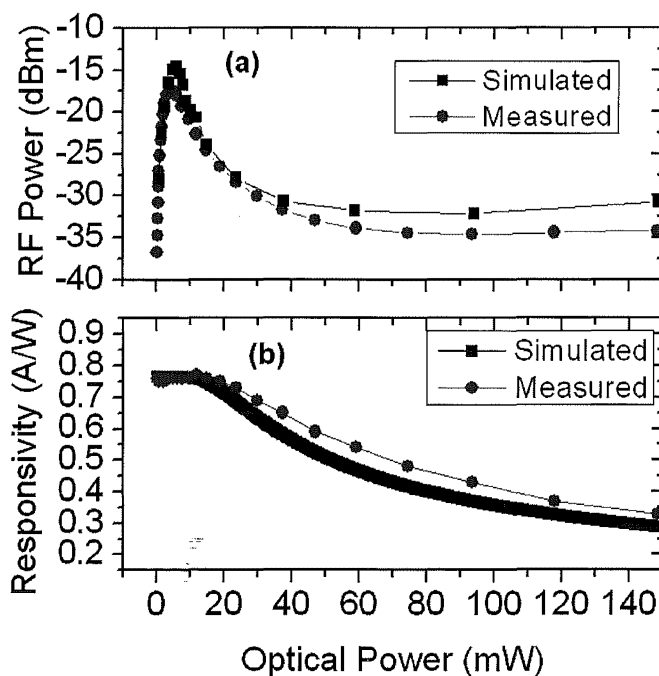


Figure 2.4 Measured and simulated (a) RF output power versus optical power and (b) responsivity versus optical power at zero bias.

optical power and then decreases with input optical power. The measured responsivity remains constant at 0.75 A/W when the optical power is small and begins to decrease near 18 mW as shown in Figure 2.4. This phenomenon is replicated by our commercial device simulator APSYS based on the drift-diffusion model. A 50 Ω load resistor and a series resistance of 5.6 Ω were used in the simulation. Thermal effects are also considered following the experiment data [16]. In general, the simulated results agree well with the measured values.

In order to study the origin of responsivity degradation, the electrical field profiles in the photodiode were simulated at zero bias for different optical injection levels. Figure 2.5(a) shows that as the optical power increases, the electric field in the depleted InGaAs absorption layer decreases due to the screening caused by the photo-generated electrons and holes, i.e., the space-charge effect described above. As a consequence, the band discontinuity in the conduction band at the step graded interface between the InGaAs layer and the InP layer become more pronounced and behaves as a barrier to impede electron transport from the absorption region, as shown in Figure 2.5(b); this results in reduced responsivity. A similar effect has been reported for UTC photodiodes [17]. This explains the falloff in the responsivity of the CC-MUTC devices at \sim 18 mW and the falloff in the RF power at 8 mW.

Since both RF power saturation and decrease in responsivity are caused by the space charge effect, the photocurrent at which the responsivity begins to degrade is an indicator of the power handling capability of the photodiode. As a result of the self-induced field, the responsivity frequently increases slightly with photocurrent at low optical injection levels for UTC-type of photodiodes and then decreases when the space charge effect becomes pronounced. In the following sections we refer to the photocurrent at which the responsivity reaches its peak as the “critical current”. Since the saturation current is more difficult to simulate, in the next section we will evaluate the “degradation current” to estimate the ability of a photodiode to sustain high optical injection.

2.4 The Role of Cliff Layer

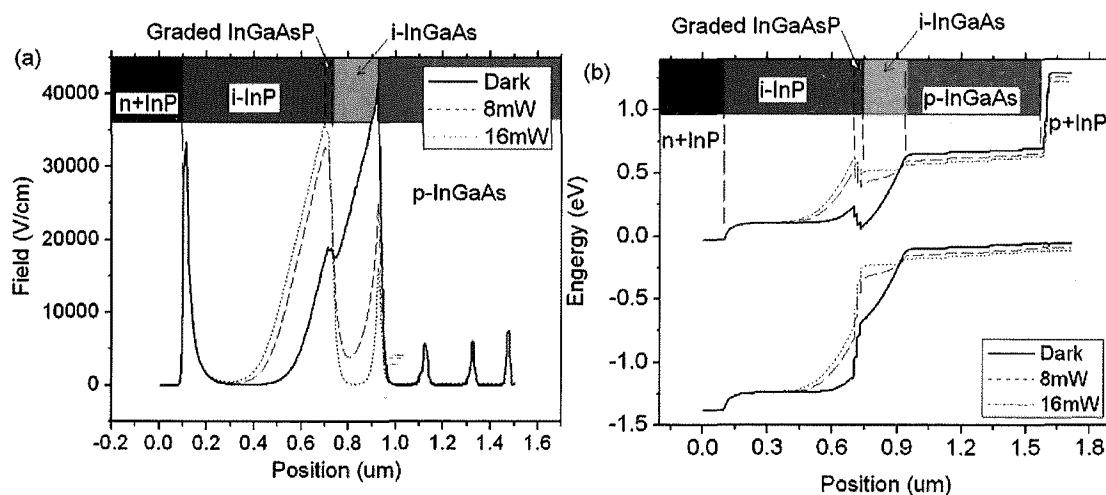


Figure 2.5 Simulated (a) electric field and (b) bandgap diagram at various optical injection levels.

A "cliff layer" is a thin, moderately-doped n-type InP layer between the semi-intrinsic InGaAs layer and the charge-compensated InP layer in UTC type of photodiodes. The cliff layer was introduced into the UTC structure soon after its invention [18]. However, the importance of cliff layer was not clearly defined and there have been few studies related to its optimization. This section presents simulations that show how the cliff layer helps to reduce the saturation effect. In all the simulations, we have assumed that the photodiodes have diameter of 34 μm , a reverse bias of 5 V, and that the temperature of the photodiodes is fixed at 300 K. First, an InP cliff layer is added to the CC-MUTC photodiode shown previously in Figure 2.3. The InP cliff layer is 5 nm thick and

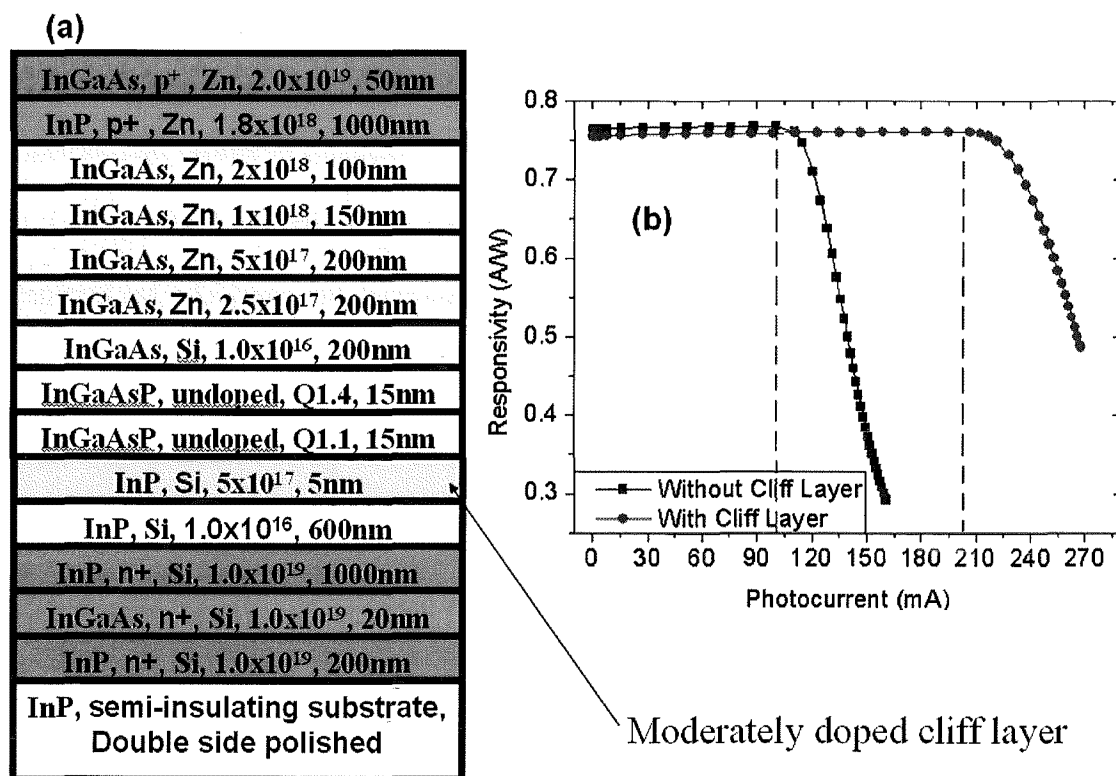


Figure 2.6 (a) Schematic of InGaAs/InP CC-MUTC photodiode with a cliff layer; (b) The responsivity versus photocurrent curve for CC-MUTC photodiodes with and without cliff layer

doped to $5 \cdot 10^{17} \text{ cm}^{-3}$, as shown in Figure 2.6(a). The current-dependent responsivities of the CC-MUTC photodiodes with and without the cliff layer are shown in Figure 2.6(b). The responsivity of the original structure begins to decrease at a photocurrent of 100 mA whereas that with the cliff layers is constant up to 200mA, a significant improvement. Although the degradation current is calculated under isothermal condition, these results provide useful insights to the importance of the cliff layer in improving the power handling capability of UTC-type of photodiodes.

Further simulations were carried out to understand the reasons why the cliff layer can reduce the saturation.. When the optical power is 235 mW, the electric field in the intrinsic InGaAs layer of the original CC-MUTC photodiode has almost completely collapsed, as can be seen in Figure 2.7(a). However, when the cliff layer is added, the electric field profile is modified such that the electric field in the depleted InGaAs layer is significantly enhanced. In other words, the cliff layer increases the electric field in the depleted InGaAs layer and decrease that in the intrinsic InP layer. This effect can be also be seen clearly in the energy diagram. When the optical power is 235 mW, the energy band of the device without a cliff layer has already flattened out and the barrier at the heterojunction interface blocks many of the electrons from getting into the InP collector. However, after the cliff layer is added, electron transport is enhanced due to higher electric field in the intrinsic InGaAs layer, as shown in Figure 2.7(b).

The electric field in the depleted InGaAs absorption layer is increased by the cliff layer. In this sense, the higher the charge in the cliff layer, whether by increased thickness or doping level, the less susceptible the photodiode is to the space charge effect. However, it should be noted that this is accompanied by a decrease in the electric field in the depleted InP layer and when the electric field in this region is very low, the frequency response will be impaired. The electric field distribution in CC-MUTC photodiode has also been simulated for different cliff layer thicknesses and doping levels. The results are shown in Figure 2.8. When the doping level of this cliff layer is fixed to $5 \times 10^{17} \text{ cm}^{-3}$, the semi-intrinsic InP layer is fully depleted for a thickness of 5nm, but full depletion cannot be maintained as the thickness increases to 10nm. We find that for the CC-MUTC, the thickness of the cliff layer should be no more than 10 nm if the doping level is $5 \times 10^{17} \text{ cm}^{-3}$, or the total charge in the cliff layer should be no more than $5 \times 10^9 \text{ cm}^{-2}$ in order to achieve the maximum power handling capability while maintaining the bandwidth of the photodiode. For UTC-type of photodiodes in general, the design rule for the cliff layer is

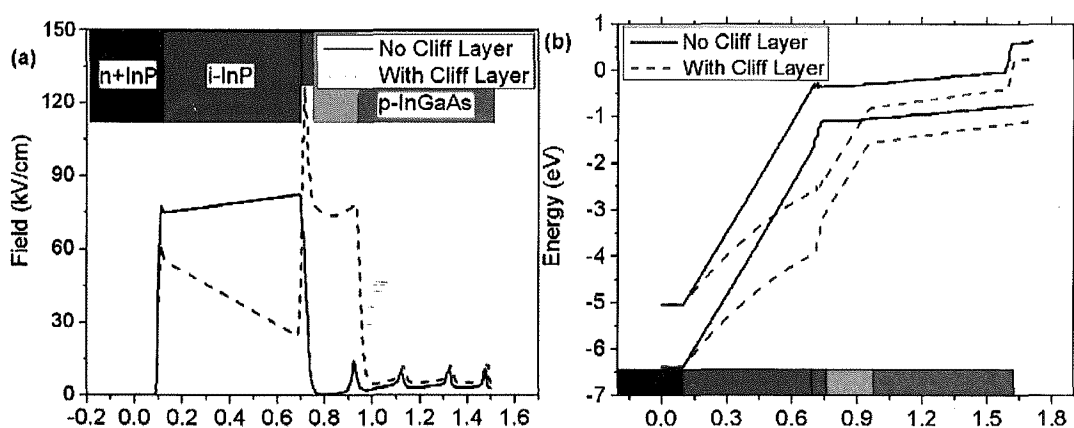


Figure 2.7 (a) electric field and (b) energy band diagram of the CC-MUTC photodiodes with and without cliff layer

that the total charge in the cliff layer should be as high as possible until the InP electron drift layer cannot maintain full depletion.

2.5 Conclusion

In this chapter several photodiode structures for high power applications have been reviewed. The saturation mechanisms in UTC-type of photodiodes are investigated through both simulations and measurements on a CC-MUTC photodiode. It was found that the primary reason for saturation is that the bandgap discontinuity impedes electron transport into the InP drift layer when the electric field in the intrinsic InGaAs absorber collapses due to the space charge effect. A cliff layer is found to be helpful to reduce the saturation effect in UTC-type photodiodes by enhancing the electric field in the depleted InGaAs layer and reducing that in the InP electron drift layer. The general design rule for the cliff layer is that the total charge in the cliff layer should be as high as possible until

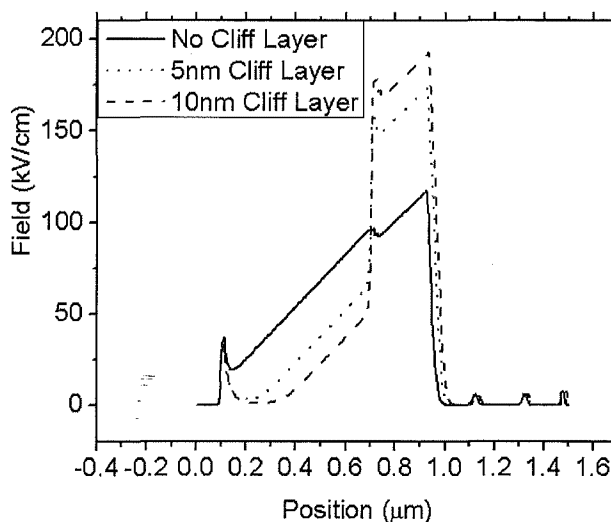


Figure 2.8 electric field in the CC-MUTC photodiodes with cliff layers of different doping levels

the InP electron drift layer cannot maintain full depletion so that the power handling capability of the photodiode can be maximized while the bandwidth of the photodiode can still be maintained.

Chapter 3 Characterization of Photodiode Linearity

3.1 Introduction

The spur-free dynamic range (SFDR) is a uniquely important figure of merit for analog optical links because, unlike other performance parameters such as loss or noise figure, SFDR can not be improved by adding pre- or post-amplification [19]. The SFDR is usually characterized using a two-tone method. Assume that the input of the link consists of two equal-power fundamental frequencies. The two-tone SFDR is defined as the signal-to-noise ratio at the link output when the power of the intermodulation distortion products equal the noise. Among all the intermodulation products and harmonics, the third order intermodulation products (IMD3) at $2f_1 - f_2$ and $2f_2 - f_1$ are important, because they are close to the fundamental frequencies f_1 and f_2 and thus difficult to be filtered, as shown in Figure 3.1(a). The third-order output intercept point (OIP3) is a key figure of merit to evaluate the linearity of an analog optical link; it is defined as the extrapolated

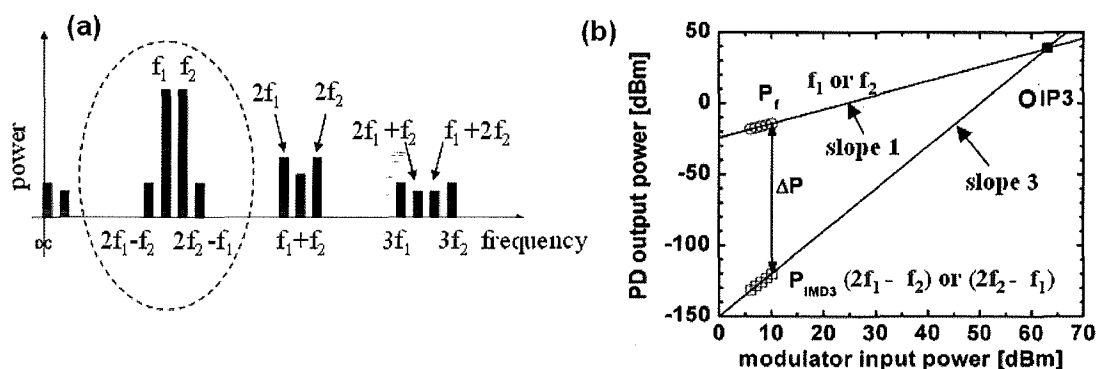


Figure 3.1 (a) Schematic of fundamentals and IMD3 (b) The definition of OIP3

intercept point of the power of fundamental frequency and IMD3, assuming that the fundamental power has a perfect slope of 1 and the power of IMD3 has a perfect slope of 3, as shown in Figure 3.1(b). Based on its definition, OIP3 can be calculated from the measured fundamental power and the power of IMD3 with this simple equation [8]:

$$OIP3 = P_f + \frac{1}{2}(P_f - P_{IMD3}) \quad (0.1)$$

where P_f is the power of the fundamental frequency and P_{IMD3} is the power of the IMD3. As discussed in Chapter 1, the photodiode is frequently the limiting factor for the linearity performance of an analog optical link. Thus in this thesis I have focused on characterization and behavior of OIP3 of photodiodes.

3.2 Conventional Two-Tone Setup

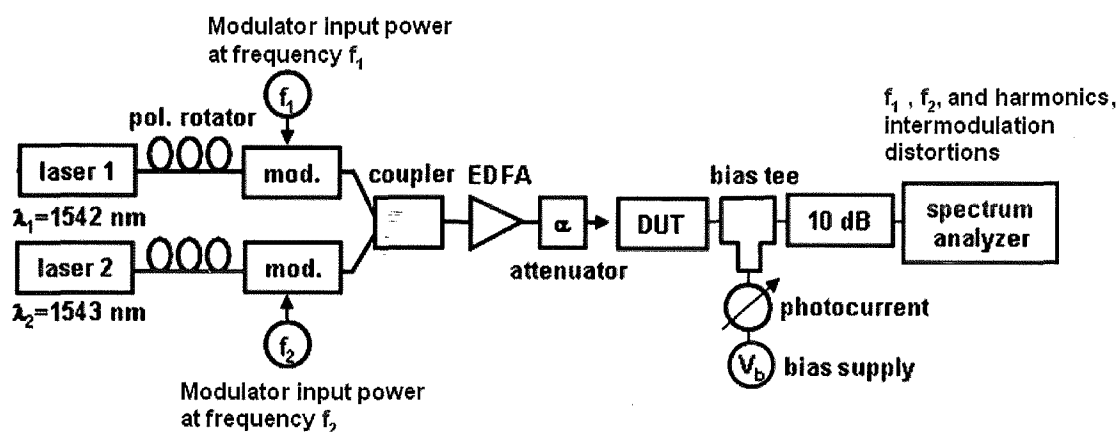


Figure 3.2 Schematic of conventional two-tone measurement setup

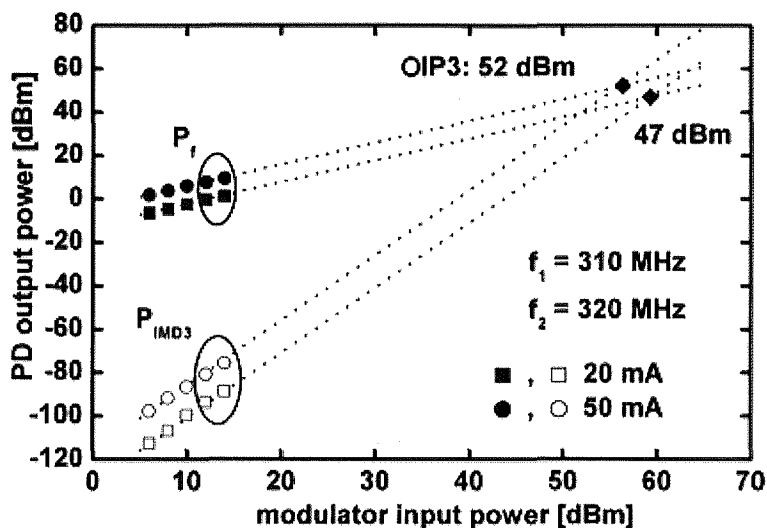


Figure 3.3 Measurement of OIP3 of CC-MUTC at 20 mA and 50 mA

The two-tone setup is a widely used apparatus to measure the dynamic range of an analog optical link [20]. To measure IMD3 we employed a two-tone setup operating near $1.55 \mu\text{m}$ wavelength, as shown in Figure 3.2. The optical source was two distributed feedback lasers that were externally modulated at frequencies f_1 and f_2 by Mach-Zehnder modulators. To minimize the influence of second-order harmonic effects originating in the modulators the modulation depths were maintained at low values (approximately 24%). The two optical signals were combined, amplified by an erbium-doped fiber amplifier (EDFA) and launched into the chip utilizing a lensed fiber. By increasing slightly the distance between fiber and chip the spot size was expanded to overfill the active area, which results in more uniform illumination. A reverse voltage, V_b , was applied to the photodiode through a bias-tee in the RF path. The output signals P_f at the fundamental frequencies f_1 and f_2 and the IMD3 P_{IMD3} at $(2f_2-f_1)$ and $(2f_1-f_2)$ were detected with a spectrum analyzer. The Agilent E4440A RF spectrum analyzer that was used for this study has an $\text{OIP3} \geq 18 \text{ dBm}$ up to 6 GHz. Using a total RF attenuation of

50 dB (40 dB internal RF attenuation in the spectrum analyzer and 10 dB external RF attenuator), the setup can measure OIP3 up to 68 dBm. The measured data were calibrated taking the losses of the components in the RF path into account.

Using the two-tone measurement setup described above, we measured the OIP3 of the CC-MUTC photodiodes shown in Figure 2.3. Figure 3.3 shows that when increasing the modulator input power and thus the modulation depth of the optical signal, the fundamental power follows the slope of 1 and the IMD3 follows the slope of 3, which indicates that the measured OIP3 is independent of the modulation depth. OIP3 has slight dependence on photocurrent, and it increases from 47 dBm at 20 mA to 52 dBm at 50 mA. Both measurements are carried out under a reverse bias of 7 V.

3.3 Problems with Two-Tone Setup

The nonlinearities of the optical modulators can influence the measurement of photodiode nonlinearities because the second-order harmonics from the modulators, $2f_1$ and $2f_2$, will mix in the photodiode with the fundamental signals f_1 and f_2 and contribute to the IMD3 at $(2f_2-f_1)$ and $(2f_1-f_2)$. Detailed calculations are carried out to verify the influence of the modulators. The transfer function of a Mach-Zehnder modulator is

$$P_{M,O} = \frac{1}{2} \left(1 + \cos \left(\frac{\pi V_M}{V_\pi} \right) \right)$$

assuming no insertion loss, where V_π is the half-wave voltage

for the Mach-Zehnder modulator and V_M is the voltage applied to the modulator. Expanding this transfer function near $V_M=V_{M0}$ using Taylor's expansion yields:

$$p_{M,o} = \frac{1}{2} \left(1 - \frac{\pi}{V_\pi} \sin \left(\frac{\pi V_{M0}}{V_\pi} \right) (V_M - V_{M0}) - \frac{1}{2} \left(\frac{\pi V_{M0}}{V_\pi} \right)^2 \cos \left(\frac{\pi V_{M0}}{V_\pi} \right) (V_M - V_{M0})^2 \right). \quad (3.1)$$

We focus on the second harmonics from the modulators, because they contribute to the IMD3 in the output of the two-tone measurement. Therefore only the first two terms in the Taylor's expansion are used. From the equation we can see that if $V_{M0} = (k + \frac{1}{2})V_\pi$,

where k is an integer, the transfer function becomes $p_{M,o} = \frac{1}{2} \left(1 - \frac{\pi}{V_\pi} (V_M - V_{M0}) \right)$, which

is a linear function. Thus $V_{M0} = (k + \frac{1}{2})V_\pi$ is called the quadrature point and a modulator will have zero second-order harmonic when biased at this quadrature point.

However, in reality, the modulator can not be biased exactly at the quadrature point due to the finite accuracy of the voltage source. Therefore, the second harmonic produced by the modulator is not zero. The following illustrates how the harmonics produced by the modulators due to the deviation of the bias from the quadrature point can influence the two-tone measurement results. We assume that the optical signal after modulated by

the modulator is $P(t) = \frac{1}{2} \left(1 + \cos \left(\pi \frac{\frac{1}{2}V_\pi + \Delta V + V_M(t)}{V_\pi} \right) \right)$, where ΔV is the deviation of

bias voltage from ideal quadrature point, and $V_M(t) = V_M[\sin(2\pi f_1 t) + \sin(2\pi f_2 t)]$ is the input RF signal applied to the modulator, which is comprised of two sinusoidal signals with different frequencies. Assume that the photodiode has an arbitrary nonlinear transfer function of $I(t) = R[P(t) + a_1 P^2(t) + a_2 P^3(t)]$ with $R=1A/W$, $a_1=0.8$, and $a_2=0.2$. The

photocurrent dependence of the power of the fundamental tone and the IMD3 can be calculated from the Fourier transform of $I^2(t)$ and the results are shown in Figure 3.4.

The modulator contributes to the IMD3 in the way that the second order harmonic of the first tone, $2f_1$, mixes with the fundament of the second tone, f_2 , in the photodiode. The result is a contribution to the IMD3 at the frequency of $2f_1-f_2$. On the other hand, the photodiode contributes to the IMD3 because the two fundamental frequencies f_1 and f_2 directly mix in the photodiode to create a signal at $2f_1-f_2$. Thus when the output RF power from the photodiode increases, the IMD3 contributed by modulator increases at a slope of 4 with logarithmic photocurrent, while the IMD3 contributed by the photodiode exhibits

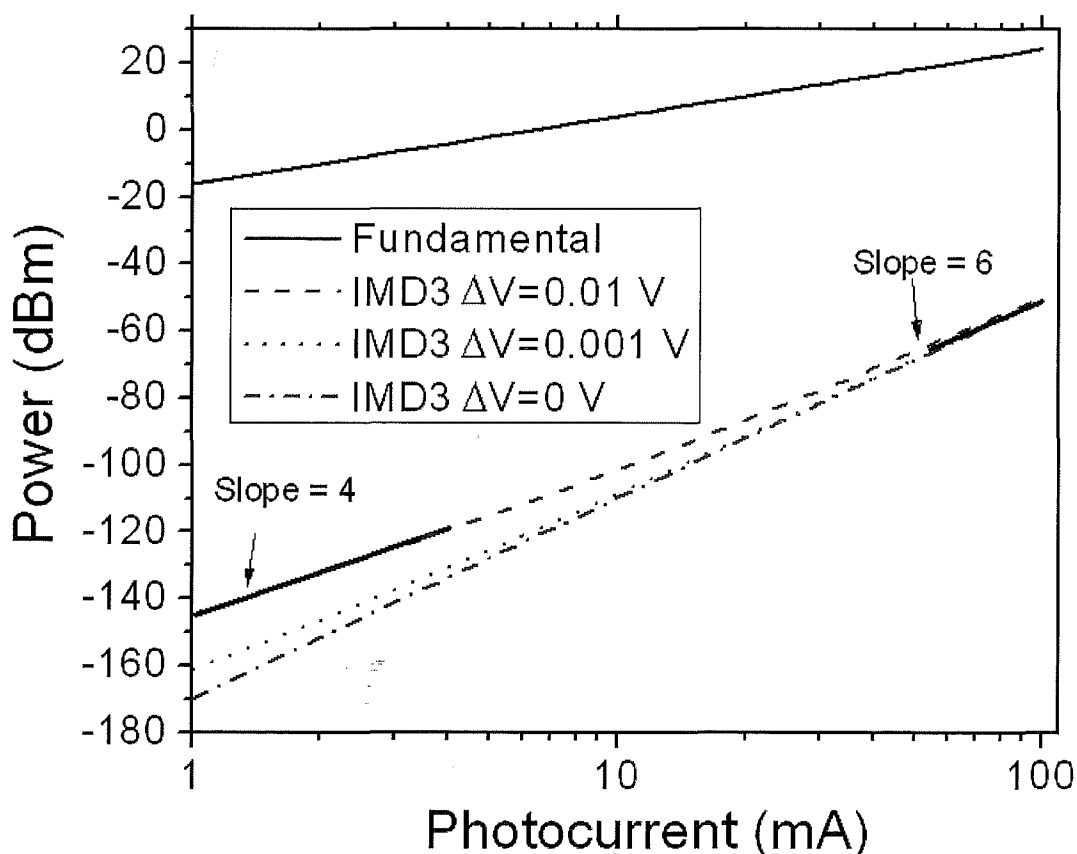


Figure 3.4 Fundamental and IMD3 produced by the modulator and the photodiode with different deviations from quadrature point.

a slope of 6. Thus if the IMD3 increases with a slope of 4 logarithmically with photocurrent, the modulator is the source of the IMD3 in the analog optical link; if the IMD3 increases with a slope of 6 the IMD3 originates in the photodiode. When $\Delta V = 0$, which means that the modulator is perfectly biased at the quadrature point, the IMD3 is produced only by the nonlinearity of the transfer function of the photodiode. In Fig. 3.4, we see that when the fundamental power is -18 dBm, the power of IMD3 is -170 dBm, which corresponds to an OIP3 of $[-18 + 0.5 \cdot (-18 + 170)] = 58$ dBm. The fundamental power increases at a perfect slope of 2 with logarithmic photocurrent and the power of IMD3 increases at a perfect slope of 6. The larger the voltage deviation from the ideal quadrature point, the larger is IMD3 contributed by the modulator, as shown in Figure 3.4. However, since the IMD3 contributed by the modulator increases with a slope of 4, which is slower than the IMD3 contributed by the photodiode, as the photocurrent approaches 70 mA the IMD3 contributed by the photodiode becomes the dominant limiting factor for all three cases shown in Figure 3.4.

From the discussion above, we can see that the second harmonics produced by modulators can influence the measurement results in a conventional two-tone setup. Two measures can be taken to minimize the influence of the second harmonics from the modulators. One is to bias the modulators as accurately at the quadrature point as possible and the other is to operate the photodiode at high photocurrent.

3.4 Three-Tone Setup

It has been suggested that a three-tone technique is more accurate for photodiode nonlinearity measurements because the three-tone approach is free of the influence of second harmonics produced by the modulators [21]. A disadvantage, however, is the requirement for an additional laser, signal generator and modulator. Figure 3.5 shows a block diagram of the three-tone measurement apparatus. Compared to the two-tone setup shown in Figure 3.2, a laser source and external modulation at frequency f_3 are added to the setup. The three optical signals are combined with a four-way optical combiner and amplified by an erbium-doped fiber amplifier (EDFA), which is followed by an optical attenuator. The signal is launched into the chip with a lensed fiber. If the third laser source is turned off, this three-tone measurement setup is the same as the two-tone setup. For two-tone measurements, the output RF power P_f at the fundamental frequencies f_1 , f_2 and the power of IMD3, P_{IMD3} , at $(2f_2-f_1)$ and $(2f_1-f_2)$ are measured. The two-tone OIP3 is defined as $\text{OIP3} = P_f + (P_f - P_{\text{IMD3}})/2$ dBm. For the three-tone measurement, the output RF power P_f at the fundamental frequencies f_1 , f_2 , f_3 and the power of IMD3, P_{IMD3} , at $(f_1+f_2-f_3)$, $(f_2+f_3-f_1)$, $(f_3+f_1-f_2)$ are measured. The three-tone IMD3 is 6dB larger than the ideally

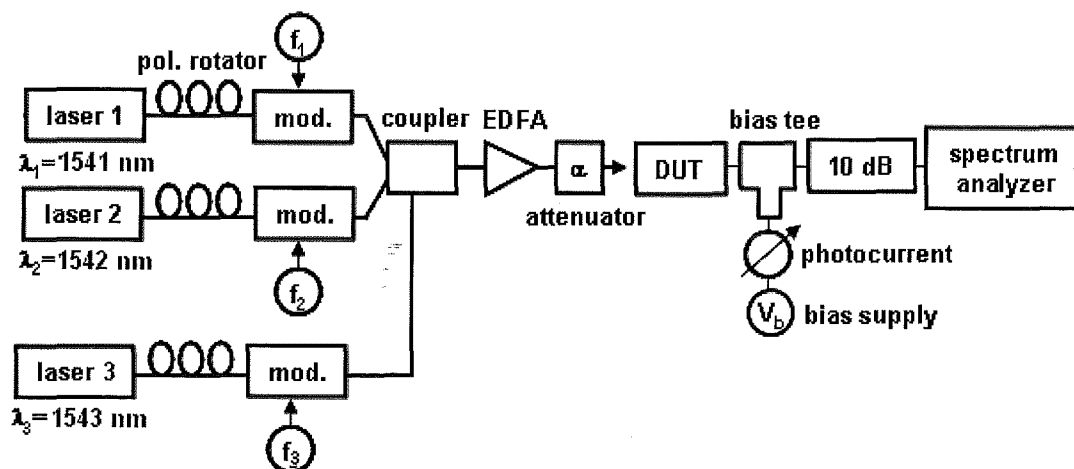


Figure 3.5 Experimental setup for three-tone measurements.

measured two-tone IMD3 [22]. This difference in IMD3 can be understood from the fact that the coefficient of $\cos(\omega_i t + \omega_j t - \omega_k t)$ ($i, j, k=1, 2, 3$ $i \neq j \neq k$) is 2 times as large as that of $\cos(2\omega_i t - \omega_j t)$ ($i, j=1, 2, 3$ $i \neq j$) after expanding the expression $[\cos(\omega_i t) + \cos(\omega_j t) + \cos(\omega_k t)]^3$ ($i, j, k=1, 2, 3$ $i \neq j \neq k$). If the three-tone OIP3 is defined analogously to the two-tone OIP3, then, following the approach in [22], a factor of 3dB should be added to the measured three-tone OIP3 in order to compare with the two-tone measurements.

Using these measurement conditions, the OIP3 of the CC-UTC photodiode reported in [23] was measured at 310 MHz with both the two-tone setup and the three-tone setup. For the two-tone setup the two lasers were modulated at $f_1=320.7$ MHz and $f_2=311.1$ MHz. The biases of the modulators are carefully tuned to minimize the second harmonics from the modulators. Figure 3.6 shows the bias dependence of the OIP3. The measurement was then repeated with the three-tone setup. The total output optical power

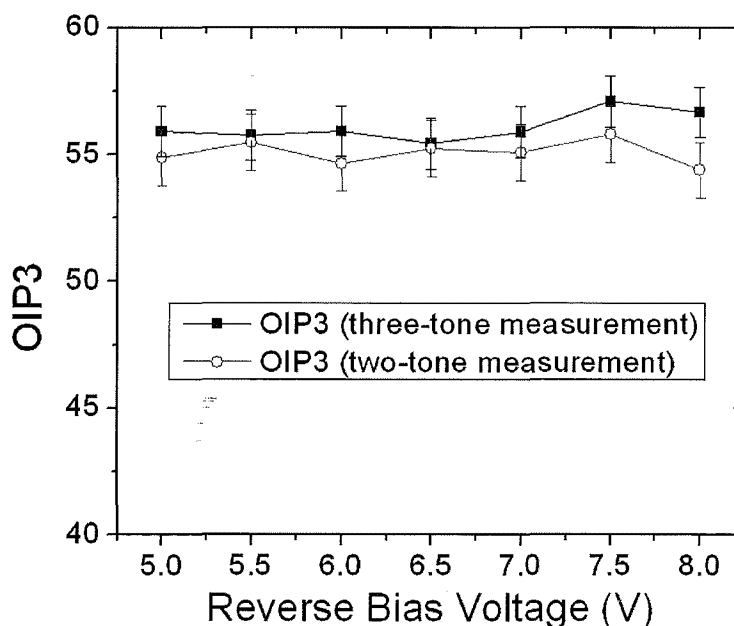


Figure 3.6 Voltage-dependence of OIP3 measured by two-tone and three-tone setups.

from the EDFA was kept constant so that the photocurrent was fixed at 60 mA for both two-tone and three-tone measurements. The modulation frequency and modulation depth of the third laser were $f_3=300.7$ MHz and 24%, respectively. As shown in Figure 3.6, the two-tone and the three-tone techniques yield consistent results. The values of the intermodulation terms exhibit a fluctuation of approximately ± 1 dB, as indicated by the error bars in Figure 3.6, which originate from fluctuations in the IMD3 power and the differences in the calculated values that result from measuring at different fundamental and IMD3 frequencies. The OIP3 values measured by the three-tone method are, on average, slightly higher than those measured by the two-tone method, which suggests that the two-tone measurement may still exhibit residual effects from modulator nonlinearities when the OIP3 of photodiodes reaches above 55 dBm.

3.5 Bias Modulation Setup

In two-tone or three-tone measurements, the measured intermodulation distortions are produced by numerous types of nonlinearities in the photodiode. Broadly these can be categorized as voltage-dependent and photocurrent-dependent nonlinearities. It is difficult to identify the contribution to the intermodulation distortions from each nonlinear phenomenon separately. In order to study only the effect of voltage-dependent nonlinearity of the MUTC photodiodes, a modulated bias measurement setup that we have developed will be described in this section.

The output of a distributed feedback laser is externally modulated at a frequency f_1 by a Mach-Zehnder modulator. The modulated optical signal is amplified by an EDFA and launched into the photodiode chip utilizing a lensed fiber. Similar to two-tone and three-tone measurements, the distance between fiber and chip is increased slightly to ensure uniform illumination. An alternating sinusoidal reverse voltage, V_{bias} , at frequency f_2 is produced by a low-frequency signal generator. For this work, f_2 is 20 kHz. This signal is applied to the photodiode through a bias-tee with a low frequency cut-off of 45 MHz. After 10 dB attenuation, the RF output signals are detected with a spectrum analyzer, which displays the fundamental frequency, f_1 , and the second intermodulation distortion (IMD2) at frequencies $f_1 \pm f_2$, P_{IMD2} , and the third intermodulation distortion (IMD3) at the frequency $f_1 + 2f_2$, P_{IMD3} . The power at frequency f_2 is as low as -91 dBm in all measurements since the bias-tee effectively blocks this low-frequency modulated bias voltage signal from the spectrum analyzer. The measured data were calibrated taking the losses of the components in the RF path into account.

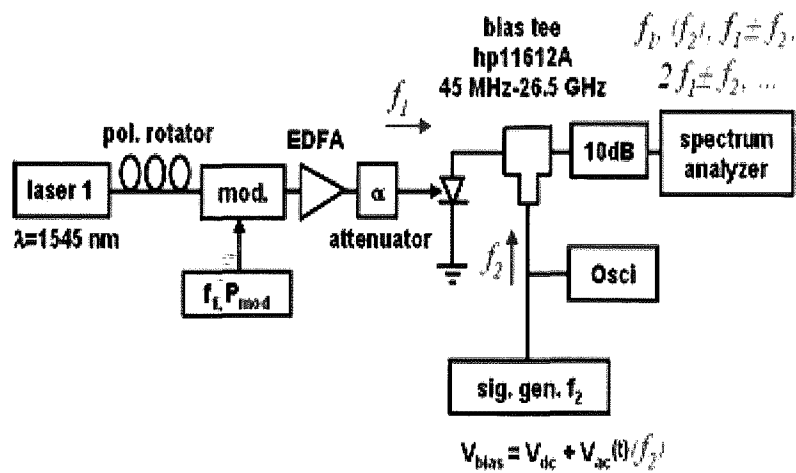


Figure 3.7 Experimental setup bias modulation measurements.

Bias modulation measurements were carried out on the CC-MUTC photodiode shown in Figure 2.3. The reverse voltage V_{bias} was composed of an average voltage, V_{dc} , and an AC peak-to-peak voltage of 2V. The average photocurrent was set to 10 mA to ensure an unsaturated output at the fundamental frequency. The measured intermodulation products for the fundamental frequency $f_1=3.5$ GHz are plotted versus the fundamental power in Figure 3.8. The measured data points of P_{IMD2} and P_{IMD3} can be well fit by straight lines with slopes of 1, which indicates that the intermodulation distortions are independent of the applied modulation depth. It is not surprising that both P_{IMD2} and P_{IMD3} increase linearly with the fundamental power instead of the power law observed for the two-tone measurement, since the power of the second tone at the frequency f_2 does not change with the fundamental optical power P_{f_1} . Since the IMD2 and IMD3 in this bias modulation setup are only produced by the modulated bias signal, the nonlinear process only involves the voltage-dependent nonlinearities; all the other nonlinear

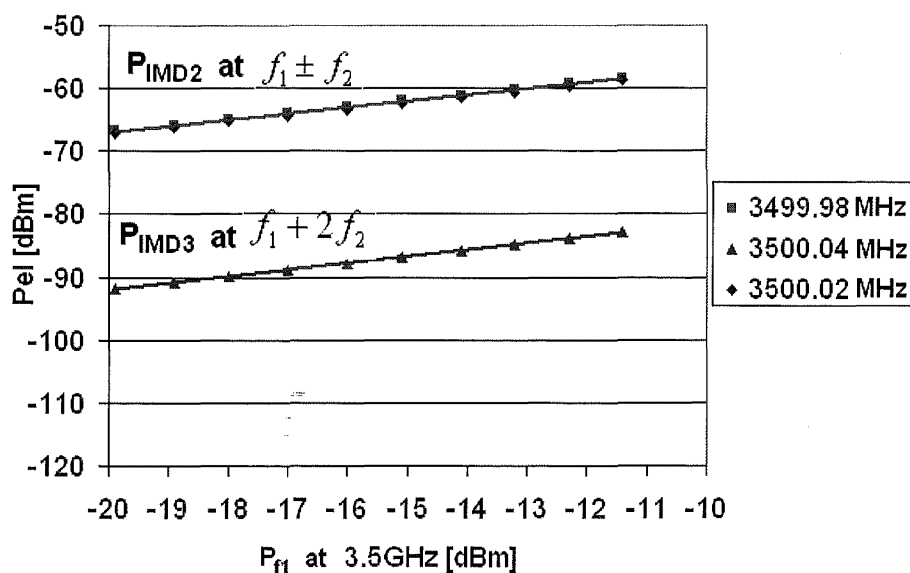


Figure 3.8 IMD2 and IMD3 vs. fundamental power for CC-MUTC at 10 mA average photocurrent and 6 V average reverse bias V_{dc} .

mechanisms such as photocurrent-dependent nonlinearities are excluded. Also the nonlinearities from the modulator have no influence on the measured IMD2 and IMD3. In the following chapters I will present more detailed discussions on how bias modulation measurements can help quantitatively identify the influence of voltage-dependent nonlinearities on the OIP3 of photodiodes.

3.6 Conclusion

In this chapter we discussed three important measurement setups to measure photodiode nonlinearities, namely two-tone, three-tone, and the bias modulation measurement techniques. The two-tone setup is relatively simple compared to the three-tone setup and it can measure the OIP3 of photodiodes with good accuracy if the modulator can be accurately biased at the quadrature point and the photocurrent is sufficiently large. The three-tone setup can accurately measure the OIP3 without the influence of modulator nonlinearities. However, an additional laser source, signal generator and modulator are required. The bias modulation setup is also free of the influence of modulator nonlinearities. While it does not directly measure the OIP3 of photodiodes, it does provide valuable insight into voltage-dependent nonlinearities.

Chapter 4 Nonlinear Phenomena in Photodiodes and the Equivalent Circuit Model

4.1 Introduction

In Chapter 3, the intermodulation products have been studied with different measurement techniques. However, the measurement results only reflect the nonlinearity of the photodiodes; they do not explain the origin of the nonlinearities. In Section 4.2 we will quantitatively measure the nonlinear phenomena in CC-MUTC photodiodes. In Section 4.3 the physical origins of those nonlinear phenomena will be explained. In Section 4.4 we will develop an equivalent circuit model that provides excellent fits to the measured OIP3 of CC-MUTC photodiodes. In Section 4.5, the equivalent circuit model is used to optimize the operating wavelength for the highest OIP3 of CC-MUTC photodiodes. In Section 4.6, the equivalent circuit model is used to link the nonlinear phenomena with the bias modulation measurement results on CC-MUTC photodiodes. Finally, Section 4.7 summarizes conclusions on the significance of each nonlinear mechanism.

4.2 Nonlinear Phenomena in Photodiodes

In order to explain the measured intermodulation products of the photodiodes we address four of the principal nonlinear phenomena, namely the voltage-dependent responsivity $R(V)$, voltage-dependent capacitance $C(V)$, photocurrent-dependent responsivity $R(I)$ and photocurrent-dependent capacitance $C(I)$. Quantitative measurements have been carried out on the CC-MUTC photodiode in Figure 2.3. The photocurrent-dependent change in capacitance $C(I)$ of a 34 μm -diameter CC-MUTC photodiode is investigated via 1-port S-parameter measurements under illumination. In this measurement we employed only one un-modulated light source with the photodiode ac-coupled to a 50 GHz network analyzer. Figure 4.1 shows the capacitance extracted from the measured S11 data at 1 GHz. By increasing the photocurrent to 60 mA we

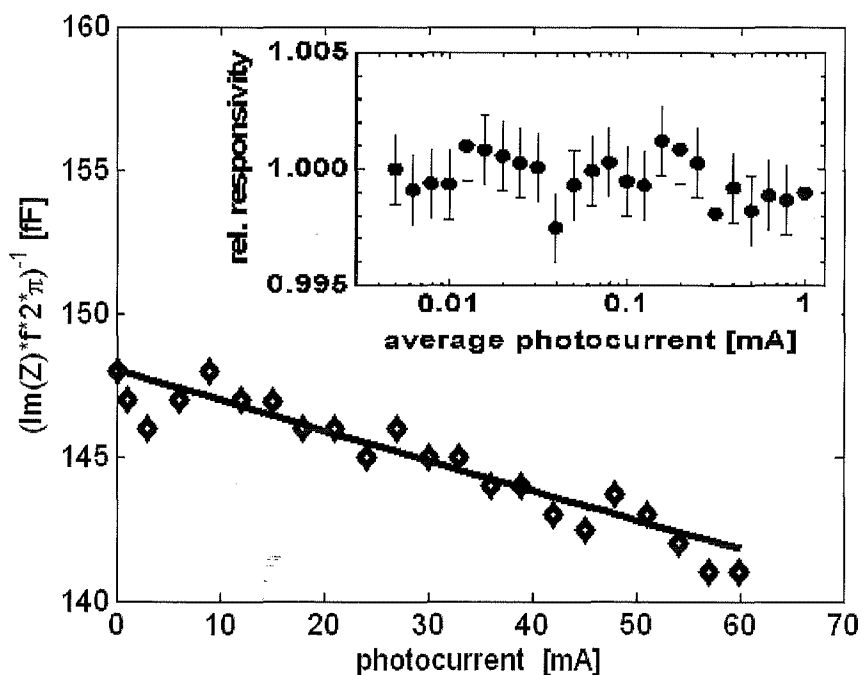


Figure 4.1 Normalized imaginary part of the photodiode impedance (symbols) at $f = 1$ GHz vs. photocurrent with self-consistent simulation (solid line) at reverse bias $V_b = -8$ V. Inset: Measured responsivity normalized to the responsivity at low photocurrent and $V_b = -7$ V.

observe a slight decrease in the capacitance of less than -0.2 fF/mA. Although we only show a 34 μm -diameter device here, we observe similar behavior for devices having different diameters under the condition of uniform illumination. This behavior is contrary to previous results from p-i-n photodiodes [24]. Our simulation of this effect, however, is consistent with our own measurements; a more detailed discussion will be presented in Section 4.3.

The second photocurrent-dependent nonlinear effect is related to the variation of responsivity with photocurrent [25]. We have employed a pulsed laser source at 1545 nm wavelength with a duty cycle of only 1% to avoid slow ohmic heating effects, which can cause a large increase in responsivity with photocurrent [26]. Responsivity is determined

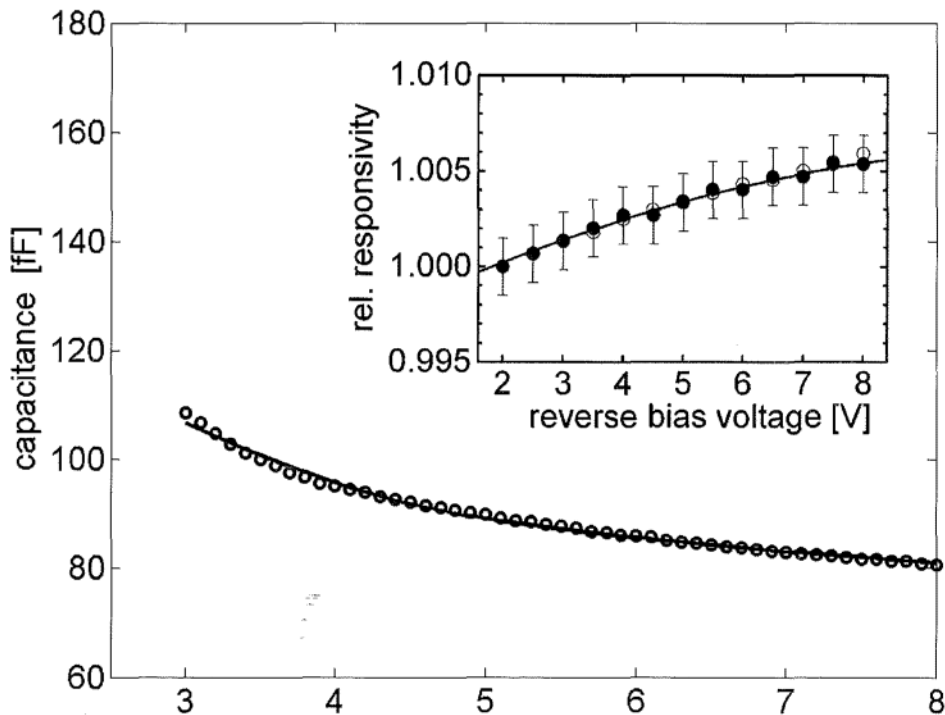


Figure 4.2 Measured photodiode capacitance (symbols) and self-consistent simulation (solid line). Inset: Relative responsivity at -7 dBm (filled circles) and -22 dBm (open circles) average optical power with quadratic polynomial fit function (solid line).

from the ratio of the average photocurrent to optical input power. Up to an average photocurrent of 1 mA, which corresponds to a peak photocurrent of 100 mA, we observed only small fluctuations in responsivity and found no significant correlation between photocurrent and responsivity as shown in the inset of Figure 4.1. Thus we neglect the effect of photocurrent-dependent responsivity in the following analysis.

Further effects to be considered are related to the voltage-dependence of the photodiode capacitance $C(V)$. When operating a reverse biased photodiode under optical illumination, the photocurrent induces a voltage drop across the series and load resistances, which is referred to as the voltage swing effect. As a consequence, the bias voltage across the photodiode junction is reduced and modulated at the signal frequency, which may cause variations in not only the device capacitance, but also in the responsivity. The photodiode capacitance versus voltage was measured with an LCR-meter at 1 MHz. From the results in Figure 4.2 we inferred a differential capacitance of roughly -4 fF/V at high reverse voltages. Simulation of the $C(V)$ curve will be discussed in Section 4.3. Similar to the aforementioned effect, a transient voltage drop across the series and load resistors may also result in a change of responsivity. The inset in Figure 4.2 shows the measured normalized responsivity versus applied reverse bias using the pulsed laser source described above. We observe an increase in responsivity of 0.5 % between 2 and 7 V. A second measurement at a higher optical average power of -22 dBm confirmed the data within the error bars.

4.3 Physical Mechanisms of Nonlinear Phenomena

Nonlinear responsivity and nonlinear capacitance are caused by different physical phenomena. There are two major mechanisms that contribute to the $R(V)$ effect. Modulation of the junction voltage leads directly to variation in the electric field strength within the depleted absorbing material, and a change in optical absorption through the Franz-Keldysh effect [27]. Especially at high bias, $R(V)$ may additionally arise through the mechanism of impact ionization. A rough calculation will demonstrate the significance of impact ionization in the InGaAs region. At 8V reverse bias, the average electric field in the depleted InGaAs region with a thickness of $w = 200$ nm is approximately 130 kV/cm considering the weak doping in the semi-intrinsic InGaAs and InP layer. According to [28], the impact ionization coefficient for electrons and holes are approximately $\alpha = 420$ cm⁻¹ and $\beta = 0.2$ cm⁻¹, respectively. Adopting the theory of McIntyre [14], assuming a

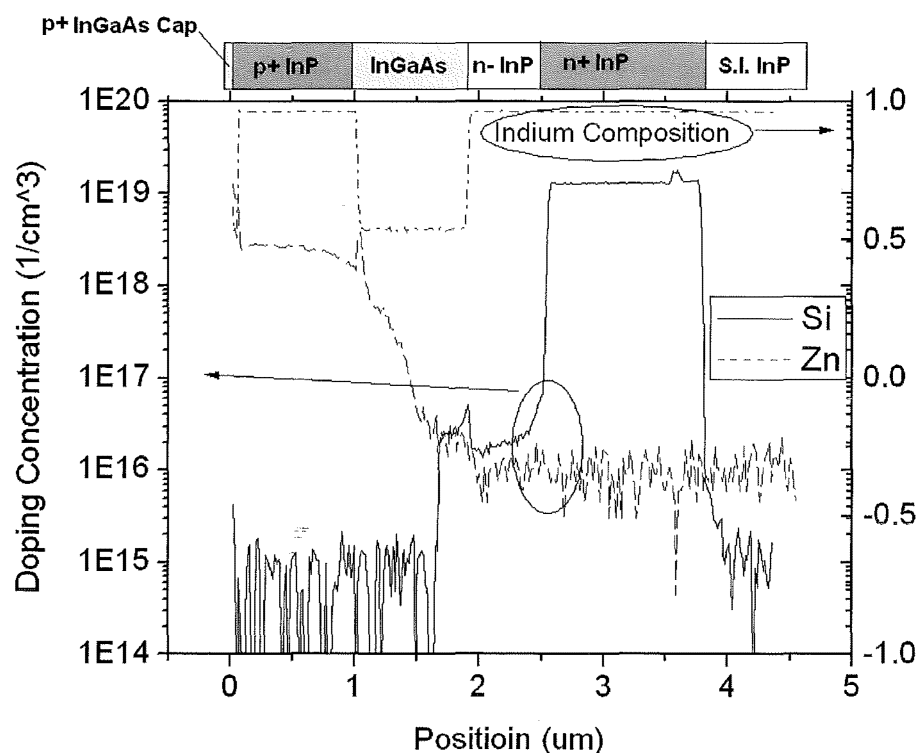


Figure 4.3 Doping profile of Zn and Si from a SIMS measurement

weak field, and performing the appropriate spatial average, the increase in responsivity due to impact ionization is $(\alpha+\beta)w/2 = 0.4\%$, which is very close to our measurement as shown in the inset of Figure 4.1.

In order to study the mechanisms of voltage- and photocurrent-dependent capacitance, a theoretical model has been developed that takes into account charge transport in the form of the continuity equations for both electrons and holes, Poisson's equation for the electrostatic potential, and coupling between the photodiode and its surrounding circuit in a lumped element model. Relevant equations are solved simultaneously as functions of applied bias and optical illumination. In order to precisely calculate the capacitance, an accurate doping profile is required. Secondary ion mass spectroscopy (SIMS) has been carried out to determine the doping profiles in the CC-MUTC device. The results are shown in Figure 4.3. Dopant profiles derived from the SIMS measurement were incorporated into our simulations, with relatively minor adjustments to achieve better agreement with the measured static $C(V)$ curve of Figure 4.2. As is shown in Figure 4.3, as a result of the diffusion of Zn, the doping concentration in the p-type InGaAs region is even lower than the intended value shown in Figure 2.3, which results in a relatively large dependence of capacitance on voltage. The simulated $C(V)$ curve is superimposed on the measured data in Figure 4.2, and a good agreement with measurement has been achieved. The voltage swing causes the device capacitance to be modulated when AC photocurrent flows through the $50\ \Omega$ load resistor, and thus causes distortion of the output signal. This will be discussed in more detail in Section 2.3.

Photocurrent-dependent capacitance arises from screening of the space charge field by photo-generated carriers within the depletion region, and often results in a negative

differential capacitance with increasing photocurrent. Electrons and holes that are photo-generated or injected into the depletion region propagate to the n- and p-side depletion region boundaries, respectively. Under conditions of high optical illumination, the total volumetric charge density within the depletion region may be reduced, as the free electron density preferentially screens the ionized donor charge and the free hole density preferentially screens the ionized acceptor charge. In the absence of feedback from the external circuit, the total junction potential remains constant, which results in deeper penetration of the depletion region into quasi-neutral material in order to satisfy Poisson's equation. The simulated $C(I)$ curve is superimposed with the measured data in Figure 4.1, which shows good agreement with the measurement.

When considering the photocurrent-dependent capacitance, the photocurrent may also reduce the junction voltage through the series resistance, resulting in a voltage-controlled capacitance which increases with DC photocurrent. It is therefore possible to observe positive differential capacitance as a function of photocurrent when the series resistance is large enough to cause significant voltage drop. However, for the CC-MUTC photodiodes studied in this work, the series resistance is very small ($< 5 \Omega$). Therefore, the space charge screening effect dominates, which results in decreasing capacitance with photocurrent. It should be noted, that for the $C(I)$ measurement the 50Ω load resistance of the network analyzer was AC-coupled by a blocking capacitor and thus did not create a DC photocurrent induced voltage drop. This may explain the qualitatively different observations reported here compared to those of [24].

4.4 The Equivalent Circuit Model in Two-Tone Setup

In order to evaluate the OIP3 theoretically, considering the nonlinear phenomena described in Section 4.2, we developed a numerical equivalent circuit model based on the analytical equivalent circuit model described in [24]. We have shown that this numerical equivalent circuit model provides excellent fits to the measured OIP3. The equivalent circuit is shown in Figure 4.4. According to this model the voltage across the photodiode $V(t)$ can be calculated from the following differential equation:

$$I(t) = \frac{d[C \cdot V(t)]}{dt} + \frac{V(t)}{R_p} + \frac{V(t)}{R_s + R_L} = \frac{dC}{dt} V + C \frac{dV(t)}{dt} + \frac{V(t)}{Z} \quad (4.1)$$

where C is the device capacitance and R_p , R_s and R_L are the parallel, series and load resistances, respectively. Z is the equivalent resistance of all the resistors. According to the two-tone setup shown in Figure 3.2 in Chapter 3, the expressions for the variables in equation (4.1) are as follows. Neglecting the transit-time effects of the carriers, the AC photocurrent $I(t)$ is given as the product of the responsivity R and the optical input power modulated at frequencies f_1 and f_2 , with an average power P and modulation depth m . Hence $I(t) = R \cdot P \cdot m \cdot (\sin(2\pi f_1 \cdot t) + \sin(2\pi f_2 \cdot t))$. In the actual simulation, the time varying photocurrent $I(t)$ and voltage $V(t)$ are calculated in a finite time duration T and time, t , is discretized with a sampling period T_s . The differential equation (4.1) is solved with an iterative algorithm. At the first time point $t = t_0$, the voltage is calculated using the equation $\frac{V(t_0)}{R_p} + \frac{V(t_0)}{R_s + R_L} = I(t_0)$. Then for $k > 0$, the differential equation (4.1) is transformed into a discrete-time difference equation, i.e.,

$$I(t_k) = \frac{C(t_k) - C(t_{k-1})}{t_k - t_{k-1}} V_{k-1} + C(t_k) \frac{dV(t_k)}{t_k - t_{k-1}} + \frac{V(t_{k-1})}{Z} \quad (4.2)$$

We calculate $dV(t_k)$ from equation (4.2), and calculate the voltage in the next time interval with equation $V(t_k) = V(t_{k-1}) + dV(t_k)$, until the voltage in all the time intervals are solved. Finally, after temporal stabilization, we compute the spectral response using a fast Fourier transform. In order to take the voltage- and photocurrent-dependent device capacitance into account, junction capacitance is generally defined as $C = C(V_L, I) = C(V_b) + \Delta C(V_L) + \Delta C(I)$ with the static capacitance $C(V_b)$ and variable capacitances $\Delta C(V_L)$ and $\Delta C(I)$. V_b is the static reverse bias provided by the voltage source and V_L is the transient voltage drop on the photodiode. Similarly the voltage-dependent responsivity is defined as $R = R_0 + \Delta R(V_L)$ with $R_0 = 0.75$ A/W. To compute the OIP3 based on the experimental data, we derived $\Delta R(V_L)$, $\Delta C(V_L)$ and $\Delta C(I)$ from numerically fitting the data shown in Figure 4.1 and Figure 4.2. Furthermore, we used $R_S = 5 \Omega$, $R_P = 1 \text{ M}\Omega$ and $R_L = 50 \Omega$, which are all obtained from measurements.

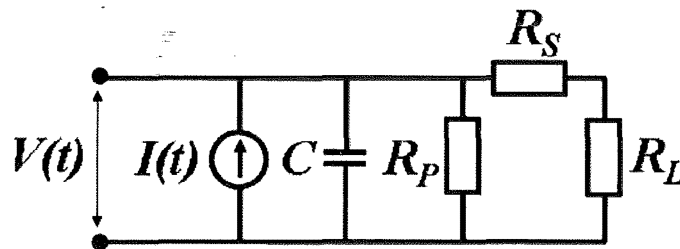


Figure 4.4 Equivalent circuit for the photodiode

The frequency dependence of OIP3 of the CC-MUTC photodiode was calculated using the equivalent circuit model and compared to the measured data. The $\Delta R(V_L)$, $\Delta C(V_L)$ and $\Delta C(I)$ were obtained using the quadratic fit, exponential fit and quadratic fit to the corresponding measurement data shown in Figure 4.1 and Figure 4.2 in order to obtain the best fit [From this it is not clear what data was fit by quadratic fit and what used an exponential fit.]. The dotted and dashed lines in Figure 4.5 show the calculated characteristics of the OIP3 exclusively due to the voltage-dependent responsivity $R(V_L)$ and capacitive effects $C(V_L, I)$, respectively. Since $R(V)$ is a static nonlinear mechanism, the OIP3 limited by $R(V)$ is constant with frequency, while $C(V)$ and $C(I)$ are dynamic nonlinear mechanisms and thus the OIP3 limited by both $C(V)$ and $C(I)$ decreases with frequency. At low frequencies, the $R(V)$ limited OIP3 agrees well with the measurement while at high frequencies, the $C(V)$ and $C(I)$ limited OIP3 become dominant and shows

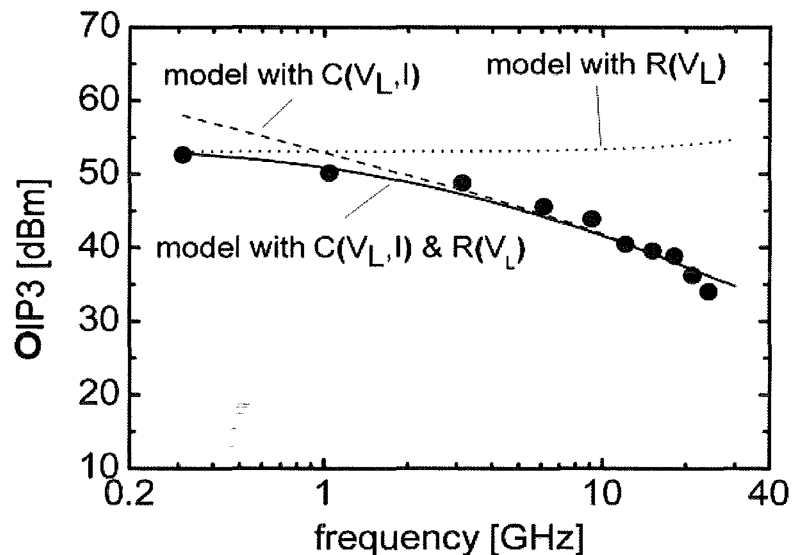


Figure 4.5 Measured OIP3 (circles) at 50 mA and reverse bias $V_b = -7$ V, and calculated OIP3 based on the voltage-dependent responsivity (dotted line), capacitive effects (dashed line) and all effects (solid line)

good agreement with the measured data. Only when these effects are considered together (solid line in Figure 4.5) do we find a good agreement with the experimental data over the entire frequency range.

4.5 Optimization of Photodiode Linearity Using the Equivalent Circuit Model

The equivalent circuit model can provide theoretical guidance to optimize the linearity of photodiodes. In this section, the equivalent circuit model is first used to help find the optimal wavelength for the highest OIP3 of the CC-MUTC photodiodes. The wavelength dependence of the R(V) curve was measured with a tunable external cavity laser covering the C-band, L-band, and O-band. For each wavelength the optical input power was set to a constant value providing a photocurrent of 50 μA at -2 V. Hence, the photocurrent-voltage characteristics can be directly translated into an R(V) curve. For a better comparison the data was normalized to the responsivity at -2 V. Each data point

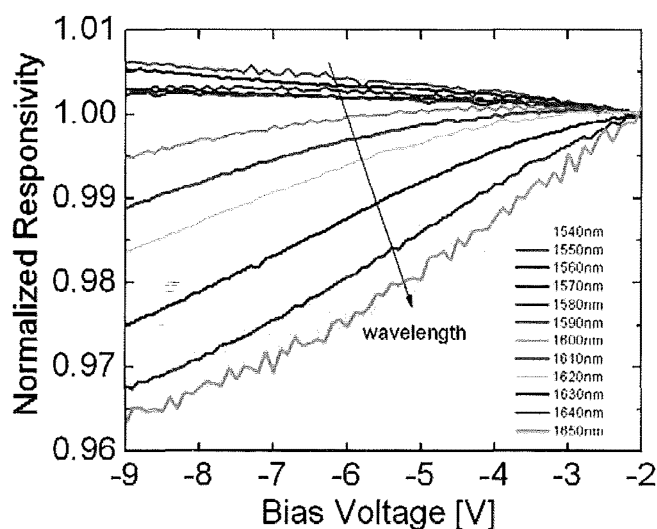


Figure 4.6 Relative responsivity measured at 50 μA photocurrent. The wavelength was changed from 1540 nm to 1650 nm in 10 nm steps.

was normalized separately by measuring the reference photocurrent at -2 V immediately after each data point was determined. Thus, potential slow drifts (>1 s) of the fiber-chip coupling which also may lead to a change in the photocurrent during the measurement were effectively eliminated.

Figure 4.6 shows the measured normalized responsivity versus applied reverse voltage. At 1540 nm an increase in responsivity of 0.6 % can be observed between -2 V and -9 V. This value is in good agreement with our previous result, which was obtained using a pulsed laser source, as shown in the inset of Figure 4.1. Tuning the input signal to longer wavelengths leads increasingly to a reduction in relative responsivity at higher voltages. We recorded the strongest voltage-dependence at 1650 nm, where the relative responsivity was 96.5% at -9 V. However, near 1590 nm, the characteristics are almost flat as evidenced by a maximum change of only 0.2 %. Figure 4.7 shows the normalized responsivity versus bias at wavelengths between 1250 nm and 1350 nm. In this range, we

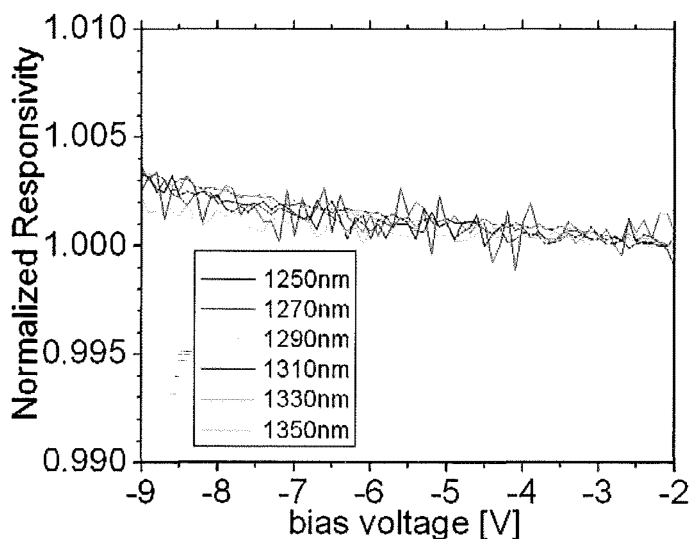


Figure 4.7 Relative responsivity measured at $50\mu\text{A}$ photocurrent. The wavelength was changed from 1250 nm to 1350 nm in 20 nm-steps.

find a relative increase in responsivity of 0.3 % which is independent of the incident wavelength.

The above behavior can be explained as follows. Since a change of the bias voltage leads directly to a variation in the electric field strength within the depleted absorbing material, the optical absorption coefficient α is also changed through the Franz-Keldysh effect. According to [29], a larger change in α , and thus in the measured photocurrent, can be expected at wavelengths close to the InGaAs band gap, which corresponds to a wavelength ~ 1650 nm, which is in good agreement with our measurements. In contrast, for wavelengths far below the band gap, the Franz-Keldysh effect is less pronounced. We believe that especially at high bias, a second voltage-dependent effect may additionally arise through the mechanism of impact ionization. A rough calculation will demonstrate the significance of impact ionization in the InGaAs region. At 8V reverse bias, the average electric field in the n⁻ InGaAs region with a thickness of $w = 200$ nm is approximately 130 kV/cm considering the weak doping in the InGaAs and InP layer. According to [28], the impact ionization coefficient for electrons and holes are approximately $\alpha = 420$ cm⁻¹ and $\beta = 0.2$ cm⁻¹, respectively. Adopting McIntyre's local field model, [30] taking the weak field limit, and performing the appropriate spatial average, the increase in responsivity due to impact ionization would be $(\alpha+\beta)w/2 = 0.4\%$, which is very close to our measurement at shorter wavelengths around 1300 nm.

| Bias voltage | OIP3 at 1270 nm | OIP3 at 1591.5 nm | OIP3 at 1610 nm |
|--------------|-----------------|-------------------|-----------------|
| -4.5 V | 55 dBm | 61 dBm | 48 dBm |
| -7 V | 50 dBm | 46 dBm | 45 dBm |

Table 4-1 calculated OIP3 limited by $R(V)$.

Based on these results we estimated the OIP3 caused by the $R(V)$ at different input wavelengths using the equivalent circuit model together with the exponential fit functions shown in Figure 4.8. The change of bias voltage is calculated from the photo-current-induced transient voltage drop at the series and load resistors. The results in Table 4-1 indicate that smaller relative changes in responsivity generally lead to higher OIP3. We calculated the highest OIP3 of 61 dBm at a wavelength of 1591.5 nm and -4.5 V since those conditions yield relatively flat $R(V)$ characteristics. Compared to the OIP3 at

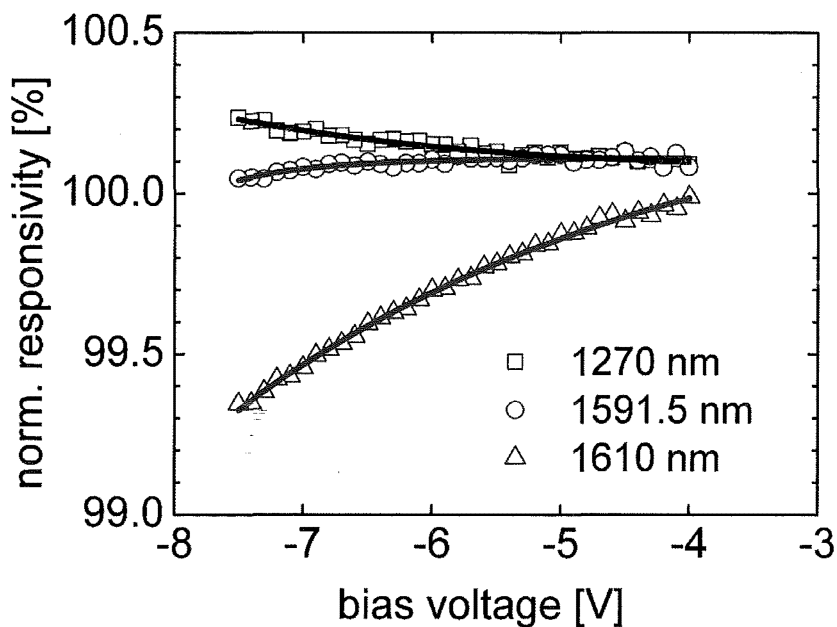


Figure 4.8 exponential fits to the measured voltage-dependent responsivity

1610 nm this value is 13 dB higher.

The OIP3 of a 40- μm -diameter CC-MUTC photodiode were measured at 152 MHz and 50 mA for various reverse biases and wavelengths, and the results are shown in Figure 4.9. The reason the measurements were carried out at such a low frequency of 152 MHz was due to the fact that the simulated OIP3 only considered $R(V)$, which is dominant only at low frequencies where $C(V)$ and $C(I)$ are insignificant. As shown in Figure 4.9, the peak of OIP3 appears at the wavelength of 1595 nm and reverse bias of 5.5 V. This agrees reasonably well considering the accuracy of the measured $R(V)$ curves and the accuracy of the exponential fit.

4.6 The Equivalent Circuit Model in Bias Modulation Setup

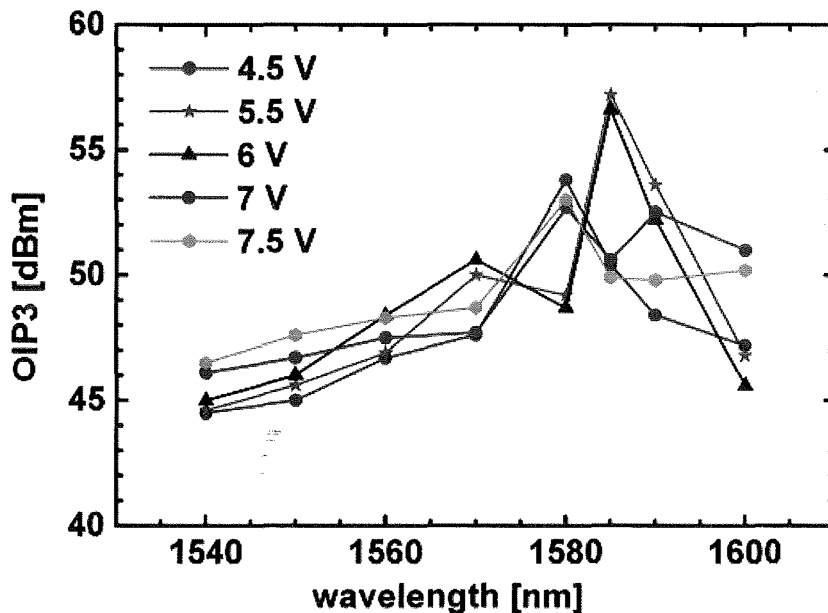


Figure 4.9 Measured OIP3 of a 40- μm -diameter CC-MUTC photodiode at 152 MHz and 50 mA on for different wavelengths

As discussed in Section 4.4 voltage-dependent or photocurrent-dependent phenomena can give rise to IMD3. In two-tone or three tone measurements, the measured

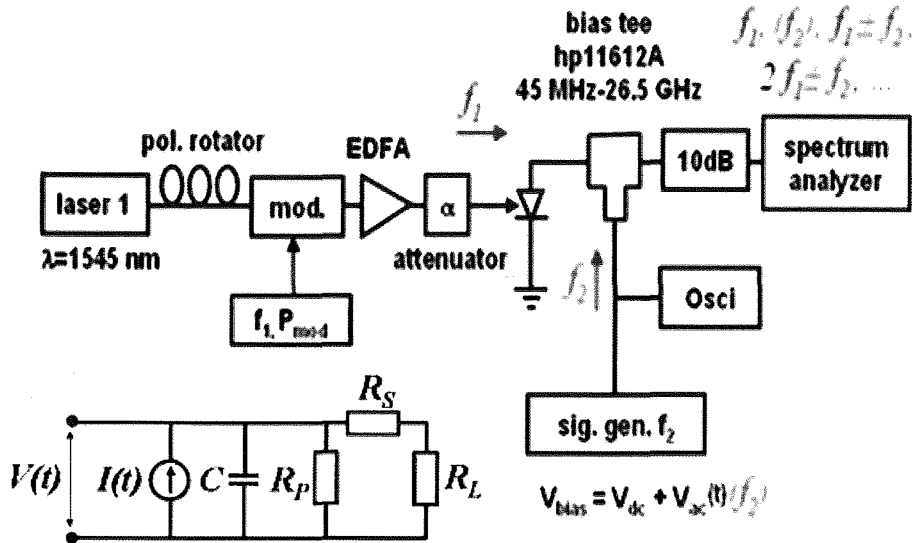


Figure 4.10 Experimental setup bias modulation measurements.

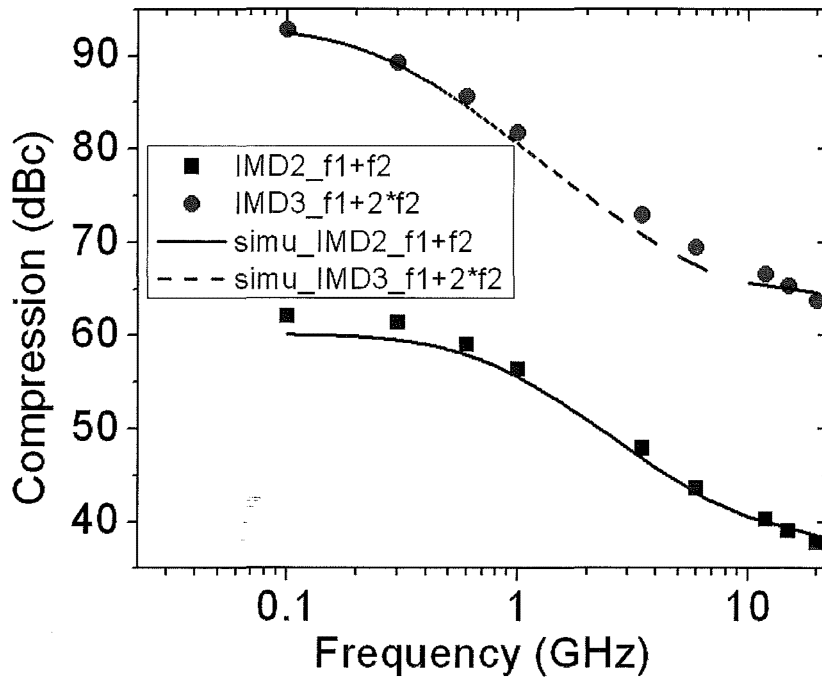


Figure 4.11 Measured and simulated IMD2 and IMD3 vs. fundamental frequency f_1 at $I_{pd} = 10 \text{ mA}$, $V_{dc} = 6 \text{ V}$ using the numerical model

intermodulation distortions are produced by both the voltage-dependent and photocurrent-dependent nonlinear mechanisms. In this case it is difficult to identify the individual contributions to the intermodulation distortions. As described in Chapter 3, bias modulation measurement is an effective way to study the effect of voltage-dependent nonlinearity without the influence of photocurrent-dependent nonlinearity. In the bias modulation setup, the same differential equation (4.1) is applicable:

The bias modulation setup is shown again together with the equivalent circuit model in Figure 4.10. Neglecting the transit-time effects of the carriers, the AC photocurrent $I(t)$ is given as the product of the responsivity R and the optical input power modulated at the frequency f_1 with an average power P and modulation depth m . Therefore, $I(t) = R \cdot P \cdot m \cdot \sin(2\pi f_1 t)$. The AC voltage signal $V_{ac}(t)$ is provided by the signal generator so that $V_{ac}(t) = V_0 \cdot \sin(2\pi f_2 t)$, where the frequency $f_2 = 20$ kHz is fixed for all the bias modulation measurements. In order to take the voltage-dependent capacitance $C(V)$ into account, the junction capacitance C is generally defined as $C(V) = C(V_{dc} + \Delta V)$, where V_{dc} is the static reverse bias provided by the voltage source and $\Delta V = V_{ac}(t) - R \cdot P \cdot R_S - V(t)$ is the difference between the transient voltage on the photodiode and the average voltage V_{dc} . Similarly the voltage-dependent responsivity is defined as $R(V) = R_0(V_{dc} + \Delta V)$. To compute the intermodulation products more accurately based on the experimental data $C(V)$ and $R(V)$ are expressed by the fit functions shown in Figure 4.1. For the $C(V)$ curve we employed an exponential fit, and for the $R(V)$ curve we employed a quadratic fit. Defining compression as the ratio of fundamental power to intermodulation product power measured in dBc, the compression of IMD2 at $f_1 + f_2$ and the compression of IMD3 at $f_1 + 2f_2$ can be expressed as:

$$Comp_{IMD2} = 10 \log_{10} \left(\frac{P_{f1}}{P_{IMD2}} \right), Comp_{IMD3} = 10 \log_{10} \left(\frac{P_{f1}}{P_{IMD3}} \right) \quad (4.3)$$

The IMD2 compressions and IMD3 compressions are plotted versus the fundamental frequency f_1 for a 56 μm -diameter CC-MUTC photodiode at 10 mA photocurrent and DC reverse bias of $V_{dc} = 6$ V. The results are summarized in Figure 4.11. The IMD2 compression is relatively constant in the low frequency range and decays with frequency in the higher frequency range. This behavior can be explained by the combined effects of $R(V)$ and $C(V)$. In the low frequency range, where the frequency independent term of nonlinear responsivity dominates, the IMD2 compression shows relatively flat frequency response. At higher frequencies the nonlinear capacitance begins to dominate and the IMD2 compression rolls off with frequency. The compressions of IMD2 and IMD3 have been calculated with the equivalent circuit model using the approach described in Section 4.4. The equation was solved by an iterative algorithm and after temporal stabilization, the spectral response was computed using a fast Fourier transform. In Figure 4.11 the solid and dashed lines show the IMD2 compression and IMD3 compression calculated from the $R(V)$ and $C(V)$ curve. We found good agreement between the simulation and the experimental data over the entire frequency range. Based on the experimental and simulation results, we conclude that the voltage-dependent nonlinearities, namely $R(V)$ and $C(V)$, are important nonlinear mechanisms that contribute to the intermodulations of photodiodes, and thus must be minimized in order to improve the photodiode linearity.

4.7 Conclusion

In this chapter the nonlinear phenomena in CC-MUTC photodiodes are quantitatively investigated. The responsivity exhibits a voltage dependence, but no significant

dependence on photocurrent. The junction capacitance of CC-MUTC photodiodes decreases with both reverse bias and photocurrent. Based on experimental data a numerical equivalent circuit model has been developed. It has shown that the frequency characteristics of the OIP3 can be attributed to the change of both the responsivity and device capacitance induced by the photocurrent and the transient voltage drop across the load and series resistors. Further investigation of the nonlinear phenomena suggests that the Franz-Keldysh effect and impact ionization are the primary reasons for the voltage-dependent responsivity $R(V)$, while low doping concentration in the p-type InGaAs absorber and space charge screening are responsible for the voltage-dependent capacitance and photocurrent-dependent capacitance $C(I)$, respectively. An equivalent circuit model was used to find the wavelength that yielded the highest OIP3 at low frequencies. The CC-MUTC achieved an OIP3 of 57.5 dBm at 152 MHz with an operating wavelength of 1595 nm. Bias modulation measurements were also carried out to verify the relative importance of the voltage-dependent nonlinear mechanisms. Based on experimental results, the equivalent circuit analysis shows that the frequency characteristics of the intermodulation distortions can be attributed to the change of both the responsivity and device capacitance induced by the modulated bias. All the measurement results and analysis prove that voltage-dependent responsivity $R(V)$, voltage-dependent capacitance $C(V)$ and photocurrent-dependent capacitance $C(I)$ are the major nonlinear mechanisms in CC-MUTC photodiodes and need to be minimized to improve the photodiode linearity.

Chapter 5 Novel Designs for High Linearity Photodiodes

5.1 Introduction

In Chapter 4 nonlinear mechanisms in CC-MUTC photodiodes are quantitatively studied. Voltage-dependent responsivity $R(V)$ has been found to be the dominant nonlinear mechanism at low frequencies, while voltage-dependent capacitance $C(V)$ and photocurrent-dependent capacitance $C(I)$ are the dominant nonlinear mechanisms in high frequencies. By tuning the operating conditions such as wavelength, reverse bias and photocurrent, $R(V)$ can be minimized and OIP3 as high as 57.5 dBm has been achieved at a low frequency of 152 MHz for CC-MUTC. Other types of photodiodes also achieved good OIP3 at low frequencies. A dual depletion region (DDR) photodiode has been reported to have a third-order harmonic output intercept point (HOIP3) of 54 dBm at 829 MHz [31] and a partially depleted absorber (PDA) photodiode has achieved an HOIP3 of 51 dBm at 3 GHz [32], which is equivalent to third-order output intercept points (OIP3) of 49.2 dBm and 46.2 dBm, respectively, as estimated from the cubic dependence of the third-order nonlinearity terms [8]. However, the OIP3 of previously reported photodiodes exhibited significant roll-off with frequency and thus high OIP3 is difficult to obtain at high frequencies [24]. The CC-MUTC photodiode studied in Chapter 4 reached an OIP3 of 36 dBm at 20 GHz. An OIP3 value of 35 dBm at 20 GHz was reported for a uni-traveling-carrier (UTC) photodiode [33].

In this chapter, first an InGaAs/InP partially depleted absorber (PDA) photodiode using high doping levels for both p-type and n-type absorbers is introduced. This type of photodiode will be referred to as an HD-PDA in this dissertation. The absorbers of the

HD-PDA are highly doped in order to minimize the dependence of capacitance on reverse bias and photocurrent, and thus to improve the OIP3 at high frequencies. Measurement results show that the OIP3 of the HD-PDA does not roll off with frequency. The OIP3 of the HD-PDA is 36 dBm at low frequencies and remains as high as 39 dBm up to 20 GHz.

HD-PDA photodiodes have low OIP3 at low frequencies since they have a thick depleted InGaAs absorber, which leads to stronger dependence of responsivity on reverse bias. In order to achieve high OIP3 in the entire frequency range, a modified uni-traveling-carrier photodiode with highly doped p-type absorber, which will be referred to as an HD-MUTC in this chapter, is introduced. Its OIP3 is 55 dBm at low frequency and remains as high as 47.5 dBm at 20 GHz.

5.2 Partially Depleted Absorber Photodiodes with Highly Doped Absorber

5.2.1 Device Design

| |
|---|
| InGaAs, p ⁺ , C, 2.0×10^{19} , 50nm |
| InP, p ⁺ , Be, 2×10^{19} , 1000nm |
| InGaAs, p ⁺ , C, 3×10^{19} , 100nm |
| InGaAs, u.i.d., $< 2.0 \times 10^{16}$, 800nm |
| InGaAs, n ⁺ , Si, 3×10^{19} , 30nm |
| InP, n ⁺ , Si, 3.0×10^{19} , 1000nm |
| InP, semi-insulating substrate, Double side polished |

Figure 5.1 Schematic layer structures of HD-PDA photodiode. All doping concentrations in cm^{-3}

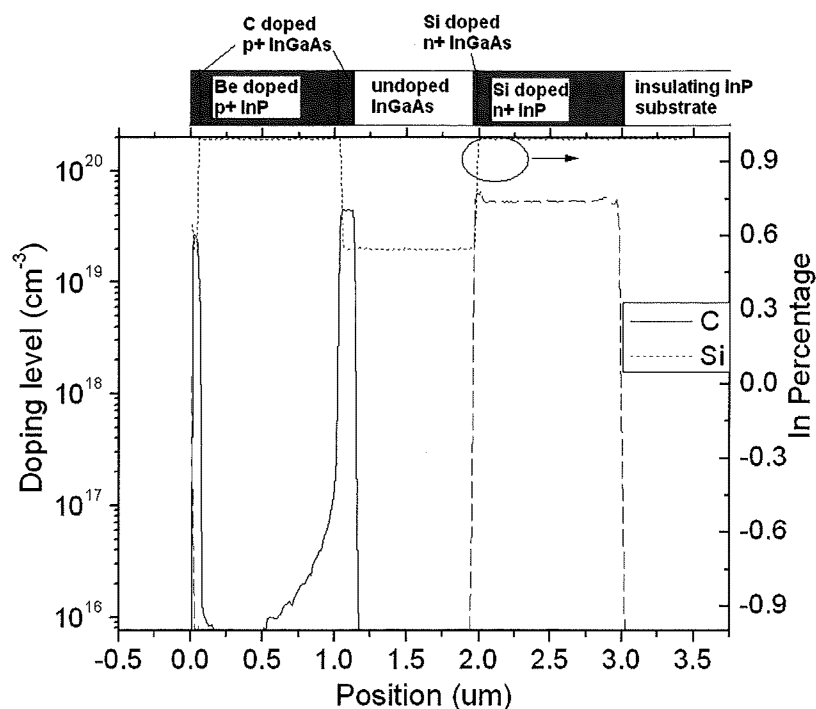


Figure 5.2 Doping profile of the HD-PDA photodiode measured with SIMS

The vertical layer design corresponds to an HD-PDA photodiode with both highly-doped undepleted absorber and low-background-doping depleted absorber as shown in Figure 5.1. The device under test was a back-illuminated InGaAs/InP mesa photodiode. The InGaAs absorbing region with a thickness of 930 nm is comprised of a 100 nm p^+ absorbing layer, an 800 nm unintentionally-doped absorber layer, and a 30 nm n^+ absorbing layer. The doping profile of the PDA-PD was measured with Secondary ion mass spectroscopy (SIMS). As shown in Figure 5.2, the doping levels in the n-type and p-type absorbing layers are as high as $3 \times 10^{19} \text{ cm}^{-3}$. Since carbon was used as the p-type dopant instead of Zn, the doping profile is very abrupt. The background doping level in the depleted absorbing layer was $< 2 \cdot 10^{15} \text{ cm}^{-3}$. The high doping levels in the n-type and p-typed absorbing layers and their abrupt doping profiles were designed to improve the

OIP3 by reducing the voltage dependence of the capacitance. The studied photodiode with an active diameter of 28 μm exhibited a 3 dB bandwidth of 23 GHz at -8 V.

5.2.2 Nonlinear Phenomena And Equivalent Circuit Analysis

It has been shown in Chapter 4 that the voltage dependent responsivity $R(V)$ is the limiting nonlinear factor for the OIP3 of photodiodes at low frequencies (< 1 GHz), while the voltage and photocurrent dependent capacitance is the limiting nonlinear factor at high frequencies. In order to improve the linearity of photodiodes in the high frequency range and reduce the frequency dependence of the OIP3, the HD-PDA photodiode with highly doped undepleted absorbers described above was designed to reduce the capacitance variation with bias voltage. The voltage-dependent capacitance $C(V)$ and voltage

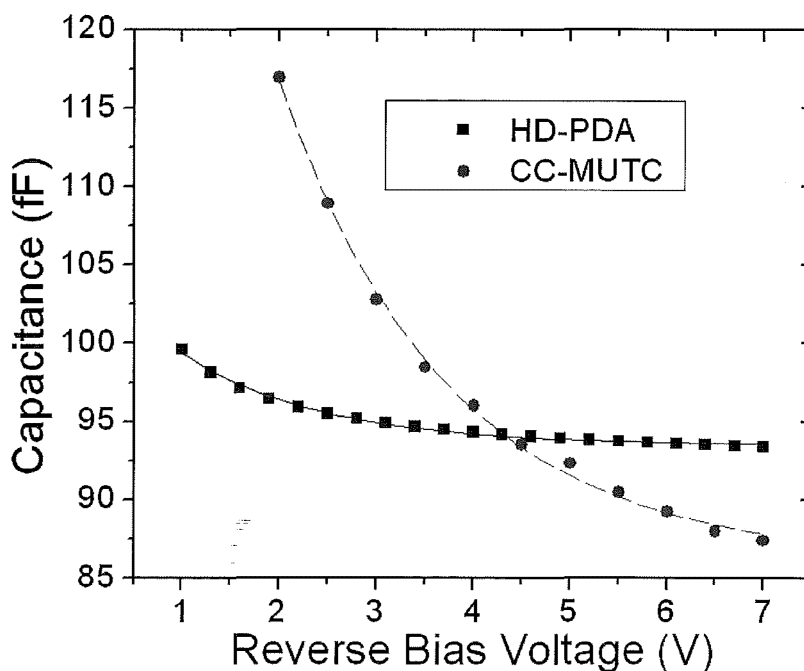


Figure 5.3 Measured photodiode capacitance (symbols) and exponential fit (lines) for CC-MUTC photodiode and HD-PDA photodiode. Inset: Relative responsivity (dots) with quadratic polynomial fit (lines) for MUTC-PD and PDA-PD.

dependent responsivity $R(V)$ of the HD-PDA photodiode were measured as described in Chapter 4 and compared with the CC-MUTC photodiode, as shown in Figure 5.3 and Figure 5.4. Both the HD-PDA and the CC-MUTC have active diameters of $28\ \mu\text{m}$. The HD-PDA photodiode has a differential capacitance of only $-0.2\ \text{fF/V}$ as a result of its highly-doped undepleted absorbers compared with $-4\ \text{fF/V}$ for the CC-MUTC photodiode. The responsivity of the PDA-PD shows a much stronger dependence on voltage (approximately 11% increase over a bias range of 8 V) compared to that of the MUTC-PD (approximately 0.5% increase over 8 V) owing to its four-times thicker depleted InGaAs layers, which exhibit impact ionization and the Franz-Keldysh effect

The frequency dependence of the OIP3 of the HD-PDA photodiode was measured

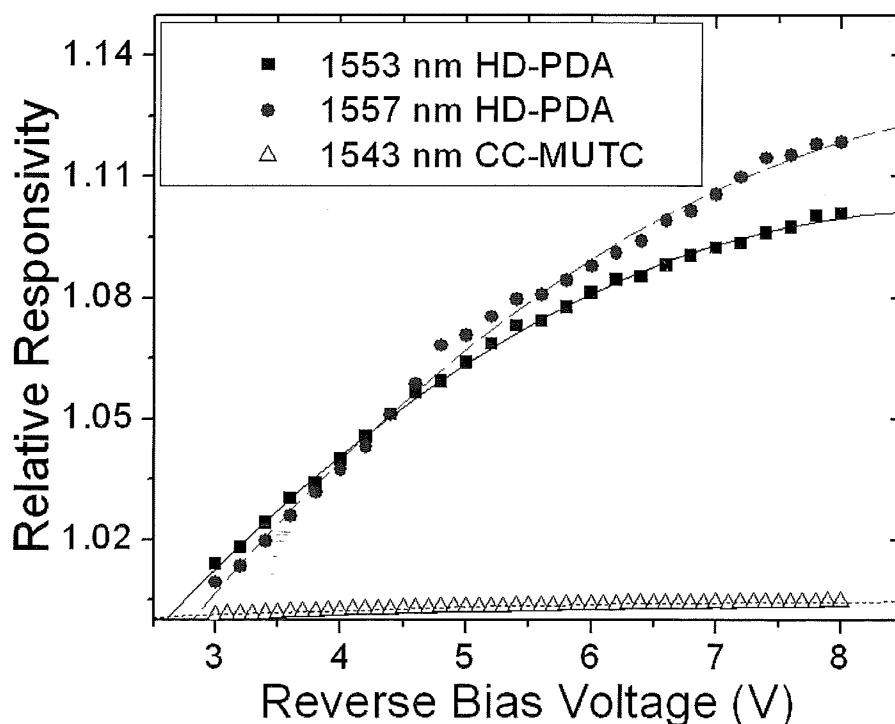


Figure 5.4 Relative responsivity (dots) with quadratic polynomial fit (lines) for CC-MUTC photodiode and HD-PDA photodiode.

using the two-tone setup described in Chapter 3 and compared to that of the CC-MUTC photodiode, as shown in Figure 5.5. The OIP3 of CC-MUTC rolls off as much as 16 dB as the frequency increases from 300 MHz to 21 GHz. In contrast, the OIP3 of the HD-PDA increases slightly with frequency up to 20 GHz, and a high OIP3 of 39 dBm is achieved at 20 GHz.

The OIP3 due to the voltage-dependent responsivity $R(V)$ of the HD-PDA (solid line in Figure 5.5) is calculated based on the equivalent circuit model described in Chapter 4. The results agree well with the frequency behavior of the OIP3 of the HD-PDA. The OIP3 due to voltage dependent capacitance $C(V)$ of the PDA-PD is also shown as the dotted line in Figure 5.5, which is as high as 52 dBm at 20 GHz. This indicates that $C(V)$ is no longer a limiting factor for the OIP3 of this HD-PDA photodiode in the frequency range up to 20 GHz. The OIP3 of the HD-PDA photodiode is expected to exceed that of

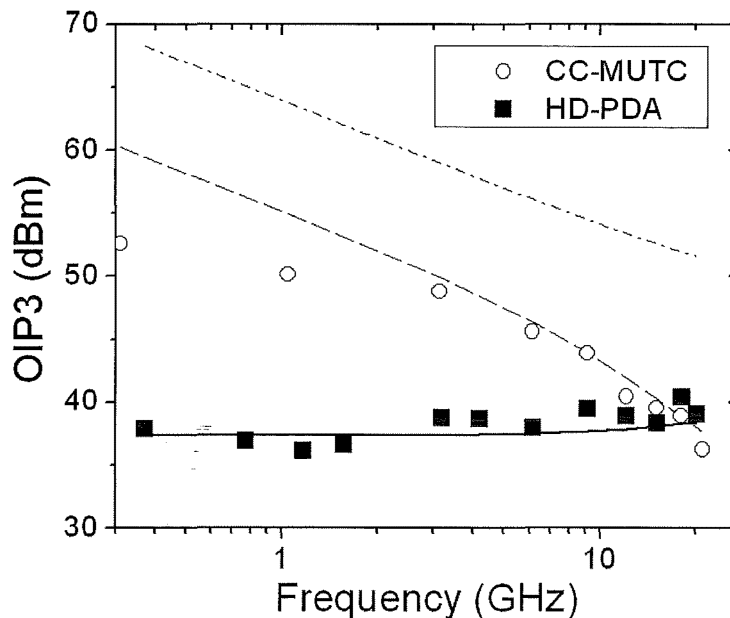


Figure 5.5 Measured OIP3 of CC-MUTC photodiode at 50 mA and $V_b = -7$ V and that of HD-PDA photodiode at 21 mA and $V_b = -8$ V.

the CC-MUTC even more significantly at higher frequencies. However, our measurement capability is limited to 20 GHz by the bandwidth of our Mach-Zehnder modulators.

5.3 Modified Uni-Traveling-Carrier Photodiodes with Highly Doped Absorber

5.3.1 . Device Design

As discussed in Section 4.2, the HD-PDA photodiode shows reduced frequency dependence of OIP3 due to its highly doped absorbers. However, since a thick depleted InGaAs layer is used, its responsivity shows relatively large dependence on reverse bias and thus the OIP3 is not high in the low frequency range. In order to improve the OIP3 in the entire frequency range, an InGaAs/InP MUTC photodiode with a highly doped p-type absorber is presented in this section. It will be referred to in the following as an HD-MUTC photodiode. The vertical layer structure of the HD-MUTC photodiode is shown in

| |
|---|
| InGaAs, p+, C, 2.0×10^{19} , 50nm |
| InP, p+, Be, 8×10^{18} , 100nm |
| InGaAs, C, 8×10^{19} - 5×10^{18} , 650 nm |
| InGaAs, n.i.d, $< 5.0 \times 10^{15}$, 300nm |
| InGaAs/InAlAs chirped Superlattice, n.i.d, $< 5.0 \times 10^{15}$, 24nm |
| InP, Si, 5×10^{16} , 5nm |
| InP, n.i.d, $< 5.0 \times 10^{15}$, 400nm |
| InP, n+, Si, 3.0×10^{19} , 1000nm |
| InP, semi-insulating substrate, Double side polished |

Figure 5.6 Schematic cross section of InGaAs–InP HD-MUTC photodiode.

Figure 5.6. The epitaxial layers were grown on a semi-insulating InP substrate by molecular beam epitaxy. The InGaAs absorbing region with a thickness of 950 nm is comprised of a 650 nm p^+ absorbing region and a 300 nm unintentionally-doped absorber layer. Previously p-type InGaAs absorbing layers doped with Zn exhibited strong diffusion of the Zn dopant, which results in a non-abrupt junction doping profile, as the case in CC-MUTC. This non-abrupt doping profile causes the junction capacitance of the photodiode to have a strong dependence on bias voltage, which has been shown to be responsible for the decrease of OIP3 with frequency. In order to form an abrupt junction doping profile, C was used instead of Zn as the dopant in the 650 nm p^+ absorbing layer. The p-type doping level was graded in 10 steps from $8 \cdot 10^{19}$ to $5 \cdot 10^{18} \text{ cm}^{-3}$ so as to assist electron transport in the doped absorber. A 24 nm-thick InGaAs/InAlAs chirped superlattice and a 5 nm moderately n-type doped InP cliff layer were incorporated between the InGaAs and InP to reduce carrier pile up at the heterojunction interface. The 24 nm-thick InGaAs/InAlAs chirped superlattice is used to smooth the bandgap discontinuity between the InGaAs layer and the InP layer [34], while the 5 nm moderately n-type doped InP cliff layer is used to enhance the electric field in the intrinsic InGaAs layer to help electrons inject into the intrinsic InP layer and reduce the space charge effect in the intrinsic InGaAs layer, as discussed in Chapter 2. The background doping level in the unintentionally-doped absorbing layer was below $5 \cdot 10^{15} \text{ cm}^{-3}$. Back-illuminated mesa structures were fabricated by inductive coupled plasma reactive ion etching. Microwave contact pads and an air-bridge connection to the top p-contact layer were fabricated for high-speed measurements. Finally a 220 nm SiO_2 anti-reflection layer was deposited on the back of the wafer. The devices were mounted on an Al heat sink for testing. Photodi-

odes with an active diameter of 40 μm exhibited a 3 dB bandwidth of 13 GHz at -6 V and responsivity of 0.49 A/W at 1550 nm.

Compared with a CC-MUTC photodiode that has similar thickness of InGaAs absorber, the responsivity of the HD-MUTC is not as high. This is due to the fact that the p-type InGaAs absorber is so highly doped that the electron lifetime in the p-type InGaAs absorber of the HD-MUTC is much shorter than that of the CC-MUTC and thus a fraction of the photo-generated electrons recombine in the highly doped p-type InGaAs absorber of the HD-MUTC before they diffuse into the intrinsic InGaAs layer.

5.3.2 Measurement of Nonlinear Phenomena

The $R(V)$ and $C(V)$ of the HD-MUTC photodiodes were measured and are com-

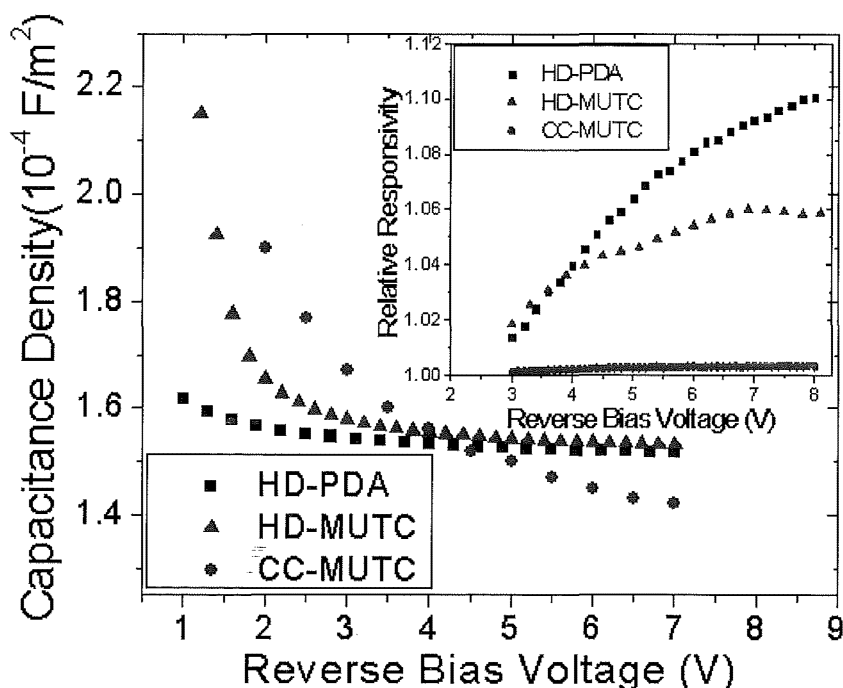


Figure 5.7 Measured junction capacitance density for CC-MUTC photodiode, HD-PDA photodiode, and HD-MUTC photodiode. Inset: Relative responsivity for CC-MUTC, HD-PDA and HD-MUTC photodiodes.

pared with those of the CC-MUTC photodiode and the HD-PDA in Figure 5.7. $R(V)$ is normalized relative to the responsivity at 2 V reverse bias and $C(V)$ is expressed in terms of the capacitance density, which is independent of the photodiode diameter. As a result of the high carbon doping level in the undepleted absorbers, the capacitance density of the HD-MUTC photodiodes has a significantly weaker voltage dependence than the CC-MUTC photodiodes when the bias is $> 4V$. However, it is similar to that of the HD-PDA photodiodes. Also the capacitance of the CC-MUTC photodiode was reported to decrease with photocurrent. However, no dependence on photocurrent has been observed for the HD-MUTC photodiode, which is similar to that of HD-PDA due to the highly doped absorbers. The responsivity of the HD-MUTC photodiodes shows a stronger dependence on voltage ($\sim 6\%$ increase over 8 V) than that of the CC-MUTC photodiodes ($\sim 0.5\%$ increase over 8 V), but a weaker dependence than the HD-PDA photodiodes ($\sim 10\%$ increase over 8 V). This is due to the fact that impact ionization and the Franz-Keldysh effect are significant in the depleted InGaAs layers. The thicker the depleted InGaAs layer, the greater is the influence of these effects. The depleted InGaAs layer in the HD-MUTC photodiodes (300 nm) is thicker than that in the CC-MUTC photodiodes (designed to be 200 nm but actually ~ 100 nm due to Zn diffusion), but thinner than that in the HD-PDA photodiodes (800 nm).

5.3.3 Measurement of OIP3

As discussed previously, $R(V)$ is the primary limiting factor of the OIP3 at frequencies < 3 GHz. Based on the equivalent circuit model described in Chapter 4 and using a quadratic fit to the measured voltage-dependent responsivity $R(V)$ of the HD-MUTC photodiodes, the calculated low-frequency OIP3 is 38.3 dBm. The dashed line in Figure 5.8 is the calculated OIP3 under the assumption that $R(V)$ is independent of the photocurrent. Figure 5.8 shows the measured OIP3 of the HD-MUTC versus photocurrent at 320 MHz using the three-tone measurement setup discussed in Chapter 3. The wavelengths of the lasers in the three-tone setup were 1544 nm, 1545 nm and 1546 nm and the lasers were modulated at 300.7 MHz, 311.1 MHz and 320.7 MHz, respectively. The OIP3 exhibits a current-dependent component and reaches peaks at slightly different photocurrents for different biases. To verify the highest measured OIP3 of 55 dBm, at 33 mA photocurrent and 10 V reverse bias, the drive power of the optical modulator is varied in

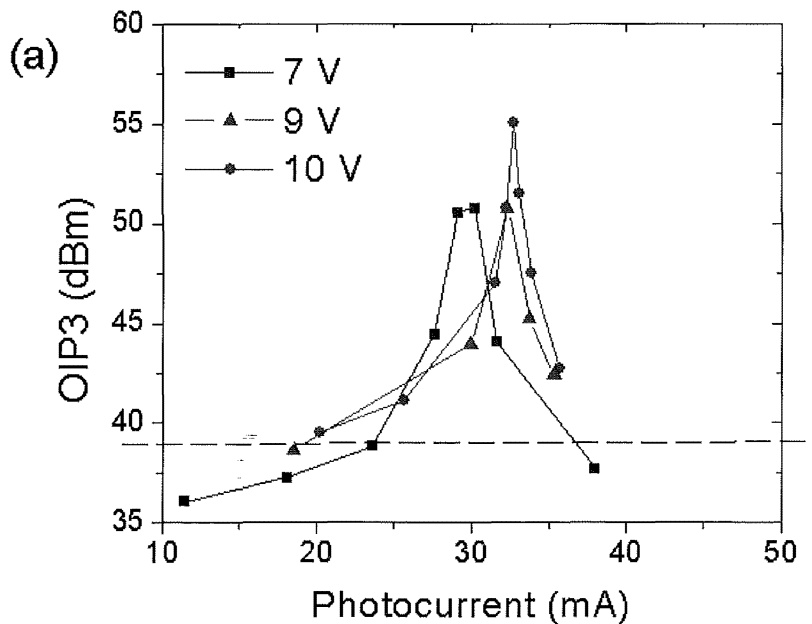


Figure 5.8 OIP3 of the HD-MUTC photodiode versus photocurrent at 7 V, 9 V and 10 V reverse bias.

order to determine the dependence of P_{IMD3} on P_f . As shown in Figure 5.9, P_f and P_{IMD3} are well characterized by a slopes of 1 and 3, respectively. The measured OIP3 value of 55 dBm is the extrapolated intercept of the P_f and P_{IMD3} plots.

The photocurrent dependence of OIP3 suggests that $R(V)$ is influenced by the photocurrent level. Since both impact ionization and the Franz-Keldysh effect are temperature dependent [35, 36], the shape of the $R(V)$ curve may change as the photocurrent increases due to the increase of the device temperature. The $R(V)$ curves shown in the inset of Figure 5.7 were measured at very low photocurrent levels ($< 200 \mu\text{A}$). Although, in theory, the $R(V)$ curves at high photocurrent levels can be measured in the same way, in practice we found that the responsivity shows much stronger dependence on reverse bias compared with those measured at low photocurrent levels. As a result, low OIP3 would

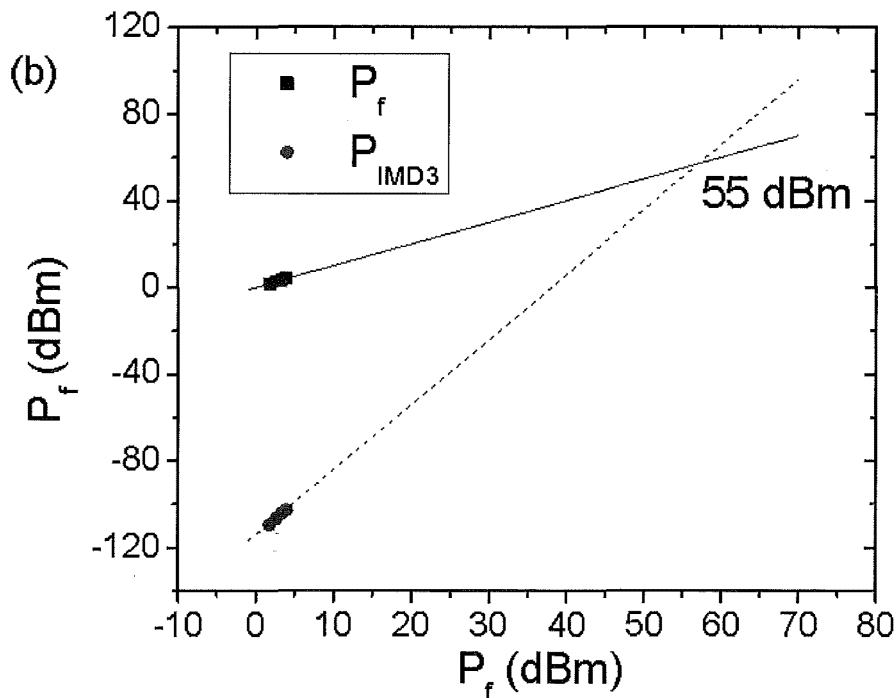


Figure 5.9 The power of IMD3 versus fundamental power shows a good slope of 3 and an extracted OIP3 of 55 dBm at 33 mA and 10 V

be expected from the high photocurrent $R(V)$, which is inconsistent with the OIP3 peaks observed in Figure 5.8. The DC measurements of the $R(V)$ curve at high photocurrents involves not only the dependence of responsivity on reverse bias but also the dependence of responsivity on temperature. The temperature change due to ohmic heating is a slow process. For the HD-MUTC photodiode studied in this paper we observed that the stabilization time for the DC photocurrent increases monotonically with photocurrent and when the photocurrent is larger than 20 mA the stabilization time could be up to several seconds. This likely due to some slow feed back process in which the increasing temperature changes the absorbing coefficient of the InGaAs by influencing the temperature-dependent Franz-Keldysh effect and impact ionization, and thus changes the photocurrent, which in return changes the temperature. However the measurements of OIP3 are carried out at high frequencies and thus the transient current change will not induce a significant temperature effect. It follows that, only the dependence of responsivity on reverse bias is significant. For these reasons DC measurements of $R(V)$ curves at high photocurrents can not accurately predict the OIP3. We have used an alternative OIP3 measurement technique, bias modulation, to determine the impact of high operating current on $R(V)$. More details will be discussed in Section 5.3.4.

The frequency dependence of the OIP3 of the HD-MUTC photodiode was measured using the three-tone technique at different photocurrent levels; the results are shown in Figure 5.10. At 33 mA and 10 V reverse bias, where the OIP3 of the HD-MUTC photodiode exhibits a peak at low frequencies, the OIP3 is 55 dBm and decreases only slightly with increasing frequency. At 20 GHz it remains as high as 47.5 dBm. The solid line in Figure 5.10 is the calculated frequency dependence of the OIP3 at 10 V reverse bias based on the measured $C(V)$ curve. As a result of the highly-doped absorbers and the concomitant reduced dependence of capacitance on reverse bias, the calculated OIP3 limited by $C(V)$ begins to approach the measured OIP3 only when the frequency is higher than 6 GHz. This indicates that $R(V)$ is the dominant nonlinear mechanism for frequen-

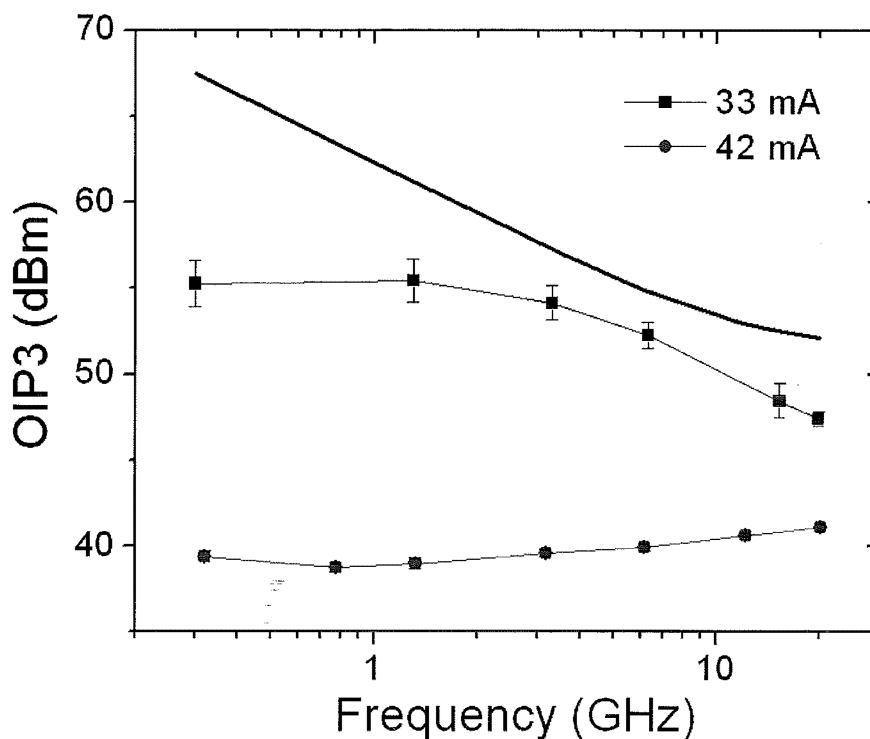


Figure 5.10 Measured OIP3 of HD-MUTC photodiode at 33 mA and 42 mA. The reverse bias is 10 V. Solid line: calculated OIP3 of HD-MUTC photodiode at 10V bias assuming that $C(V)$ is the primary nonlinearity driver.

cies lower than 6 GHz. In the frequency range from 6 GHz to 20 GHz the OIP3 is determined by both $C(V)$ and $\mathcal{R}(V)$. The drop of OIP3 accelerates as the frequency approaches 20 GHz while the calculated OIP3 limited by $C(V)$ shows the opposite trend at high frequencies, which indicates that in addition to $C(V)$, other frequency-dependent nonlinear mechanisms such as carrier speed modulation caused by the voltage swing may also contribute to the decrease of OIP3 at high frequencies [8].

The frequency dependence of the OIP3 was also measured at a photocurrent of 42 mA and 10 V reverse bias, where the OIP3 is 39 dBm at 320 MHz and slightly increases to 41 dBm at 20 GHz. This indicates that the nonlinearity caused by $\mathcal{R}(V)$ is so strong that the $C(V)$ nonlinearity is by comparison negligible at least up to 20 GHz. This is consis-

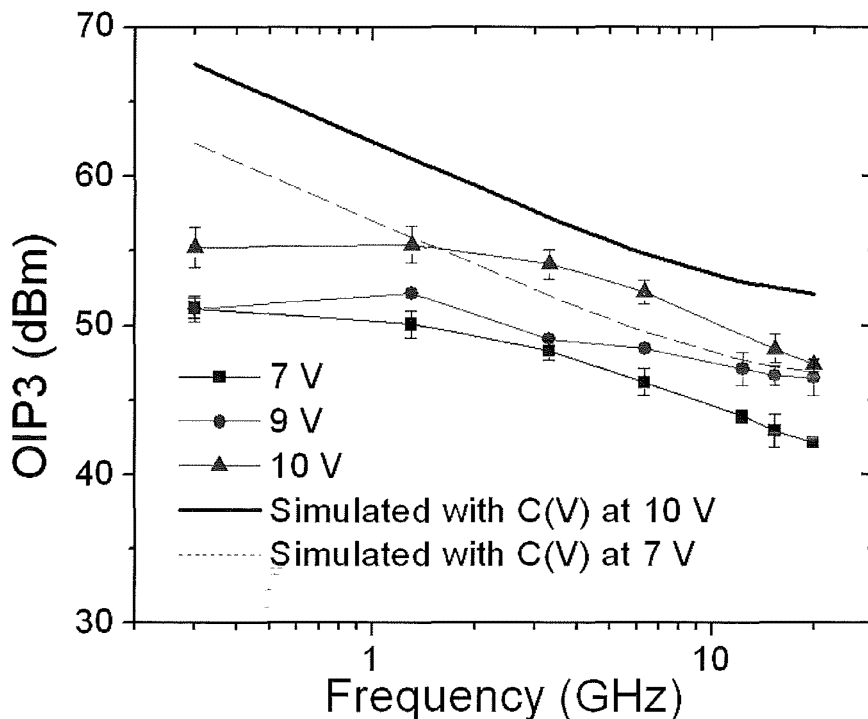


Figure 5.11 Frequency dependence of OIP3 of HD-MUTC at various reverse biases and their corresponding optimized photocurrents. Solid line: $C(V)$ -limited OIP3 at 10 V; Dashed line: $C(V)$ -limited OIP3 at 7 V.

tent with the calculation of OIP3 based on $C(V)$.

Figure 5.11 shows the measured frequency dependence of the OIP3 at different reverse bias and the corresponding optimized photocurrent levels (30.5 mA for 7 V, 32.5 mA for 9 V and 33 mA for 10 V). At 20 GHz the measured OIP3 increases monotonically with reverse bias. The dashed and solid lines in Figure 5.11 are the calculated $C(V)$ -limited OIP3 at 10 V and 7 V reverse bias, respectively. Since the derivative of capacitance with respect to bias, i.e. $dC(V)/dV$, decreases with increasing reverse bias, the $C(V)$ -limited OIP3 calculated from the equivalent circuit model increases with reverse

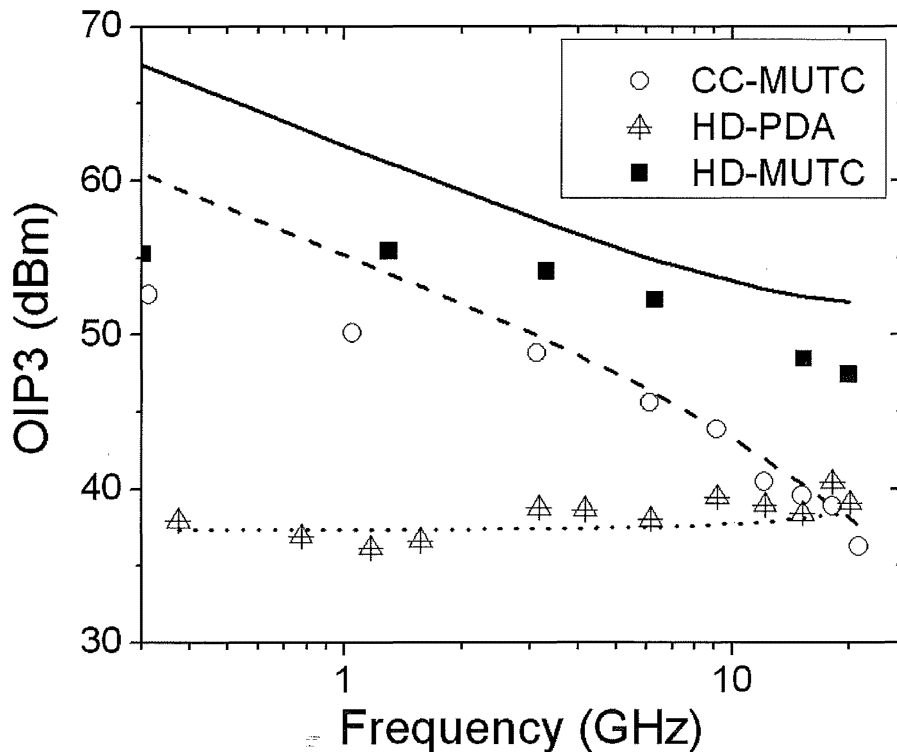


Figure 5.12 Measured OIP3 of (1) CC-MUTC photodiode at 50 mA and $V_b = -7$ V, (2) HD-PDA photodiode at 21 mA and $V_b = -8$ V, and (3) HD-MUTC photodiode at 33 mA and 10 V reverse bias. Solid line: calculated OIP3 of HD-MUTC photodiode based assuming the dominance of $C(V)$; Dashed line: calculated OIP3 of CC-MUTC photodiode assuming primary contributions from $C(V)$ and $C(I)$; Dotted line: calculated OIP3 of HD-MUTC photodiode assuming that $C(V)$ is the primary nonlinear driver.

bias. Thus increasing reverse bias is beneficial in improving the OIP3 of the photodiode especially at high frequencies.

The frequency dependence of the OIP3 of the HD-MUTC photodiodes is compared to that of the CC-MUTC photodiode and the HD-PDA photodiode, as shown in Figure 5.12. Since the OIP3 of all the photodiodes show certain dependence on photocurrent and reverse bias, in order to make fair comparisons each device was measured at the photocurrent and bias conditions that maximized their OIP3. As shown in Figure 5.12, although the CC-MUTC photodiode shows a high OIP3 at low frequencies, there is a 16 dB roll off as the frequency increases from 320 MHz to 21 GHz. This is caused by voltage-dependent capacitance $C(V)$ and photocurrent-dependent capacitance $C(I)$ as explained in Chapter 4. The calculated OIP3 of the CC-MUTC photodiode based on its $C(V)$ and $C(I)$ characteristic is shown as the dashed line in Figure 5.12, which agrees well with the measured OIP3 at high frequencies (> 6 GHz). The OIP3 of the HD-PDA photodiode slightly increases with frequency, which is similar to that of the HD-MUTC photodiode measured at non-optimized conditions (42 mA curve in Fig. 5). This indicates that the strong nonlinearities caused by the $\mathcal{R}(V)$ of the HD-PDA photodiode limit its OIP3 to values below 40 dBm. The OIP3 limited by the $\mathcal{R}(V)$ of the HD-PDA was calculated and is shown as the dotted line in Figure 5.12; which shows good agreement with the measurements. The reduced frequency dependence of OIP3 of the HD-MUTC photodiode is due to the highly doped absorber, which significantly reduces the voltage dependence of capacitance and almost eliminates the photocurrent dependence of the capacitance.

5.3.4 Explanation for the Peak of OIP3 at Certain Photocurrent

As discussed in Section 5.3.3, the $R(V)$ curve of HD-MUTC can not be measured at high photocurrent levels due to the influence of ohmic heating and thus bias modulation techniques needs to be used to help determine the $R(V)$ curve at high photocurrent levels. In contrast to the three-tone measurement, which utilizes three optical signals modulated at different frequencies, the bias modulation method employs only one optically modulated signal at frequency f_1 and the reverse bias applied to the photodiode has the form $V_{\text{bias}}(t) = V_{\text{dc}} + V_0 \sin(2\pi f_2 t)$, where V_{dc} is the DC component and V_{ac} is a modulated voltage at fixed frequency f_2 and amplitude V_0 . For the measurements reported here $f_2 = 20$ kHz

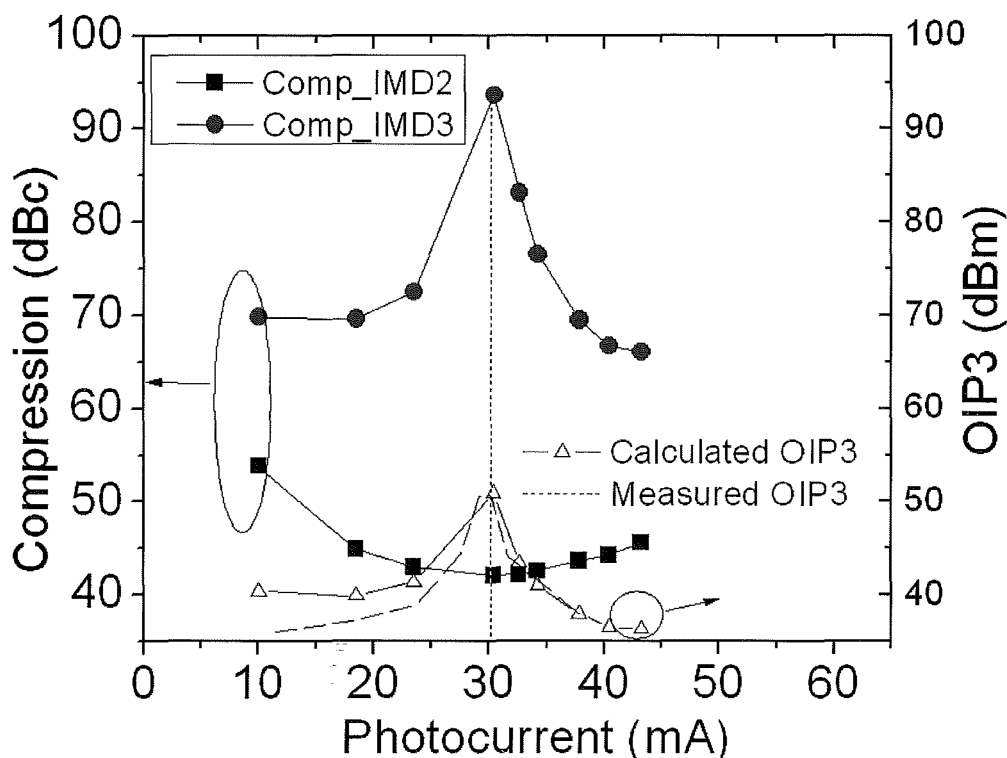


Figure 5.13 The compressions of IMD2 and IMD3 versus photocurrent. The calculated OIP3 based on the nonlinear parameters extracted from the measured compressions of IMD2 and IMD3 is compared with the OIP3 measured using three-tone techniques at 320 MHz and 7 V reverse bias.

and $V_0 = 1\text{V}$. The advantage of the bias modulation setup is that the measured intermodulation terms are relatively immune to the nonlinearities of the modulators as well as those of the signal generators that drive the modulators, as described in Chapter 3 and 4. With the bias modulation technique, the output photocurrent will exhibit components at the fundamental frequency f_1 and at the frequencies $f_1 \pm f_2$ and $f_1 \pm 2f_2$. The compression of the second order intermodulation terms, IMD2, are defined as $P_{f_1}/P_{f_1 \pm f_2}$ measured in dBc, similarly the compression of the third order intermodulation products, IMD3, is $P_{f_1}/P_{f_1 \pm 2f_2}$ measured in dBc. The compression of the IMD2 and the IMD3 of HD-MUTC were measured with this bias modulation approach at various photocurrent levels and the results are shown in Figure 5.13. The wavelength of the laser used in this bias modulation setup was 1545 nm and the laser was modulated at a fixed frequency of 320 MHz, which was low enough so that the contribution from the voltage-dependent capacitance $C(V)$ was negligible compared with that of $\mathcal{R}(V)$. V_{dc} was fixed at 7 V. As shown in Figure 5.13, both compression of IMD2 and IMD3 show some dependence on the photocurrent and, interestingly, the compression of IMD3 shows a peak at 30.5 mA, which is exactly the photocurrent that the OIP3 shows a peak when the reverse bias is 7 V.

As stated above, at low frequencies the OIP3 is determined by the relative voltage dependent responsivity $R(V)$. In order to relate the compression of IMD3 to OIP3, we first seek a relation between the compression of IMD3 and $R(V)$. According to the equivalent circuit model, the transient voltage drop across the load resistor $V(t)$ is the variable to be solved in equation (4.1). Using Harmonic the Balance Method similar to [24], $V(t)$ can be expanded as:

$$\begin{aligned}
 V(t) = & V_1 \sin(2\pi f_1 t + \phi_1) + V_2 \sin(2\pi f_2 t + \phi_2) + \\
 & + V_{21} \sin[2\pi(f_1 + f_2)t + \phi_{21}] + V_{22} \sin[2\pi(f_1 - f_2)t + \phi_{22}] + \dots
 \end{aligned}
 \tag{5.1}$$

Where $\phi_1, \phi_2, \phi_{21}, \dots$ are phase delays resulting from the capacitance of the PD. Inserting (5.1) into the differential equation (4.1) and using the orthogonality property of sine and cosine functions, we obtain a set of linear equations for V_1, V_2, V_{21}, \dots . In this way the power of the IMD2 and the fundamental power can be expressed as functions of the circuit parameters. Assuming that $R(V)$ has a form of $R(V) = 1 + a_1V + a_2V^2 + \dots$, to second order the compression of the IMD2 can be expressed as:

$$Comp_IMD2 = 10 \log_{10} \left(\frac{P_{f_1}}{P_{f_1 \pm f_2}} \right) = -10 \log_{10} \left(\frac{1}{2} a_1 V_0 \right)^2 \quad (5.2)$$

when the frequency is sufficiently low so that the contribution to the intermodulation from the voltage-dependent capacitance $C(V)$ is negligible compared with $\mathcal{R}(V)$. Similarly we can obtain the following expression for the compression of the IMD3:

$$Comp_IMD3 = 10 \log_{10} \left(\frac{P_{f_1}}{P_{f_1 \pm 2f_2}} \right) = -10 \log_{10} \left(\frac{1}{4} a_2 V_0^2 \right)^2 \quad (5.3)$$

Thus the absolute values of the nonlinear parameters a_1 and a_2 can be determined from the measured compression values and equations (5.2) and (5.3). However, additional information is required to determine the signs of a_1 and a_2 . A quadratic fit to the measured $\mathcal{R}(V)$ indicates that a_1 is positive and a_2 is negative when the photocurrent is low. The measured compressions of IMD2 indicate that the absolute value of a_1 never approaches zero in the range of photocurrent considered in this work. Hence, in the following a_1 will be assumed to be positive. The measured compressions of IMD3 indicate that the absolute value of a_2 decreases with photocurrent, approaches zero and then increases, which implies that a_2 is negative at low photocurrent levels and becomes positive at high photocurrent. Thus, we assume that the sign of a_2 is negative when the

photocurrent is less than or equal to 30.5 mA and positive when the photocurrent is larger than 30.5 mA.

In order to verify the effectiveness of the assumptions, the measured $R(V)$ curve at low photocurrent and the $R(V)$ curves deduced from the bias modulation measurements are shown in Figure 5.14. The responsivity is normalized relative to the absolute responsivity at 6 V because the DC bias is 7 V in this measurement and the deduced values of a_1 and a_2 are only valid in the vicinity of 7 V. As shown in Figure 5.14, the estimated $R(V)$ curve at 10 mA agrees reasonably well with the measured $R(V)$ at 50 μA . However, as the photocurrent starts to increase, the shape of the $R(V)$ begins to change probably due to thermal effect.

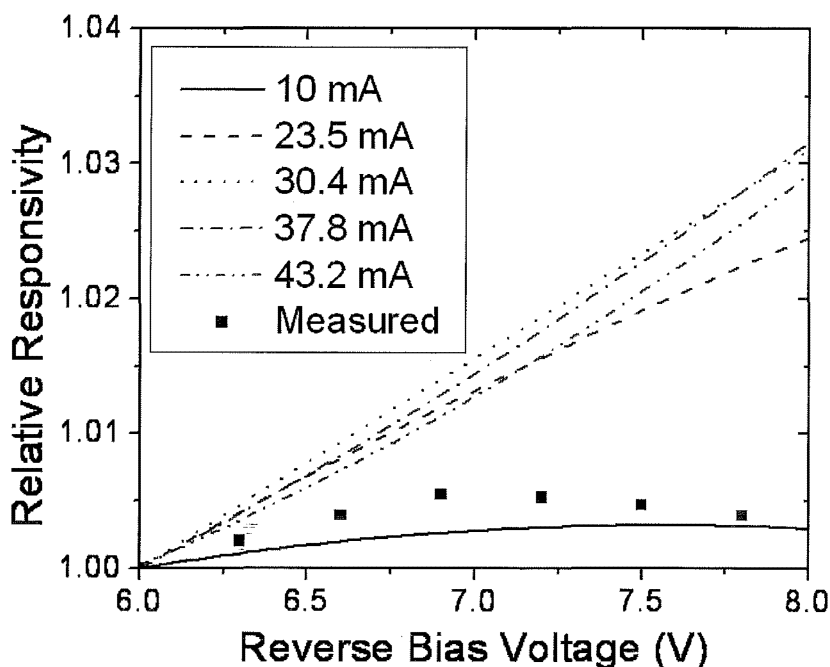


Figure 5.14 Measured $R(V)$ curve and the $R(V)$ curves determined from the bias modulation measurement

With these assumptions for a_1 and a_2 the OIP3 limited by the nonlinear $R(V)$ at various photocurrent levels can be calculated using the equivalent circuit model. If the $R(V)$ limited OIP3 is close to the OIP3 measured with three-tone technique, it means that $R(V)$ is the dominant mechanism. Otherwise, other nonlinear mechanisms dominate. The $R(V)$ limited OIP3 are calculated and the results are compared with the measured OIP3 in Figure 5.13. The calculated and measured OIP3 using the three-tone methods show good agreement within an error margin of 2 dB. The fact that the compressions of the IMD3, the calculated OIP3, and the measured OIP3 reach their peaks at exactly the same photocurrent is a strong indication that $R(V)$ is the dominant mechanism in HD-MUTC at 320 MHz and the dependence of OIP3 on photocurrent is related to a photocurrent induced change in the $R(V)$ curve: as photocurrent and reverse bias changes, the nonlinear parameters a_1 and a_2 change and at certain photocurrent and reverse bias conditions the nonlinear parameter a_2 , become almost zero. In other words, responsivity become a linear function of reverse bias at those specific conditions, and thus the IMD3 caused by $R(V)$, which is mainly associated with a_2 , become very small and results in high OIP3.

The reduction of a_2 may be caused by competing nonlinear mechanisms. It has been shown that $R(V)$ of photodiodes is mainly caused by Franz Keldysh effect and impact ionization in Chapter 4, and these two nonlinear effects can compensate each other and thus result in high OIP3. It is very likely that the minimization of a_2 and thus the peak of OIP3 is due to the compensation between two nonlinear effects at certain photocurrent and reverse bias conditions. As shown in Fig. 3, the photocurrent at which OIP3 shows a peak changes with reverse bias. This is likely due to the fact that both the Franz Keldysh effect and impact ionization are dependent on electric field and tempera-

ture, which are influenced by reverse bias and photocurrent. Similar photocurrent dependence of OIP3 is also observed in the CC-MUTC, but the OIP3 is less sensitive to photocurrent and reverse bias than the HD-MUTC. This is likely due to the fact that the CC-MUTC has a thinner intrinsic absorber (200 nm) than that of the HD-MUTC (300 nm) and thus suffers less from the Franz Keldysh effect and impact ionization. In this case less precise conditions of photocurrent and reverse bias are required for the Franz Keldysh effect and impact ionization to compensate each other.

5.4 Conclusions

In this chapter two novel photodiode structures, the HD-PDA and the HD-MUTC, have been developed in order to improve the OIP3 at high frequencies. Both structures include highly doped absorbers in order to minimize the dependence of capacitance on reverse bias and photocurrent. The OIP3 of the HD-PDA photodiode has a flat frequency response that remains as high as 39 dBm at 20 GHz. However, due to its thick depleted InGaAs absorber, the responsivity has relatively large dependence on reverse bias and thus the OIP3 is limited by $R(V)$ across the entire frequency range. The HD-MUTC was designed to improve the OIP3 of photodiode in all frequencies. The OIP3 of the HD-MUTC photodiode is 55 dBm at low frequencies with only slight roll off with frequency; at 20 GHz the OIP3 reaches 47.5 dBm. The excellent frequency behavior is due to the high doping levels in the undepleted absorber and the relatively thin depleted InGaAs absorber. The frequency dependence of OIP3 is well explained by the equivalent circuit model. The photocurrent dependence of the OIP3 of the HD-MUTC photodiode, as

determined by the bias modulation method, is primarily attributable to the change of the $R(V)$.

Chapter 6 High Power Photodiodes as Optoelectronic

Mixers

6.1 Introduction

Radio-over-fiber systems operating at millimeter-wave frequencies have great potential in providing future V-band (50-75 GHz) wireless networks with larger channel capacity. In this architecture the radio signals are generated at a central station and are distributed to and from the radio base stations as millimeter wave-modulated optical signals, as shown in Figure 6.1. Due to the small coverage of millimeter-wave frequency radio signals, a lot of radio base stations are required; therefore, they must be simple,

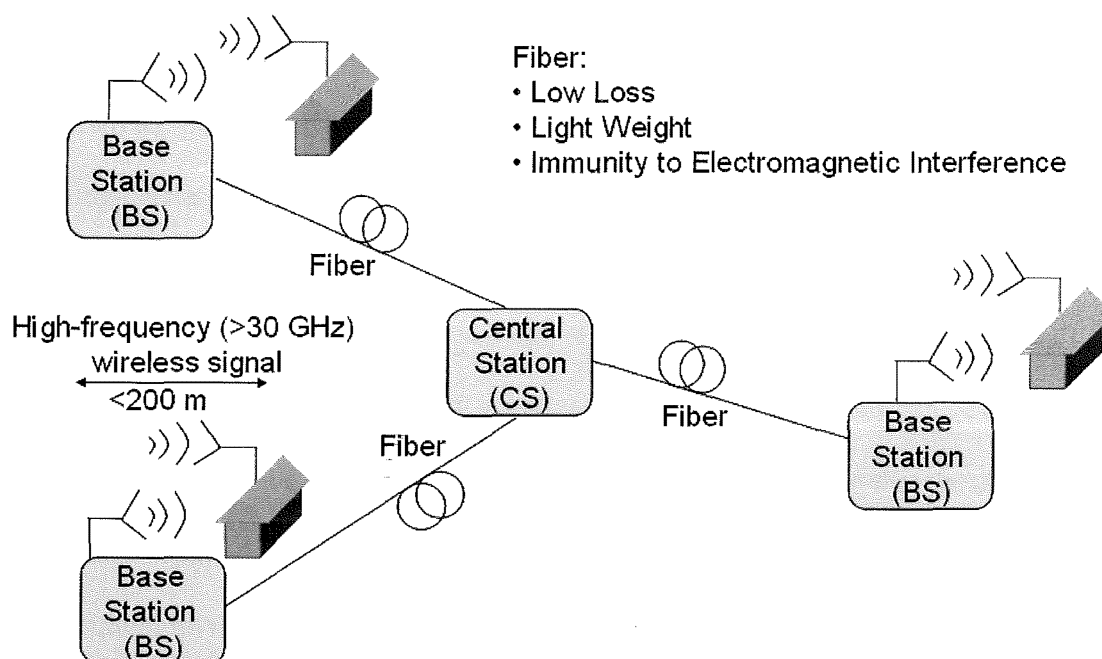


Figure 6.1 Schematic of Radio-over-fiber system for V-band wireless communication

compact, and low cost. Conventionally the optical subcarrier-modulated signals are converted to electrical signals with a linear-detection pin-photodiode and then up-converted by electrical frequency mixing. To simplify the frequency conversion scheme, pin-photodiodes operating in nonlinear detection mode were proposed to up-convert intermediate-frequency (IF) signals with both the local oscillator (LO) and the IF signals in optical form [10]. This direct frequency conversion scheme not only eliminated the necessity of using electrical mixers, but also allows the optical IF signal to be easily distributed from central stations to base stations through optical fibers. As the key component in this direct frequency conversion scheme, the photodiodes used as the optoelectronic (OE) mixers are required to deliver high up-converted radio-frequency (RF) signal power. However, pin-photodiodes suffer from severe space charge effect and the maximum power of the up-converted signal is very low. The highest up-converted signal power reported using a pin-photodiode as an OE mixer at V-band is only -50 dBm [10]. Uni-traveling-carrier (UTC) photodiodes as OE mixers have achieved higher up-converted RF power of -14.6 dBm at 60 GHz [37]. Recently a near-ballistic uni-traveling-carrier (NB-UTC) photodiode as OE mixer was also reported to have a relatively high up-converted RF power of -29 dBm at 60 GHz [38]. In this chapter, we demonstrate a modified uni-traveling-carrier (MUTC) photodiode as a high power OE mixer. The relative optical LO and IF signal levels and the reverse bias can be optimized for maximum up-converted power, and experimental results revealed that the optimum IF percentage $P_{\text{opt-IF}}/(P_{\text{opt-IF}}+P_{\text{opt-LO}})$ is approximately 1/3 for all photocurrent levels while the optimum reverse bias increases linearly with photocurrent. A simple analytical model based on the space charge effect was developed to explain the optimum IF percentage

and the photocurrent dependence of the optimum reverse bias. By optimizing the relative optical LO and IF signal levels and the reverse bias, a record high up-converted RF power of -4.7 dBm was achieved at 60 GHz when the photocurrent was 70 mA. Further studies show that the maximum up-converted RF signal power is only limited by the saturation effect of the photodiode.

6.2 Device Design and Measurement Setup

The device structure was grown on semi-insulating double-side-polished InP substrates by metal-organic chemical vapor deposition (MOCVD). A schematic cross section is shown in Figure 6.2. The epitaxial growth begins with a 200 nm-thick n⁺ InP layer, a 20-nm n⁺ InGaAs layer, and a 900-nm n⁺ InP. A 100-nm n-type InP layer with a doping

| |
|--|
| InGaAs, p ⁺ , Zn, 2.0×10^{19} , 50nm |
| InP, p ⁺ , Zn, 1.5×10^{18} , 100nm |
| InGaAsP, Q1.1, Zn, 2.0×10^{18} , 15nm |
| InGaAsP, Q1.4, Zn, 2.0×10^{18} , 15nm |
| InGaAs, Zn, 2.0×10^{18} , 100nm |
| InGaAs, Zn, 1.0×10^{18} , 150nm |
| InGaAs, Zn, 5.0×10^{17} , 200nm |
| InGaAs, Zn, 2.5×10^{17} , 200nm |
| InGaAs, n.i.d, $<1.0 \times 10^{16}$, 250nm |
| InGaAsP, Q1.4, n.i.d, $<1.0 \times 10^{16}$, 15nm |
| InGaAsP, Q1.1, n.i.d, $<1.0 \times 10^{16}$, 15nm |
| InP, Si, 5.0×10^{16} , 50nm |
| InP, Si, n.i.d, $<1.0 \times 10^{16}$, 700nm |
| InP, n ⁺ , Si, 1.0×10^{18} , 100nm |
| InP, n ⁺ , Si, 1.0×10^{19} , 900nm |
| InGaAs, n ⁺ , Si, 1.0×10^{19} , 20nm |
| InP, n ⁺ , Si, 1.0×10^{19} , 200nm |
| InP, semi-insulating substrate, Single side polished |

Figure 6.2 Schematic of the MUTC photodiode

concentration of $1 \times 10^{18} \text{ cm}^{-3}$ is then grown to reduce Si diffusion into the following 700 nm lightly-doped InP drift layer. Following the InP drift layer are two 15-nm lightly-doped InGaAsP transition layers, and then a 50-nm lightly-doped n- InP cliff layer. The $\text{In}_{0.53}\text{Ga}_{0.47}\text{As}$ absorbing region consists of a 250-nm unintentionally-doped n-layer that is depleted when the device is sufficiently reverse biased and four undepleted, step-graded $\text{In}_{0.53}\text{Ga}_{0.47}\text{As}$ layers. The two top layers are a 100-nm p^+ InP electron blocking layer and a 50-nm p^+ InGaAs contact layer. The two 15-nm InGaAsP quaternary layers are designed to “smooth” the abrupt conduction band barrier at the InGaAs-InP heterojunction interface. To assist carrier transport in the p-type absorbing layer, the doping was graded in four steps ($2.5 \times 10^{17} \text{ cm}^{-3}$, $5.0 \times 10^{17} \text{ cm}^{-3}$, $1.0 \times 10^{18} \text{ cm}^{-3}$ and $2.0 \times 10^{18} \text{ cm}^{-3}$) to create a quasi-electric field. Compared to the CC-MUTC design reported in Chapter 2, the thickness of the charge-compensated InP collector layer was increased from 605 nm to 700 nm to reduced the capacitance and thus increase the RC-limited bandwidth. The InP cliff layer, which is a thin moderately doped n-type InP layer, was added between the depleted InGaAs layer and the depleted InP layer to reduce the space charge effect at high photocurrent levels. Back-illuminated mesa structures were fabricated by inductive coupled plasma etching. Microwave contact pads and air-bridge connections to the top p-contact layer were fabricated for high-speed measurements. Finally, a 230-nm SiO_2 anti-reflection layer was deposited on the back of wafer. The MUTC photodiode has a high responsivity of 0.75 A/W, which compares favorably with the 0.15 A/W responsivity of the NB-UTC photodiode reported in [38]. The devices were mounted on a thermoelectric heat sink for testing. The MUTC photodiode studied in this work has a diameter of 20 μm , which corresponds to an active area of 314 μm^2 . Compared with the previously

reported UTC photodiode V-band mixer, which has an active area of $40 \mu\text{m}^2$ [37] and the NB-UTC photodiode, which has an active area of $100 \mu\text{m}^2$ [38], the relatively large active area of the MUTC photodiode allows larger tolerance in alignment and undercut during chemical etching of the mesa structure, which significantly eases the fabrication process. However, this large active area did not harm the high-power performance of the photodiode in V-band, which will be discussed later.

A block diagram of the measurement setup for optical signal mixing with the MUTC photodiode is shown in Figure 6.3. Two tunable External Cavity Lasers (ECL) with a center wavelength near 1545 nm were used to create a 100% modulated LO signal

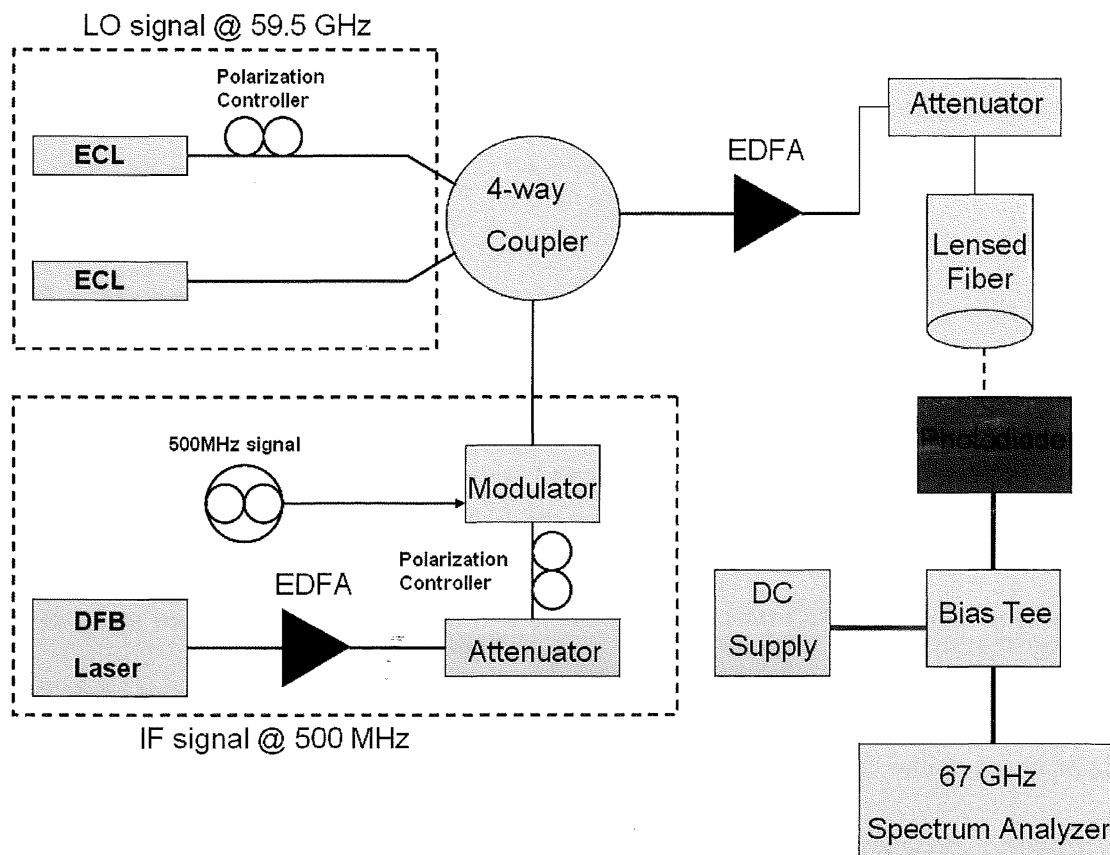


Figure 6.3 Measurement setup for optical signal mixing with photodiode

at 59.5 GHz by heterodyning. The optical IF signal at a center optical wavelength of 1543 nm was generated by modulating a DFB laser with an electro-optic modulator at a fixed frequency of 0.5 GHz. The modulator was driven at high power so that the IF signal was also 100% modulated. The optical LO and IF signals were combined through a 4-way coupler and then amplified by an EDFA. Since the optical LO and IF signals share a single EDFA, the ratio between the injected optical LO and IF power can be adjusted to optimize the up-conversion efficiency. The optical signal was then attenuated by an optical attenuator and coupled into the photodiode with a lensed fiber. The photodiode was biased with a low loss bias tee through which the signals produced by the photodiode were coupled into a Rohde & Schwarz FSU67 spectrum analyzer which has a maximum measurable frequency range of 67 GHz. The LO signal at 59.5 GHz and the up-converted RF signals at 59 GHz and 60 GHz produced by the photodiode were directly measured using the 67 GHz spectrum analyzer.

6.3 Measurement Results

The frequency response of the 20- μ m-diameter MUTC photodiode was measured by sweeping the frequency of the optical LO signal while keeping the IF signal off. The results are shown in Fig. 3. The MUTC photodiode exhibited a 3-dB bandwidth of 32 GHz when measured at 50 mA and 5 V reverse bias. At 60 GHz, the relative response decreased to approximately -8 dB. The measured junction capacitance was 61 fF and the series resistance was 5 Ω for the 20- μ m-diameter MUTC photodiode, which corresponds to an RC-limited bandwidth of 47 GHz. Assuming that the relative frequency response of

the photodiode is a combination of the RC effect and the transit time, the bandwidth is given by the following relation [39]:

$$B(f) = \frac{1}{\left(1 + \left(\frac{f}{BW_{RC}}\right)^2\right) \left(1 + \left(\frac{f}{BW_{TR}}\right)^2\right)} \quad (6.1)$$

where BW_{RC} is the RC limited 3-dB bandwidth and BW_{TR} is the transit-time limited 3-dB bandwidth. From the measured 3-dB bandwidth of 32 GHz and the RC limited bandwidth of 47 GHz, we can estimate the transit-time limited bandwidth by solving the equation $B(32 \text{ GHz}) = 0.5$. Thus we obtained an estimated transit-time limited bandwidth of $BW_{TR} = 53 \text{ GHz}$. Using equation (6.1), we can know that of the -8 dB loss at 60 GHz, -4.3

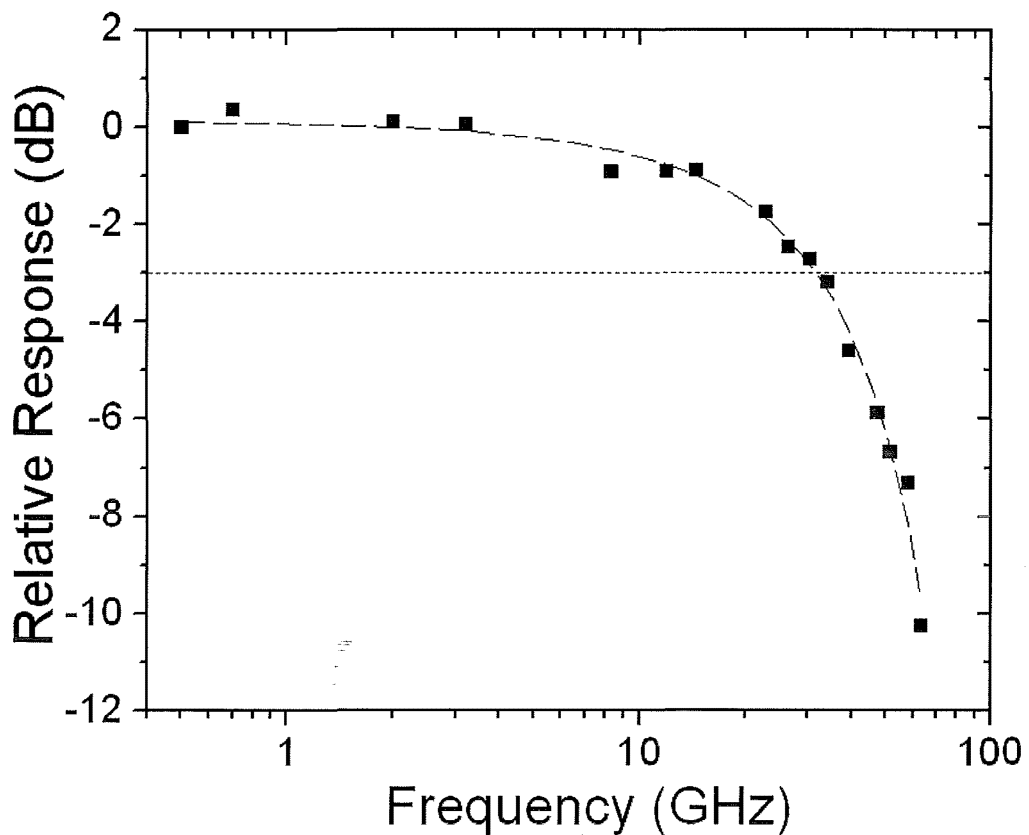


Figure 6.4 Relative frequency response of the MUTC photodiode measured at 50 mA and 5 V reverse bias.

dB is contributed by the RC effect while only -3.7 dB is contributed by the transit-time effect. It seems that the relatively large active area of the photodiode, which corresponds to a small RC-limited bandwidth, contributed to a significant portion to the loss of the RF power at 60 GHz. However, the maximum photocurrent is linearly proportional to the active area A , while the bandwidth is inversely proportional to the active area A . Thus the maximum output power $P_{\max} \propto I_{\max}^2 \propto A^2$, and power loss at a certain high frequency $B(f_0) \propto 1/A^2$ when $f_0 \gg f_{3dB}$. Thus the maximum power of the photodiode at a certain high frequency is $P_{\max} * B(f_0) = \text{constant}$. Within reasonable limits the output power is independent of the size of the photodiode. This can be beneficial since the relatively large active area of the photodiode eases the fabrication process but does not harm the maximum power that can be delivered at 60 GHz. The loss caused by the transit-time effect at 60 GHz could be reduced at the cost of using a thinner absorber, which would result in decreased responsivity or by using a waveguide structure which requires more complicated fabrication and optical alignment.

The optical IF percentage is defined as $P_{\text{opt-IF}} / (P_{\text{opt-IF}} + P_{\text{opt-LO}})$, where $P_{\text{opt-IF}}$ is the optical power of the IF signal and $P_{\text{opt-LO}}$ is the optical power of the LO signal. The optical IF percentage was adjusted to maximize the up-converted RF power at fixed photocurrent levels. As shown in Figure 6.5, at 30 mA of photocurrent and 1.5 V of reverse bias, the electrical power of the LO signal produced by the photodiode monotonically decreases with the optical IF percentage, which is due to the reduction of the optical LO signal. The up-converted RF power, however, reaches a “plateau” when the optical IF percentage is between 25% and 40%. Similar measurements have been carried out for various photocurrent levels and bias conditions and similar dependence of the up-

converted RF power on optical the IF percentage was observed. The optimum optical IF percentage centers near 33%. The up-converted RF power shows no significant difference when the optical IF percentage is between 25% and 40%. Thus all the measurements described in the following were carried out with the optical IF percentage fixed at 33%.

In order to explain the measured optimum IF percentage a simple analytical model was developed. It was suggested in Chapters 4 and 5 that both the nonlinear responsivity (voltage or photocurrent dependent responsivity) and the nonlinear capacitance (voltage or photocurrent dependent capacitance) contribute to the nonlinear frequency mixing process. We define conversion loss as P_{LO}/P_{IF} (dB), the ratio of the electrical power of the LO signal to the up-converted RF power measured in dB. In order to determine the dominant nonlinear mechanism in the MUTC photodiode studied in this

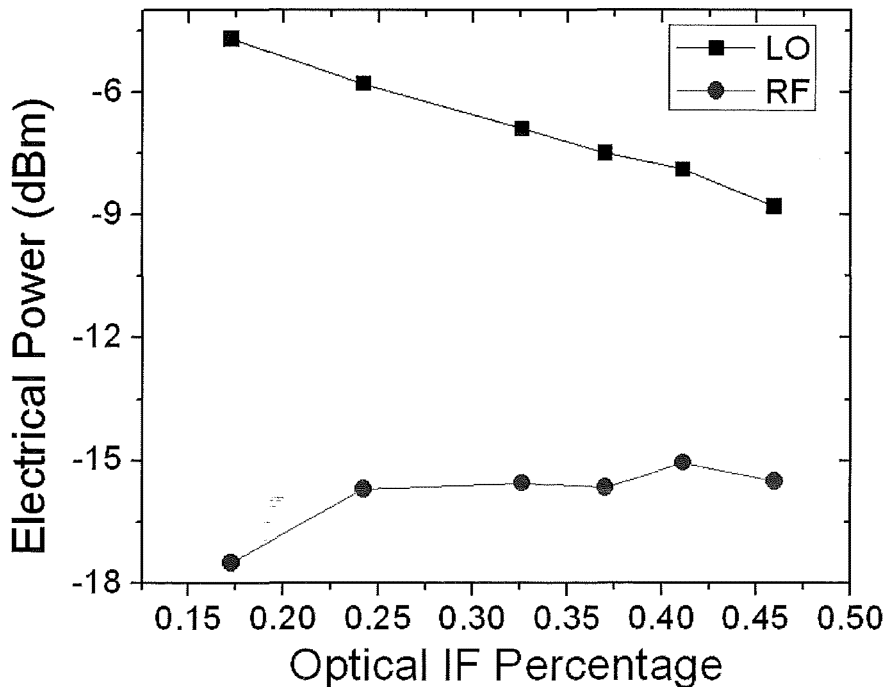


Figure 6.5 Measured electrical LO power and up-converted RF power versus optical IF percentage

work and thus simplify the expression for up-converted RF power, conversion loss was measured versus frequency at photocurrent levels of 30 mA and 70 mA. The reverse bias condition was optimized for the highest up-converted power; it was 1.4 V for 30 mA and 3.4 V for 70 mA.

As shown in Figure 6.6, the conversion loss is almost independent of frequency in the measured frequency range for both 30 mA and 70 mA. As suggested in Chapters 4 and 5, nonlinear responsivity is the dominant nonlinear mechanism if conversion loss (referred to as “compression” in Chapters 4 and 5) is independent of frequency while nonlinear capacitance is the dominant nonlinear mechanism if conversion loss decreases

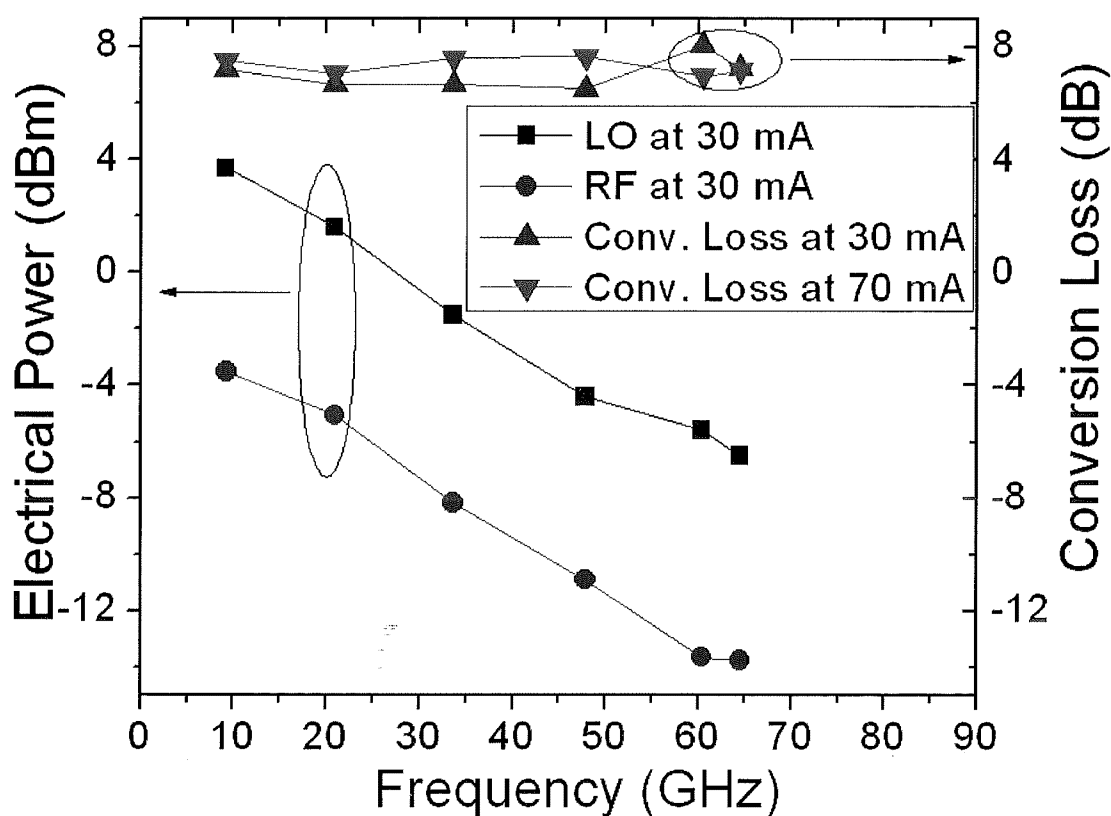


Figure 6.6 Conversion loss versus frequency at 30 mA and 70 mA. The LO and up-converted RF power versus frequency at 30 mA is also shown.

with frequency, since nonlinear responsivity leads to amplitude distortion which is independent of frequency while nonlinear capacitance leads to phase distortion which increases with frequency. Since the measured conversion loss is independent of frequency, we concluded that the nonlinear responsivity is the dominant nonlinear mechanism in the MUTC photodiode and the effect of nonlinear capacitance can be neglected.

6.4 Theoretical Calculations and Maximum Up-converted RF Power

When the MUTC photodiode is operated in saturation mode, the responsivity of the photodiode can be modulated by both photocurrent and reverse bias due to the space charge effect, as discussed in Chapters 3 and 4. When operating a photodiode under optical illumination the photocurrent induces a voltage drop across the series and load resistances. As a consequence, the bias voltage across the photodiode junction is modulated by the photocurrent [40], which will be referred to as “voltage swing” in this chapter. As the reverse bias on the photodiode decreases, the electric field in the photodiode also decreases and thus the responsivity of the photodiode is reduced when the photodiode is saturated. Thus the responsivity of the photodiode is modulated by the photocurrent through voltage swing effect. The photocurrent can also directly modulate the responsivity of the photodiode through space charge effect, since the injected electrons into the depleted region screen the ionized donor charge and thus decreases the electric field in the depletion region, which is similar to the effect of reducing the reverse bias of the photodiode. It is shown in [41] that the equivalent voltage drop due to photo-

current induced space charge effect is linearly proportional to the photocurrent, which can be written as $\Delta V = R_{sc} \times I$, where R_{sc} is the space charge resistance. In this way we consider that the responsivity modulation due to the space charge effect induced by photocurrent is equivalent to a voltage swing effect with photocurrent flowing through a load resistor of R_{sc} , and the equivalent voltage swing produced by both photocurrent induced space charge and a voltage swing together will be referred to as the “total equivalent voltage swing”, which can be calculated as

$$V_s = I[R_{sc} + R_L \sqrt{B(f)}] \quad (6.2)$$

where R_L is 55Ω which includes the 50Ω load resistance the 5Ω series resistance of the photodiode, and $B(f)$ is the frequency response of the photodiode in equation (6.1).

To get the expression for the optimum IF percentage, we also make the following assumption: the optimum condition for highest up-converted power is the condition when the amplitude of the total equivalent voltage swing equals the actual static reverse bias voltage applied on the photodiode. This assumption is based on the fact that if the bias voltage applied to the photodiode swings to the forward bias region, the output RF power of the photodiode will significantly degrade due to severe space charge effect [42]. On the other hand, if the static reverse bias voltage applied on the photodiode is so high that it can not be forced near the zero bias region by the photocurrent, the conversion efficiency will be low since photodiodes have strongest nonlinear effects near zero bias [43]. For the case of the OE mixing measurement in this work, the optimum condition can be written as:

$$V_{s-IF} = V_{s-LO} = V_b + \phi_{bi} - (I_{LO} + I_{IF})R_s \quad (6.3)$$

where I_{LO} and I_{IF} are the DC offsets of the photocurrent of the LO and IF signals, which are equal to the amplitude of the AC photocurrent of the LO and IF signals in the case of 100% modulation. $V_{s-IF} = I_{IF}[R_s + R_L\sqrt{B(0.5GHz)}]$ is the total equivalent voltage swing caused by the IF signal and $V_{s-LO} = I_{LO}[R_s + R_L\sqrt{B(59.5GHz)}]$ is the total equivalent voltage swing caused by the LO signal. V_b is the reverse bias provided by the voltage source and ϕ_{bi} is the build-in potential of the photodiode, which is approximately 0.5 V according to I-V measurements. $(I_{LO} + I_{IF})R_s$ is the static voltage drop caused by the total photocurrent. Using the measured optimum optical IF percentage of 33%, which corresponds to $I_{LO} = 2 \times I_{IF}$, we obtain $R_{sc} = 31 \Omega$ by solving equation (6.3). The validity of this calculated space charge resistance will be verified through a theoretical calculation in this

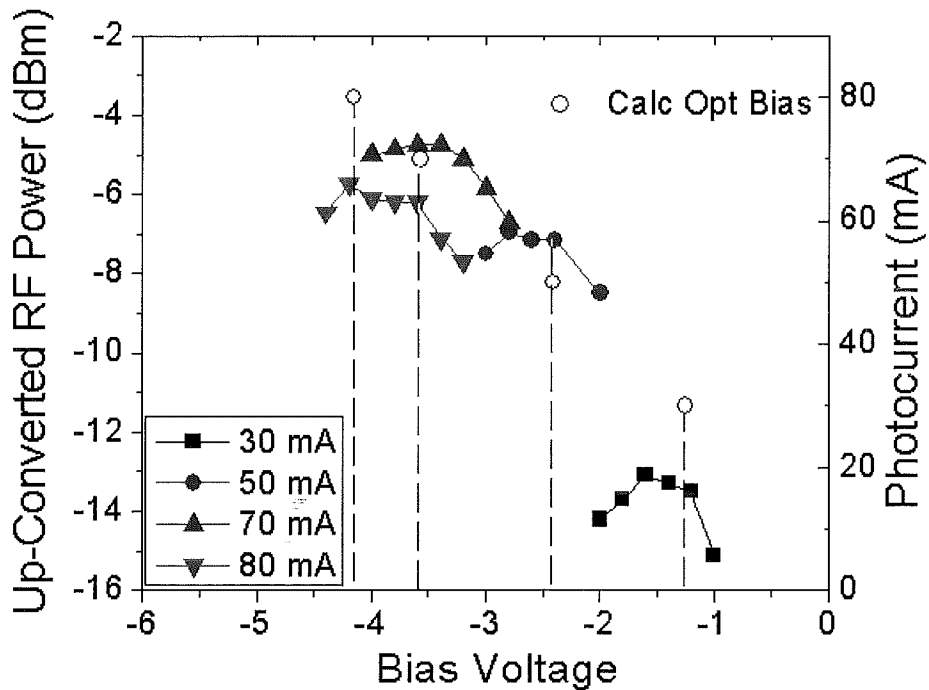


Figure 6.7 Filled shapes: measured up-converted power versus reverse bias at different photocurrent levels. Open circles: calculated optimum reverse bias.

chapter. Using equation (6.3) we can also estimate the optimal value of the reverse bias V_{b-opt} for maximum up-converted power. This enables us to confirm the validity of the calculated space charge resistance by calculating V_{b-opt} at different photocurrent levels and comparing the results with the measured values. Substituting $R_s=31 \Omega$ and $I_{LO} = 2 \cdot I_{IF}$ into equation (6.3), we obtain:

$$I_{IF}(R_s + R_L) = V_{b-opt} + \phi_{bi} - 3I_{IF}R_s. \quad (6.4)$$

Since the total photocurrent $I_{total} = I_{LO} + I_{IF} = 3I_{IF}$, we obtain from equation (6.4) that the optimum reverse bias is 1.3 V, 2.4 V, 3.6 V and 4.2 V when the total photocurrent is 30 mA, 50 mA, 70 mA and 80 mA. The bias dependence of the up-converted power at different photocurrent levels is shown in Fig. 5. At all measured photocurrent levels the up-converted power shows peaks at specific reverse bias value. The optimum reverse bias for maximum up-converted power increases with photocurrent and agrees well with the calculated values, which proves the effectiveness of the analytical model.

As reported in [41], space charge resistance has an analytical expression:

$$R_{sc} = \frac{d^2}{2\varepsilon_0\varepsilon_r vA} \quad (6.5)$$

where d is the effective depletion width of the photodiode, A is the active area of the photodiode, v is a velocity of the electrons and ε_r is the relative dielectric constant of the depletion region. Equation (6.5) appears simple and concise but accurately calculating the space charge resistance R_{sc} is difficult due to uncertainty of some of the parameters. The depletion width d is not necessarily the total thickness of the depleted layers shown in Figure 6.1 since we have observed significant Zn diffusion from the p-doped InGaAs layer into the lightly n-doped InGaAs. In addition the 700 nm lightly n-doped InP layer

will not be fully depleted under the condition of low reverse bias and high photocurrent injection, which is necessary for the OE mixing measurement. The electron velocity in InP will not be the saturation velocity since the field is low. If we take the following set of parameters to calculate R_{sc} : $\epsilon_0=8.85 \times 10^{-12}$ F/m, $\epsilon_r=13$, $v_s=1.6 \times 10^7$ cm/s, $d=600$ nm, and $A=314 \mu\text{m}^2$, which is reasonable under the conditions that the measurements were carried out, we obtain $R_{sc}=31 \Omega$, which is the value we calculated from the measurements described above. The calculation is relatively rough, and in the actual measurement R_{sc} is not necessarily a constant. However, both the optical IF percentage and the reverse bias values show an optimum range rather than specific values. R_{sc} in the range 20Ω to 40Ω yields reasonable optimum optical IF percentage and reverse biases consistent with the measured values.

As shown in Figure 6.7, the maximum up-converted RF power occurs when the photocurrent is 70 mA and the reverse bias is approximately 3.5 V. As the photocurrent increases from 70 mA to 80 mA, the maximum up-converted RF power decreases with photocurrent. As reported in [43], the up-converted RF power can be expressed as: $P_{RF}=\theta_{mix} * P_{LO}^2 * P_{IF}^2$, where θ_{mix} is the conversion efficiency, which is not the same as the conversion loss defined in this paper. The measured conversion loss near the optimum bias condition is 7 ± 1 dB for all photocurrent levels, which are not significantly different from each other. Thus according to the expression for the up-converted RF power, the maximum P_{RF} is primarily determined by the LO power P_{LO} and the IF power P_{LO} . The powers of the LO signals were also measured at different photocurrent levels and bias conditions. The results are shown in Figure 6.8. At the optimal bias condition, the largest LO power occurs at 70 mA. The LO powers at 80 mA are lower than those at 70 mA at

all measured bias conditions, which is due to the severe saturation effect caused by the extremely high photocurrent injection levels [15]. The measured IF powers show a similar trend to that of the LO. These measured results explain the reason that the maximum up-converted RF power occurs when the photocurrent is 70 mA and reveal the fact that the maximum up-converted RF power is primarily limited by the saturation characteristics of the photodiode. More advanced device structure designs might be applied to further improve the power capability of the MUTC photodiode as OE mixers.

6.5 Conclusion

In this chapter, a modified uni-traveling-carrier photodiode-based V-band optoelectronic mixer is demonstrated. It can up-convert intermediate-frequency (IF) signals with both the 59.5 GHz local oscillator (LO) and the IF signals in optical form. An

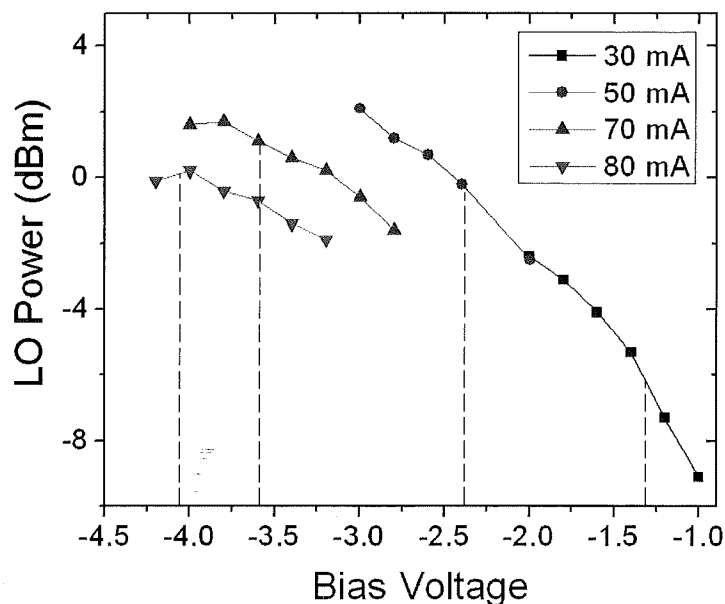


Figure 6.8 Measured LO power versus reverse bias at different photocurrent levels. Dashed lines: optimum reverse bias corresponding to those shown in Figure 6.7

analytical model was developed to explain the optimum IF percentage and the optimum reverse bias condition which is dependent on the photocurrent. By optimizing the IF percentage, photocurrent and bias conditions, a high up-converted RF power of -4.7 dBm was achieved. The maximum up-converted RF power is mainly limited by the saturation behavior of the photodiode.

Chapter 7 Conclusions and Future Work

7.1 Conclusions

In order to improve the power handling capability of photodiodes, I first studied the saturation mechanisms in UTC-type of photodiodes. It was found that the primary reason for saturation is that the bandgap discontinuity impedes electron transport into the InP drift layer when the electric field in the depleted InGaAs absorber collapses due to the space charge effect. The role of a cliff layer in UTC-type of photodiodes has been studied and it was found that a cliff layer is beneficial in suppressing the saturation effect in UTC-type photodiodes by enhancing the electric field in the depleted InGaAs layer and reducing that in the InP electron drift layer. A general design rule for the cliff layer to maximize the output power of this type of photodiode was formulated as: the total charge in the cliff layer should be as high as possible until the InP electron drift layer cannot maintain full depletion.

For better characterization of photodiode linearity, different measurement setups have been evaluated. The two-tone technique is a measurement setup that is widely used to determine the OIP3 of photodiodes. It is relatively easy to implement compared to the three-tone setup and it yields accurate values for OIP3 IF the modulator can be accurately biased at the quadrature point and the photocurrent is sufficiently large. The three-tone setup can accurately measure OIP3 without the influence of the modulator nonlinearities. However, an additional laser source, signal generator and modulator are required. I have also developed a new measurement setup that we refer to as “bias modulation”. It is a

very simple measurement setup and, like the three-tone measurement, it is immune to modulator nonlinearities. The bias modulation technique does not directly measure the OIP3 of photodiodes, but it does measure the intermodulation distortions caused by voltage-dependent nonlinearities separate from the influence of photocurrent-dependent nonlinearities. This makes the modulation measurement technique beneficial to quantitatively assess the significance of the voltage-dependent nonlinear mechanisms.

Detailed investigations were carried out to quantitatively identify the nonlinear mechanisms in CC-MUTC photodiodes. The responsivity of the CC-MUTC photodiode exhibits bias dependence, but no significant variation with photocurrent. The junction capacitance of the CC-MUTC photodiodes decreases with both reverse bias and photocurrent. A numerical equivalent circuit model was developed that confirms that the frequency characteristics of the OIP3 can be attributed to the changes of both the responsivity and device capacitance induced by the photocurrent and the transient voltage drop across the load and series resistors. This circuit model provided excellent agreement between the calculated OIP3 and measurements. Simulations on the OIP3 of CC-MUTC photodiodes suggest that the Franz-Keldysh effect and impact ionization are the primary origins of voltage-dependent responsivity $R(V)$, while low doping concentration in the p-type InGaAs absorber and space charge screening are responsible for the voltage-dependent capacitance and photocurrent-dependent capacitance $C(I)$, respectively. The equivalent circuit model was used to find the optimal wavelength for highest OIP3 at low frequencies; a high OIP3 of 57.5 dBm was obtained for the CC-MUTC at a low frequency of 152 MHz at the optimal wavelength of 1595 nm. Bias-modulated measurements were also carried out to verify the influence of the voltage-dependent

nonlinear mechanisms on photodiode nonlinearity. Good agreement between measurement results and the equivalent circuit analysis confirmed that the frequency characteristics of the intermodulation distortions are due to the voltage-dependent responsivity and capacitance. Based on the measurement results and the equivalent circuit analysis, we conclude that voltage-dependent responsivity $R(V)$, voltage-dependent capacitance $C(V)$ and photocurrent-dependent capacitance $C(I)$ are the primary nonlinear mechanisms in CC-MUTC photodiodes and need to be reduced further in order to improve the photodiode linearity.

In order to improve the OIP3 of photodiodes at high frequencies, two novel photodiode structures were designed, Partially Depleted Absorber Photodiodes with Highly Doped Absorbers (HD-PDA) and Modified Uni-Traveling-Carrier Photodiode with Highly Doped Absorbers (HD-MUTC). Both structures include highly doped absorbers in order to minimize the dependence of capacitance on reverse bias and photocurrent. The OIP3 of the HD-PDA photodiode exhibited a flat frequency response and at 20 GHz the OIP3 was as high as 39 dBm. The HD-MUTC was designed to improve the OIP3 of photodiodes over a broad frequency range (100 MHz to > 20 GHz). The OIP3 of these photodiodes was 55 dBm at low frequencies with only slight roll off with frequency; at 20 GHz the OIP3 was a record high 47.5 dBm. However, the OIP3 of the HD-MUTC photodiodes exhibit strong photocurrent dependence and the high OIP3 values can only be obtained within a narrow range of photocurrent. The photocurrent dependence of the OIP3, as determined by the bias modulation method, is primarily attributable to voltage-dependent variation of the responsivity, $R(V)$. The frequency dependence of the OIP3 of

both HD-PDA and HD-MUTC photodiodes are well explained by the equivalent circuit model.

I have also demonstrated that the high power photodiodes studied in this work can be used as optoelectronic mixers when operated at low bias conditions. A modified uni-traveling-carrier photodiode-based V-band optoelectronic mixer that can up-convert intermediate-frequency (IF) signals with both the 59.5 GHz local oscillator (LO) and the IF signals in optical form was successfully demonstrated. An analytical model was developed to explain the optimum IF percentage and the optimum reverse bias condition, which is dependent on the photocurrent. By optimizing the IF percentage, photocurrent, and bias conditions, a high up-converted RF power of -4.7 dBm was achieved.

7.2 Future Work

With the emergence of more and more applications for analog optical links, there is increasing demand for higher power handling capability and increased linearity of photodiodes. Several approaches may be helpful to further increase the maximum power and linearity of photodiodes.

7.2.1 Improved Device Structures

Although HD-MUTC shows high OIP3 in the entire frequency range, the OIP3 shows strong dependence on photocurrent and thus the high OIP3 occurs only in a narrow range of photocurrent. The device structure of the HD-MUTC can be modified to increase the range of photocurrent where the photodiodes show high OIP3. I have designed a new HD-MUTC structure (HD-MUTC2) to achieve this goal; it is shown in Figure 7.1. The InGaAs absorbing region primarily consists of a 500 nm-thick p^+ absorbing layer. In

order to enhance the electron transport in the doped absorber, the doping is graded in 10 steps from $5 \cdot 10^{19}$ to $5 \cdot 10^{18} \text{ cm}^{-3}$. Compared with my previous HD-MUTC design, the 24 nm-thick InGaAs/InAlAs chirped superlattice is replaced with a 30 nm-thick three-step InAlGaAs graded layer in order to avoid electron accumulation at the interface of the InGaAs/InAlAs chirped superlattice. The doping level and the thickness of the InP cliff layer are both increased to improve the power handling capability of the photodiode and to reduce the band discontinuity at the interface. The thickness of the depleted InGaAs layer is decreased from 300 nm to 150 nm in order to reduce the dependence of responsivity on reverse bias. The thickness of the depleted InP layer is increased from 400 nm to 900 nm in order to reduce the capacitance and the voltage swing effect. The background doping level in the unintentionally-doped absorbing layer was below $5 \cdot 10^{15} \text{ cm}^{-3}$.

The capacitance density of the designed HD-MUTC2 photodiode was simulated using the same commercial device simulator, APSYS, that was described in the previous

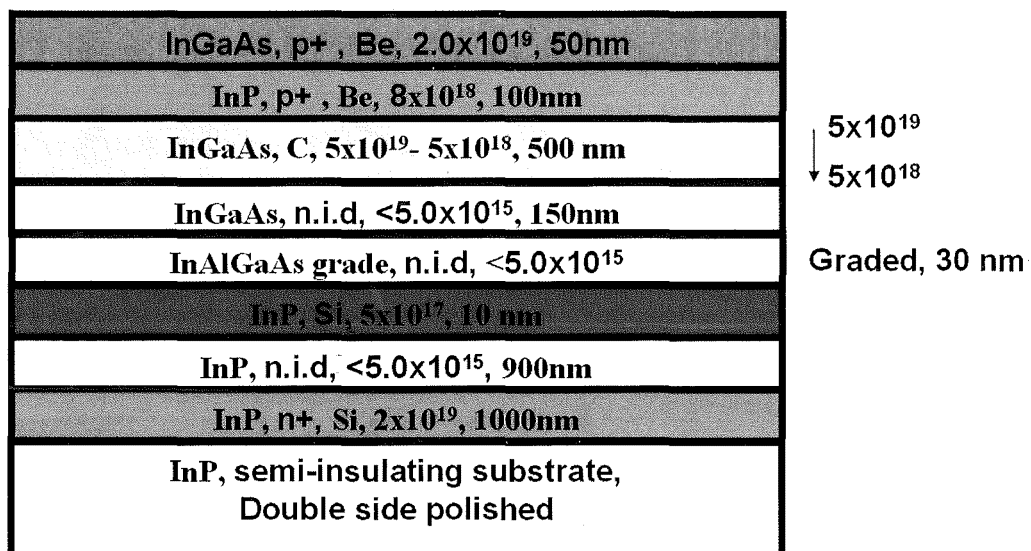


Figure 7.1 Schematic of HD-MUTC2

section and the results are compared with the measured data of the MUTC and HD-PDA photodiodes in Figure 7.2. As a result of the high doping level of the undepleted absorbers, the capacitance density of the HD-MUTC photodiodes has a significantly weaker dependence on reverse bias than that of the MUTC photodiodes when the bias is $> 4V$, which is similar to that of the HD-PDA photodiode and CC-MUTC photodiode. Also the capacitance density of the HD-MUTC2 is lower than that of the HD-PDA and CC-MUTC photodiodes as a result of its thick depleted layers (1050 nm). Also the C(V)-limited OIP3 of the HD-UTC photodiode will be higher than that of the HD-PDA and HD-MUTC photodiode due to its smaller capacitance density.

R(V) exhibits a weak correlation to the thickness of the depleted absorber. The thick-

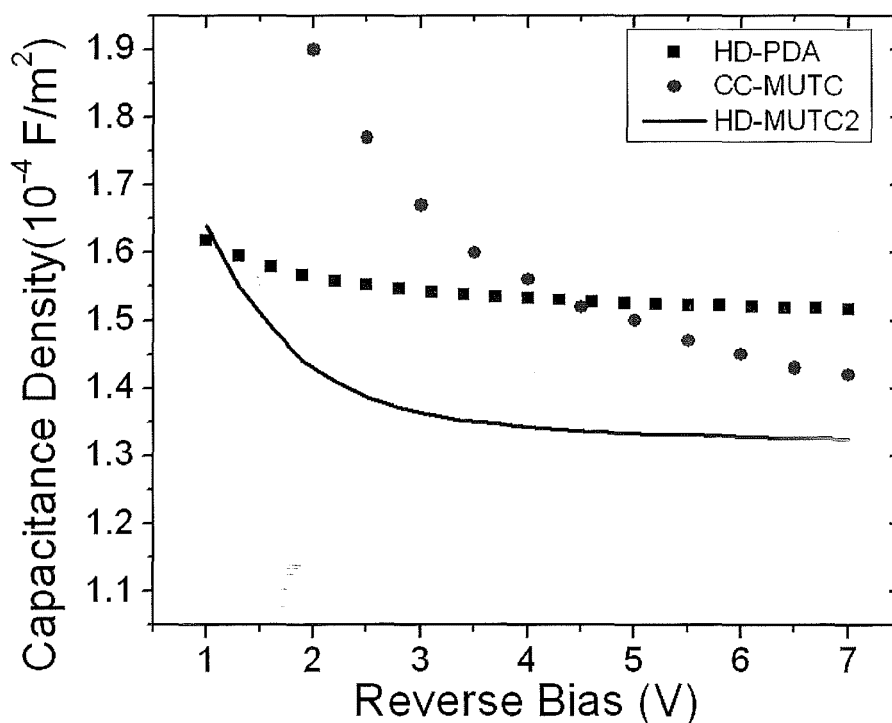


Figure 7.2 Measured junction capacitance density for MUTC photodiode, HD-PDA photodiode, and simulated junction capacitance density of HD-MUTC2 photodiode.

ness of the depleted absorber in the designed HD-MUTC is 150 nm, which is very thin compared with that of the HD-PDA (800 nm), the CC-MUTC (200 nm), and the HD-MUTC (300 nm). Further reduction of the thickness of the depleted InGaAs absorber might further reduce $R(V)$. However, this is also likely to result in smaller absolute responsivity. In order to avoid reducing the responsivity due to the reduced thickness of the depleted InGaAs layer, a waveguide structure can be considered although this would result in more complex fabrication, reduced input coupling tolerance, and higher current densities.

7.2.2 Wilkinson Power Combiner

As discussed, there are physical limits and performance tradeoffs associated with increasing the output power and achieving higher linearity using a single photodiode. In

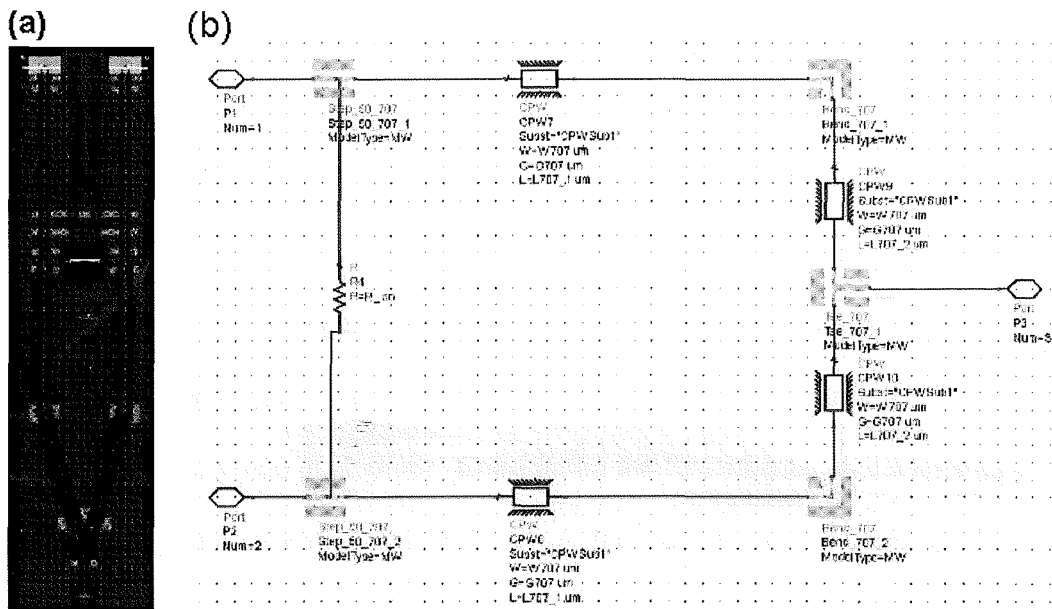


Figure 7.3 (a) mask design and (b) the equivalent circuit model of the photodiode pair coupled to a Wilkinson power combiner

order to achieve both improved OIP3 and output RF power, a two-way Wilkinson power combiner can be designed that incorporates a pair of photodiodes. The mask design and the equivalent circuit model of the two-way Wilkinson power combiner are shown in Figure 7.3. For this particular design, the center frequency of the Wilkinson combiner is centered at 20 GHz. In addition, a microwave tuning circuit, which matches the impedance of each photodiode to 50Ω at 20 GHz, is attached to each photodiode. We note however that the center frequency can be tuned to a wide range of frequencies by changing the parameters of the combiner such as line width, line length, and thickness of the strip line metal.

The voltage swing versus frequency has been simulated for the combiner and a discrete photodiode. Figure 7.4 shows the voltage swing versus frequency for photocurrent of 10 mA in the discrete photodiode and 10 mA in each of the photodiodes in the combiner. The voltage swing on the load resistor, V_{Load} , of the combiner is 1.4 times larger than the V_{Load} discrete photodiode due to the power combiner, which corresponds to a 3 dB improvement of output power of the combiner compared to that of the discrete photodiode [44]. Due to the isolation nature of the Wilkinson combiner at its designed center frequency [44], the voltage swing on the photodiode, V_{PD} , of each photodiode in the combiner and V_{PD} of the discrete photodiode are almost the same at 20 GHz, which means that the IMD3 produced by each photodiode in the combiner is the same as that produced by that discrete photodiode. Considering the fundamental characteristics of the power combiner, the power of IMD3 P_{IMD3} on the load of the combiner is also 3 dB larger than the P_{IMD3} on the load of the discrete photodiode at 20 GHz. Since OIP3 is defined as $\text{OIP3} = P_f + (P_f - P_{\text{IMD3}}) / 2$, and since both P_f and P_{IMD3} on the load of the

combiner are 3 dB larger than those on the load of the discrete photodiode, it follows that the OIP3 of the combiner will be 3 dB higher than that of the discrete photodiode at 20 GHz. Further expansion of the scale of the Wilkinson power combiner will lead to further improvements in power and OIP3. In general, an N element Wilkinson power combiner will lead to $10\log_{10}N$ dB improvement in both power and OIP3.

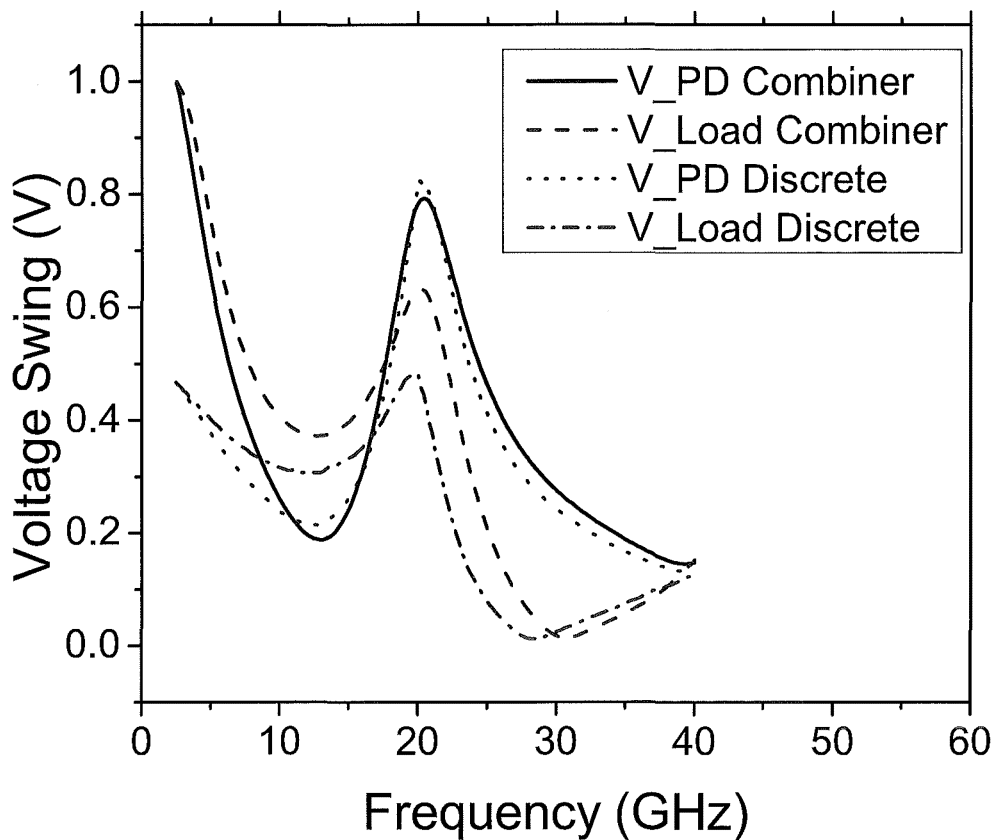


Figure 7.4 Simulation of the amplitude of voltage swing assuming a photocurrent of 10 mA. Solid line: voltage swing amplitude on the photodiode for the combiner design; Dashed line: voltage swing amplitude on the load for the combiner design; Dotted line: voltage swing amplitude on the photodiode for the discrete photodiode with tuning circuits. Dash dot line: voltage swing amplitude on the load for the discrete photodiode with tuning circuits.

Appendix A: Publications

- [1]. Zhi Li, **Huapu Pan**, Joe Campbell, “High-Power Integrated Balanced Photodetector”, *Photon. Tech. Lett.*, vol. 21, pp. 1858-1860, 2009.
- [2]. **Huapu Pan**, Zhi Li, and Joe C. Campbell, Characterization of High-Linearity Modified Uni-Traveling Carrier Photodiodes Using Three-Tone and Bias Modulation Techniques, *J. Lightwave Tech.*, 2009, accepted
- [3]. **Huapu Pan**, Zhi Li, and Joe C. Campbell, “High-Power High-Responsivity Modified Uni-Traveling-Carrier Photodiode Used as V-Band Optoelectronic Mixers”, *J. Lightwave Tech.*, 2009, accepted
- [4]. **Huapu Pan**, Zhi Li, Andreas Beling, and Joe C. Campbell, “Measurement and Modeling of High-Linearity Modified Uni-Traveling Carrier Photodiode with Highly-Doped Absorber”, *Optics Express*, 2009, Vol. 17, Iss. 22, pp. 20221–20226 (2009)
- [5]. **Huapu Pan**; Beling, A.; Campbell, J.C.; , "High-Linearity Uni-Traveling-Carrier Photodiodes," *Photonics Technology Letters, IEEE* , vol.21, no.24, pp.1855-1857, Dec.15, 2009
- [6]. Han-Din Liu, **Huapu Pan**, Chong Hu, Dion McIntosh, Yimin Kang, and Joe Campbell, “Avalanche Photodiode Punch-Through Gain Determination Through Excess Noise Analysis”, *J. Appl. Phys.*, **106**, 064507, (2009)
- [7]. **Huapu Pan**, P. D. Yoder, Andreas Beling, Hao Chen, and Joe C. Campbell, “A High-Linearity Modified Uni-Traveling Carrier Photodiode with Offset Effects of Nonlinear Capacitance”, *J. Lightwave Tech.*, vol. 27, no. 20,

pp. 4435-4439, 2009

- [8]. Yang Fu, **Huapu Pan**, and Joe C. Campbell, "Photodiodes with Monolithically Integrated Wilkinson Power Combiner", *Quantum Electronics, IEEE Journal of*, 2009, to be published
- [9]. Hao Chen, Andreas Beling, **Huapu Pan**, and Joe C. Campbell, "A Method to Estimate the Junction Temperature of Photodetectors Operating at High Photocurrent", *J. Lightwave Tech.*, 2009, to be published
- [10]. Andreas Beling, Hao Chen, **Huapu Pan**, and Joe C. Campbell, "High-Power Monolithically Integrated Traveling Wave Photodiode Array", *Photon. Tech. Lett.*, 2009, to be published
- [11]. **Huapu Pan**; Beling, A.; Hao Chen; Campbell, J.C., "The Frequency Behavior of the Intermodulation Distortions of Modified Uni-Traveling Carrier Photodiodes Based on Modulated Voltage Measurements," *Quantum Electronics, IEEE Journal of*, vol.45, no.3, pp.273-277, March 2009
- [12]. Andreas Beling, **Huapu Pan**, and Joe C. Campbell, "High-Power High-Linearity InGaAs/InP Photodiodes", *ECS Trans.* vol. 16, pp. 39-48 (2009)
- [13]. A. Beling, **H. Pan**, H. Chen, J. C. Campbell, "Measurement and modeling of high-linearity partially depleted absorber photodiode", *Electronics Letters*, vol. 44, no. 24, p 1419 - 1420, Nov. 20, 2008
- [14]. Andreas Beling, **Huapu Pan**, Hao Chen, and Joe C. Campbell, "Linearity of Modified Uni-Traveling Carrier Photodiodes" *J. Lightwave Tech.*, vol. 26, pp. 2373 – 2378, Aug.1, 2008

- [15]. Andreas Beling, **Huapu Pan**, Hao Chen, and Joe C. Campbell, "Measurement and Modeling of a High-Linearity Modified Uni-Traveling Carrier Photodiode" *Photon. Tech. Lett.*, vol. 20, no. 14, pp. 1219-1221, 15 July 2008.
- [16]. **H. Pan**, A. Beling, H. Chen, J. C. Campbell, "Characterization and Optimization of High-Power InGaAs/InP Photodiodes", *Optical and Quantum Electronics*, vol. 40, no. 1, p. 41 – 46, Jul. 2, 2008
- [17]. Handin Liu; Mcintosh, D.; Xiaogang Bai; **Huapu Pan**; Mingguo Liu; Campbell, J.C.; Ho Young Cha, "4H-SiC PIN Recessed-Window Avalanche Photodiode With High Quantum Efficiency," *Photonics Technology Letters, IEEE* , vol.20, no.18, pp.1551-1553, Sept.15, 2008
- [18]. **Huapu Pan**, Liwei Huang, et. al., "Finite Element Model of GaN Based LED and the Optimization of the Mesa Structure", *Chinese Journal of luminescence*, Vol. 28, No. 1, pp. 114-120, 2007
- [19]. Ti Li, **Huapu Pan**, et. Al, "Optimization of Electron Blocking Layer in GaN Laser Diode", *Chinese Journal of Semiconductors*, 2006, **27**(8), 1458-1462
- [20]. Rui Li, Tao Dai, Ling Zhu, **Huapu Pan**, et. al., "The reactive ion etching characteristics of AlGaIn/GaN SLs and etch-induced damage study of n-GaN using Cl₂/SiCl₄/Ar plasma", *Journal of Crystal Growth* 298 (2007) 375 – 378
- [21]. Zhuo Chen, Zhongyun Wu, Lianming Tong, **Huapu Pan**, et. al., "Simultaneous Dielectrophoretic Separation and Assembly of Single-Walled Carbon Nanotubes on Multi-Gap Nanoelectrodes and Their Thermal Sensing Properties", *Anal. Chem.* 2006, 78 (23), pp 8069–8075
- [22]. **Huapu Pan**, Yang Fu, Zhi Li, Joe C. Campbell, "High-Linearity Modified

- Uni-Traveling Carrier Photodiode with Reduced Frequency Dependence of Third-Order Intercept Point”, 2010, Conference on Optical Fiber Communication, to be published.
- [23]. **Huapu Pan**, Zhi Li, Joe C. Campbell, “Modified uni-traveling-carrier photodiode-based V-band optoelectronic mixers with high up-converted power and high responsivity”, *2010 SPIE Photonics West*, San Francisco, CA, January, 2010, to be published
- [24]. **Huapu Pan**, Andreas Beling, Hao Chen, and Joe C. Campbell, “Reduced Frequency Dependence of Third Order Nonlinearities in Partially-Depleted-Absorber Photodiodes”, *2009 International Conference on Indium Phosphate and Related Materials (IPRM 2009)*, Newport Beach, CA, May 2009, p 147 - 148
- [25]. **Huapu Pan**, Andreas Beling, Hao Chen, and Joe C. Campbell, “The Behavior of the Intermodulation Distortions of Modified Uni-Traveling Carrier Photodiodes Produced by Bias Modulation,” The 7th International Conference on Optical Communications and Networks (ICOON 2008), PhotonicsGlobal@Singapore, Dec. 8-11, 2008, p 1-4.
- [26]. A. Beling, **H. Pan**, H. Chen, J. C. Campbell, A. Hastings, D.A. Tulchinsky, and K. J. Williams, “Impact of Voltage-Dependent Responsivity on Photodiode Non-Linearity,” *2008 LEOS Annual Meeting*, Newport Beach, CA, November 2008, p 157-158
- [27]. A. Beling, **H. Pan**, H. Chen, and J. C. Campbell, “High-Power High-Linearity Modified Uni-Traveling Carrier Photodiodes”, *Integrated Photonics*

and Nanophotonics Research and Applications (IPNRA), Boston, Massachusetts, July, 2008, paper IWC3

- [28]. Andreas Beling, **Huapu Pan**, Hao Chen, and Joe C. Campbell, "High-Power Modified Uni-Traveling Carrier Photodiode with > 50 dBm Third Order Intercept Point," *2008 Int. Microw. Symp. (IEEE-IMS 2008)*, Atlanta, GA, June 2008., p 499-502
- [29]. **Huapu Pan**, Andreas Beling, Hao Chen, Joe C. Campbell, and P. D. Yoder, "The Influence of Nonlinear Capacitance on the Linearity of a Modified Uni-Traveling Carrier Photodiode," *2008 International Topical Meeting on Microwave Photonics*, Gold Coast, Australia, October, 2008, p 82-85
- [30]. Andreas Beling, **Huapu Pan**, and Joe C. Campbell, "High-Power High-Linearity InGaAs/InP Photodiodes," *214th Meeting of the Electrochemical Society*, Hawaii, October, 2008.
- [31]. A. Beling, **Huapu Pan**, Hao Chen, and J. C. Campbell, "Two-tone characterization of high-power modified uni-traveling carrier photodiode," *LEOS 2007. 20th Annual Meeting of the IEEE Lasers and Electro-Optics Society*, 2007, p 389-90
- [32]. **H. Pan**, A. Beling, H. Chen, J. C. Campbell, "Characterization and Optimization of InGaAs/InP Photodiodes with High Saturation Current", *Proceedings of NUSOD 2007*, paper WC31, pp. 79-80, Sep. 2007
- [33]. Han-Din Liu; McIntosh, D.; Xiaogang Bai; **Huapu Pan**; Mingguo Liu; Campbell, J.C., "4H-SiC PIN recessed window avalanche photodiode", *20th Annual Meeting of the IEEE Lasers and Electro-Optics Society (LEOS 2007)*,

pp. 517-18, Oct. 2007

Bibliography

- [1] W. A. Gambling, "The rise and rise of optical fibers," *Selected Topics in Quantum Electronics, IEEE Journal of*, vol. 6, no. 6, pp. 1084-1093, 2000.
- [2] Y. Liu, J. Yao, and J. Yang, "Wideband true-time-delay unit for phased array beamforming using discrete-chirped fiber grating prism," *Optics Communications*, vol. 207, no. 1-6, pp. 177-187, 2002.
- [3] N. Pleros, K. Vyrsoinos, K. Tsagkaris, and N. D. Tselikas, "A 60 GHz Radio-Over-Fiber Network Architecture for Seamless Communication With High Mobility," *Lightwave Technology, Journal of*, vol. 27, no. 12, pp. 1957-1967, 2009.
- [4] R. H. Walden, "Analog-to-digital converter survey and analysis," *Selected Areas in Communications, IEEE Journal on*, vol. 17, no. 4, pp. 539-550, 1999.
- [5] R. A. Minasian, "Photonic signal processing of microwave signals," *Microwave Theory and Techniques, IEEE Transactions on*, vol. 54, no. 2, pp. 832-846, 2006.
- [6] K. J. Williams, L. T. Nichols, and R. D. Esman, "Photodetector nonlinearity limitations on a high-dynamic range 3 GHz fiber optic link," *Lightwave Technology, Journal of*, vol. 16, no. 2, pp. 192-199, 1998.
- [7] Z. Sen Lin, P. M. Lane, and J. J. O'Reilly, "Assessment of the nonlinearity tolerance of different modulation schemes for millimeter-wave fiber-radio systems using MZ modulators," *Microwave Theory and Techniques, IEEE Transactions on*, vol. 45, no. 8, pp. 1403-1409, 1997.

- [8] K. J. Williams, R. D. Esman, and M. Dagenais, "Nonlinearities in p-i-n microwave photodetectors," *Lightwave Technology, Journal of*, vol. 14, no. 1, pp. 84-96, 1996.
- [9] J. Genest, M. Chamberland, P. Tremblay, and M. Tetu, "Microwave signals generated by optical heterodyne between injection-locked semiconductor lasers," *Quantum Electronics, IEEE Journal of*, vol. 33, no. 6, pp. 989-998, 1997.
- [10] M. Tsuchiya and T. Hoshida, "Nonlinear photodetection scheme and its system applications to fiber-optic millimeter-wave wireless down-links," *Microwave Theory and Techniques, IEEE Transactions on*, vol. 47, no. 7, pp. 1342-1350, 1999.
- [11] L. Xiaowei, L. Ning, Z. Xiaoguang, S. Demiguel, J. C. Campbell, D. A. Tulchinsky, and K. J. Williams, "High-saturation-current InP-InGaAs photodiode with partially depleted absorber," *Photonics Technology Letters, IEEE*, vol. 15, no. 9, pp. 1276-1278, 2003.
- [12] G. A. Davis, R. E. Weiss, R. A. LaRue, K. J. Williams, and R. D. Esman, "A 920-1650-nm high-current photodetector," *Photonics Technology Letters, IEEE*, vol. 8, no. 10, pp. 1373-1375, 1996.
- [13] N. Li, X. Li, S. Demiguel, X. Zheng, J. C. Campbell, D. A. Tulchinsky, K. J. Williams, T. D. Isshiki, and G. S. Kinsey, "High-saturation-current charge-compensated InGaAs/InP uni-traveling-carrier photodiode," *The 16th Annual Meeting of the IEEE Lasers and Electro-Optics Society (LEOS), Tucson, AZ*, vol. 2, pp. 790-791, 2003.

- [14] D.-H. Jun, J.-H. Jang, I. Adesida, and J.-I. Song, "Improved Efficiency-Bandwidth Product of Modified Uni-Traveling Carrier Photodiode Structures Using an Undoped Photo-Absorption Layer," *Japanese Journal of Applied Physics*, vol. 45, no. 4B, pp. 3475 - 3478, 2006
- [15] W. Xin, D. Ning, C. Hao, and J. C. Campbell, "InGaAs/InP Photodiodes With High Responsivity and High Saturation Power," *Photonics Technology Letters, IEEE*, vol. 19, no. 16, pp. 1272-1274, 2007.
- [16] D. Ning, W. Xin, L. Ning, L. Han-Din, and J. C. Campbell, "Thermal Analysis of High-Power InGaAs–InP Photodiodes," *Quantum Electronics, IEEE Journal of*, vol. 42, no. 12, pp. 1255-1258, 2006.
- [17] S. Srivastava and K. P. Roenker, "Numerical modeling study of the InP/InGaAs uni-travelling carrier photodiode," *Solid-State Electronics*, vol. 48, no. 3, pp. 461-470, 2004.
- [18] N. Shimizu, N. Watanabe, T. Furuta, and T. Ishibashi, "InP-InGaAs uni-traveling-carrier photodiode with improved 3-dB bandwidth of over 150 GHz," *Photonics Technology Letters, IEEE*, vol. 10, no. 3, pp. 412-414, 1998.
- [19] C. H. Cox, III, E. I. Ackerman, G. E. Betts, and J. L. Prince, "Limits on the performance of RF-over-fiber links and their impact on device design," *Micro-wave Theory and Techniques, IEEE Transactions on*, vol. 54, no. 2, pp. 906-920, 2006.
- [20] A. R. Williams, A. L. Kellner, and P. K. L. Yu, "Dynamic range performance of a high speed, high saturation InGaAs/InP pin waveguide photodetector," *Electronics Letters*, vol. 31, no. 7, pp. 548-549, 1995.

- [21] A. Ramaswamy, N. Nunoya, K. J. Williams, J. Klamkin, M. Piels, L. A. Johansson, A. Hastings, L. A. Coldren, and J. E. Bowers, "Measurement of intermodulation distortion in high-linearity photodiodes," *Opt. Express*, vol. 18, no. 3, pp. 2317-2324.
- [22] T. Ohno, H. Fukano, and Y. Muramoto, "Measurement of intermodulation distortion in high-output-power uni-travelling-carrier refracting-facet photodiode at 40 GHz," *Electronics Letters*, vol. 36, no. 23, pp. 1954-1955, 2000.
- [23] D. Ning, L. Ning, S. Demiguel, and J. C. Campbell, "High-speed high-current InGaAs/InP photodiode with thick depletion region," *Lasers and Electro-Optics Society, 2005. LEOS 2005. The 18th Annual Meeting of the IEEE*, pp. 458-459, 2005.
- [24] H. Jiang, D. S. Shin, G. L. Li, T. A. Vang, D. C. Scott, and P. K. L. Yu, "The frequency behavior of the third-order intercept point in a waveguide photodiode," *Photonics Technology Letters, IEEE*, vol. 12, no. 5, pp. 540-542, 2000.
- [25] K. J. Williams and R. D. Esman, "Photodiode DC and microwave nonlinearity at high currents due to carrier recombination nonlinearities," *Photonics Technology Letters, IEEE*, vol. 10, no. 7, pp. 1015-1017, 1998.
- [26] T. H. Stievater and K. J. Williams, "Thermally induced nonlinearities in high-speed p-i-n photodetectors," *Photonics Technology Letters, IEEE*, vol. 16, no. 1, pp. 239-241, 2004.
- [27] K. Satzke, G. Weiser, R. Höger, and W. Thulke, "Absorption and electroabsorption spectra of an $\text{In}_{1-x}\text{Ga}_x\text{P}_{1-y}\text{As}_y/\text{InP}$ double heterostructure," *J. Appl. Phys.*, vol. 63, pp. 5485 - 5491, 1988.

- [28] J. S. Ng, C. H. Tan, J. P. R. David, G. Hill, and G. J. Rees, "Field dependence of impact ionization coefficients in In_{0.53}Ga_{0.47}As," *Electron Devices, IEEE Transactions on*, vol. 50, no. 4, pp. 901-905, 2003.
- [29] M. S. Leeson and F. P. Payne, "Predicted performance of Franz-Keldysh effect optical reflection modulators and comparisons with similar multiple quantum well-based devices," *Optoelectronics, IEE Proceedings -*, vol. 141, no. 4, pp. 257-264, 1994.
- [30] R. J. McIntyre, "Multiplication noise in uniform avalanche diodes," *IEEE Transactions on Electron Devices*, vol. ED-13, no. 1, pp. 164-168, 1966.
- [31] A. Joshi, S. Datta, and D. Becker, "GRIN Lens Coupled Top-Illuminated Highly Linear InGaAs Photodiodes," *Photonics Technology Letters, IEEE*, vol. 20, no. 17, pp. 1500-1502, 2008.
- [32] K. J. Williams, D. A. Tulchinsky, and A. Hastings, "High-power and high-linearity photodiodes," *IEEE Lasers and Electro-Optics Society, 2008. LEOS 2008. 21st Annual Meeting of the*, pp. 290-291, 2008.
- [33] M. Chtioui, A. Enard, D. Carpentier, S. Bernard, B. Rousseau, F. Lelarge, F. Pommereau, and M. Achouche, "High-Power High-Linearity Uni-Traveling-Carrier Photodiodes for Analog Photonic Links," *Photonics Technology Letters, IEEE*, vol. 20, no. 3, pp. 202-204, 2008.
- [34] Z. Griffith, K. YoungMin, M. Dahlstrom, A. C. Gossard, and M. J. W. Rodwell, "InGaAs-InP metamorphic DHBTs grown on GaAs with lattice-matched device performance and $f_T, f_{max} \gg 268$ GHz," *Electron Device Letters, IEEE*, vol. 25, no. 10, pp. 675-677, 2004.

- [35] C. H. Tan, G. J. Rees, P. A. Houston, J. S. Ng, W. K. Ng, and J. P. R. David, "Temperature dependence of electron impact ionization in $\text{In}_{0.53}\text{Ga}_{0.47}\text{As}$," *Applied Physics Letters*, vol. 84, no. 13, pp. 2322-2324, 2004.
- [36] K. L. Chen, H. H. Lin, G. J. Jan, Y. H. Chen, and P. K. Tseng, "Photoreflectance temperature dependence of graded InAlAs/InGaAs heterojunction bipolar transistor layers," *Journal of Applied Physics*, vol. 78, no. 6, pp. 4035-4038, 1995.
- [37] H. Fushimi, T. Furuta, T. Ishibashi, and H. Ito, "Photoresponse Nonlinearity of a Uni-Traveling-Carrier Photodiode and Its Application to Optoelectronic Millimeter-Wave Mixing in 60 GHz Band," *Jpn. J. Appl. Phys.*, vol. 43, pp. L966-L968, 2004.
- [38] F. M. Kuo, Y. S. Wu, and J. W. Shi, "Near-Ballistic Unitraveling-Carrier Photodiode-Based V-band Optoelectronic Mixers With Low Upconversion Loss and High Operation Current Performance Under Optical IF Signal Injection," *Electron Device Letters, IEEE*, vol. 30, no. 1, pp. 21-23, 2009.
- [39] I. Hiroshi and et al., "Continuous THz-wave generation using antenna-integrated uni-travelling-carrier photodiodes," *Semiconductor Science and Technology*, vol. 20, no. 7, p. S191, 2005.
- [40] M. Dentan and B. de Cremoux, "Numerical simulation of the nonlinear response of a p-i-n photodiode under high illumination," *Lightwave Technology, Journal of*, vol. 8, no. 8, pp. 1137-1144, 1990.
- [41] J. L. Beutler, C. S. Clauss, M. S. Johnson, A. R. Hawkins, M. D. Jack, G. R. Chapman, and K. Kosai, "Frequency response of solid-state impact ionization multipliers," *Journal of Applied Physics*, vol. 101, no. 2, pp. 023117-9, 2007.

- [42] A. Hirata, T. Furuta, H. Ito, and T. Nagatsuma, "10-Gb/s millimeter-wave signal generation using photodiode bias modulation," *Lightwave Technology, Journal of*, vol. 24, no. 4, pp. 1725-1731, 2006.
- [43] S. A. Malyshev and A. L. Chizh, "p-i-n Photodiodes for Frequency Mixing in Radio-Over-Fiber Systems," *Lightwave Technology, Journal of*, vol. 25, no. 11, pp. 3236-3243, 2007.
- [44] D. M. Pozar, "Microwave Engineering," *third edition, John Wiley & Sons, Inc.*, p. 321, 2005

Vita

Huapu Pan (潘华璞) was born in Zigong, Sichuan, China on April 22, 1984, the son of Shiyong Pan (潘世永) and Ping Zheng (郑萍). He graduated from Chengdu No. 7 High School in 2002. He then began his undergraduate study in Peking University, Beijing, China, where he received his Bachelor of Physics in 2006. He joined the graduate program in Electrical Engineering at the University of Virginia in the spring of 2007 and started research on photodetectors under Dr. Campbell's supervision.

Permanent address: No. 8, Unit 2, Building 22,
Xihua University
Chengdu, China 610039

This dissertation was typed by the author.